PASJ: Publ. Astron. Soc. Japan **64**, 70, 2012 August 25

Star Formation and AGN Activity in Galaxies Classified Using the 1.6 μm Bump and PAH Features at $z = 0.4$–2

Hitoshi HANAMI,[1] Tsuyoshi ISHIGAKI,[1,2] Naofumi FUJISHIRO,[3] Kouichiro NAKANISHI,[4] Takamitsu MIYAJI,[5,6] Mirko KRUMPE,[6,7] Keiichi UMETSU,[8] Youichi OHYAMA,[8] Hyunjin SHIM,[9] Myungshin IM,[10] Hyoung Mok LEE,[10] Myung Gyoon LEE,[10] Stephen SERJEANT,[11] Glenn J. WHITE,[11,12] Christopher N. WILLMER,[13] Tomotsugu GOTO,[14] Shinki OYABU,[15] Toshinobu TAKAGI,[16] Takehiko WADA,[16] and Hideo MATSUHARA[16]

[1]*Physics Section, Iwate University, 3-18-34 Ueda, Morioka, Iwate 020-8550*
hanami@iwate-u.ac.jp
[2]*Asahikawa National College of Technology, 2-2 Syunkodai, Asahikawa, Hokkaido 071-8142*
[3]*Kyoto Sangyo University, Motoyama, Kamigamo, Kita-ku, Kyoto 603-8555*
[4]*ALMA/NAOJ Office, Calle Joaquin Montelro 3000, Oficina 702, Vitacura, Santiago, Chili*
[5]*Instituto de Astronomía, Universidad Nacional Autónoma de México, Ensenada, Baja Californioa, México*
(mailing address: P.O. Box 439027, San Ysidro, CA 92143-9027, USA)
[6]*University of California, San Diego, Center for Astrophysics and Space Sciences,*
9500 Gilman Drive, La Jolla, CA 92093-0424, USA
[7]*ESO Headquarters, Karl-Schwarzschild-Straße 2, 85748, Garching, Germany*
[8] *Institute of Astronomy and Astrophysics, Academia Sinica, P.O. Box 23-141, Taipei 10617, Taiwan, R.O.C.*
[9]*School of Science Education, Kyungpook National University, Daegu 702-701, Korea*
[10]*Astronomy Program, Department of Physics and Astronomy, Seoul National University, Seoul 151-747, Korea*
[11]*Department of Physics and Astronomy, The Open University, Walton Hall, Milton Keynes, MK7 6AA, UK*
[12]*Space Science and Technology Division, STFC Rutherford Appleton Laboratory, Chilton, Didcot, UK*
[13]*Steward Observatory, University of Arizona, 933 North Cherry Avenue, Tucson, AZ 85721, USA*
[14] *Institute for Astronomy, University of Hawaii, 2680 Woodlawn Drive, Honolulu, HI 96822, USA*
[15]*Graduate School of Science, Nagoya University, Furo-cho, Chikusa-ku, Nagoya 464-8602*
[16]*Institute of Space and Astronautical Science, Japan Aerospace Exploration Agency,*
3-1-1 Yoshinodai, Chuo-ku, Sagamihara 252-5210

(Received 2010 August 31; accepted 2011 December 28)

Abstract

We studied the star-formation and AGN activity of massive galaxies in the redshift range $z = 0.4$–2, which were detected in a deep survey field using the AKARI InfraRed (IR) astronomical satellite and Subaru telescope toward the North Ecliptic Pole (NEP). The AKARI/IRC Mid-InfraRed (MIR) multiband photometry was used to trace the star-forming activities with Polycyclic Aromatic Hydrocarbon (PAH) emission, which is effective not only to distinguish between star-forming and AGN galaxies, but also to estimate the Star Formation Rate (*SFR*) with converting its flux to the total emitting IR (TIR) luminosity. In combination with the analyses of the stellar components, we studied the MIR SED features of star-forming and AGN-harboring galaxies, which we summarize below: (1) The rest-frame 7.7-μm and 5-μm luminosities are good tracers of star-forming and AGN activities from their PAH and dusty tori emissions, respectively. (2) For dusty star-forming galaxies without AGN, their *SFR* shows a correlation that is nearly proportional to their stellar mass, and their specific *SFR* (*sSFR*) per unit stellar mass increases with redshift. Extinctions estimated from their TIR luminosities are larger than those from their optical SED fittings, which may be caused by geometric variations of dust in them. (3) Even for dusty star-forming galaxies with AGN, *SFR*s can be derived from their TIR luminosities with subtraction of the obscured AGN contribution, which indicates that their *SFR*s were possibly quenched around $z \simeq 0.8$ compared with those without AGN. (4) The AGN activity from their rest-frame 5-μm luminosity suggests that their Super Massive Black Holes (SMBHs) could already have grown to $\simeq 3 \times 10^8\ M_\odot$ in most massive galaxies with $10^{11}\ M_\odot$ at $z > 1.2$, and the mass relation between SMBHs and their host galaxies has already become established by $z \simeq 1$–2.

Key words: galaxies: evolution — galaxies: high-redshift — infrared: galaxies

1. Introduction

A major issue in observational cosmology is to reconstruct the cosmic evolution of star formation and the detailed growth history of present-day galaxies. Even though it is not easy to reconstruct the whole path of the stellar mass for galaxies as a function of the present-day galaxy stellar mass, $M_{*;0}$, and the cosmic time, t, as $M_*(M_{*;0}, t)$, it is essential to obtain knowledge of their Star Formation Rate (*SFR*) as a function $SFR(M_*, t)$.

Recent Near-InfraRed (NIR) observations suggest that most of the stellar mass is contained in massive galaxies, and

that this situation had already become established at $z \simeq 1$. This appears to have been followed by a rapid evolution of the stellar mass density between $z = 1$–3 (Papovich et al. 2001; Dickinson et al. 2003; Fontana et al. 2003; Franx et al. 2003; Drory et al. 2004; Fontana et al. 2004; Glazebrook et al. 2004; van Dokkum et al. 2004; Labbé et al. 2005; Fontana et al. 2006; Papovich 2006; Yan et al. 2006; Webb et al. 2006; Kriek et al. 2006; Pozzetti et al. 2007; Arnouts et al. 2007; Vergani et al. 2008). These recent studies imply that most of the massive galaxies must have already formed at $z \simeq 1$, supporting the so-called *downsizing* scenario (Cowie et al. 1997). In this scenario, star formation shifts from higher to lower mass galaxies as a function of the cosmic time, t, although the stellar mass in massive galaxies may not directly follow the growth history of their Dark Matter Halos (DMHs), which build up hierarchically from less-massive systems to more-massive ones at a later time. However, several studies of massive galaxies at $z < 1$ (Brown et al. 2007; Faber et al. 2007; Brown et al. 2008) report the evolution from predominantly blue to red galaxies, suggesting that the number and stellar mass of galaxies in the red-sequence may continue to grow, even after $z = 1$ (Bell et al. 2004; Zucca et al. 2006), in agreement with the hierarchical merging scenario. Recently, a mass-dependent quenching of star formation has been proposed to explain these rapid increases of the number density of the massive galaxies relative to lower-mass galaxies at $z = 1$–2 (Peng et al. 2010; Kajisawa et al. 2011; Brammer et al. 2011).

The evolutionary path of $M_*(M_{*;0}, t)$ up to the present mass, $M_{*;0}$, can also be reconstructed from knowledge of the $SFR(M_*, t)$. Recent studies have confirmed the features for rapid *SFR* evolution up to $z \simeq 2$ (Brinchmann & Ellis 2000; Fontana et al. 2003; Pérez-González et al. 2005; Feulner et al. 2005a, 2005b; Papovich 2006; Iglesias-Pramo et al. 2007; Zheng et al. 2007; Cowie & Barger 2008; Damen et al. 2009; Dunne et al. 2009; Santini et al. 2009; Pannella et al. 2009). However, we have not found a general consensus concerning the stellar mass dependence for specific *SFR*: $sSFR = SFR/M_*$ (the *SFR* per unit stellar mass). Most studies based on UV-derived *SFR*'s have found evidence to support an anti-correlation with stellar mass, not only local galaxies, but also the distant universe, supporting the downsizing scenario. It is not easy, however, to accept that UV estimates are the only way to estimate the *SFR* that will capture all of the emission originally from newly born stars in a galaxy, which can be independently estimated from rest-frame luminosities in the UV, IR, Submillimeter (Submm), and radio-wavelength regions by introducing appropriate calibration factors. Although the UV luminosity is used as a proxy of the *SFR*, its reliability often depends on the use of large, and rather uncertain corrections for dust extinction. Most of the short-wavelength photons from star-forming galaxies are reprocessed through absorption and scattering with dust in their star-forming regions, and then re-emitted in the IR–Submm wavelength regions. Thus, the mid/far-IR and their Submm emissions become an important tracer of the total star-forming activity in high-z galaxies.

The total IR (TIR) luminosity, $L_{\rm IR}$, integrated across the long wavelength spectral region is a good proxy for the *SFR*, which is relatively independent of the dust obscuration (Kennicutt 1998). Luminous InfraRed Galaxies (LIRGs) and Ultra Luminous InfraRed Galaxies (ULIRGs) up to $z = 1$–2, detected at the Mid-InfraRed (MIR) wavelength with the IR observing satellites as ISO (Mann et al. 2002; Elbaz et al. 2002; Pozzi et al. 2004; Dennefeld et al. 2005; Taylor et al. 2005; Marcillac et al. 2006a, 2006b), AKARI (Takagi et al. 2007, 2010, 2012), and Spitzer (Egami et al. 2004; Shapley et al. 2005; Caputi et al. 2006; Choi et al. 2006; Marcillac et al. 2006a, 2006b, Papovich 2006; Papovich et al. 2006; Reddy et al. 2006; Elbaz et al. 2007; Papovich et al. 2007; Rocca-Volmerange et al. 2007; Shim et al. 2007; Teplitz et al. 2007; Brand et al. 2008; Magnelli et al. 2008; Dasyra et al. 2009; Hernán-Caballero et al. 2009; Murphy et al. 2009; Santini et al. 2009; Strazzullo et al. 2010), have shown that the *SFR* rapidly increases with the redshift, as they contribute $\simeq$70% of the cosmic IR luminosity density (Floc'h et al. 2005). The MIR emission from LIRGs/ULIRGs is evidence of dusty starburst or AGN surrounded by a dusty torus. Recently, the LIRGs/ULIRGs are expected to suppress star formation at $z = 1$–2 with feedback activity from starbursts or AGNs. Understanding the LIRGs/ULIRGs at $z = 1$–2 can be the key to solve the cosmic history of star formation and AGN activities. The *SFR* for galaxies detected with Spitzer is frequently estimated with the TIR luminosity estimated from the 24 μm flux (Daddi et al. 2004; Santini et al. 2009; Pannella et al. 2009), which is nearly proportional to their stellar mass up to $z \simeq 2$. These recent results with Spitzer are also basically consistent with recent results from a stacking analysis for their radio emissions (Dunne et al. 2009; Pannella et al. 2009) as another *SFR* estimation immune to dust extinctions. These two radio stacking analyses, however, show a discrepancy in their details, as Dunne et al. (2009) reported *sSFR* with a negative correlation to stellar mass, while Pannella et al. (2009) reported *sSFR* with stellar mass independence. Thus, there may be various unknown factors in the *SFR* estimations. The TIR luminosity $L_{\rm IR}$ of LIRGs/ULIRGs is generally derived from fittings of the observed Spectral Energy Distribution (SED) with synthetic templates. In the SED fitting, we could sometimes use only a few bands in the IR wavelength without longer 100–1000 μm wavelengths, which may cause large uncertainties in the $L_{\rm IR}$ estimation. Obscured AGNs are another notable problem in the $L_{\rm IR}$ estimation. This means that a sample selection without significant AGN contamination is also important to obtain an accurate $SFR_{\rm IR}$. Thus, systematically designed surveys are required to construct samples for distant star-forming galaxies.

Optical surveys have been successful in selecting numerous Lyman Break Galaxies (LBGs) as star-forming galaxies beyond $z \sim 2$ (Steidel et al. 1996a, 1996b, 1999; Lehnert & Bremer 2003; Iwata et al. 2003; Ouchi et al. 2003, 2004; Dickinson et al. 2004; Sawicki & Thompson 2006a, 2006b) and even up to $z \simeq 6$ (Yan et al. 2004; Stanway et al. 2003; Bunker et al. 2004; Bouwens et al. 2004; Shimasaku et al. 2005). They may, however, fail to detect substantial numbers of massive galaxies at $z < 3$, in which the Lyman break photometric technique does not work well with ground-based telescopes because of telluric absorption. Furthermore, even if galaxies are undergoing intensive star formation, the internal dust extinction of their UV radiation may reduce

the prominence of their Lyman break features, to appear as LIRGs/ULIRGs in the local universe. However, alternative photometric techniques can be used to select massive high-z galaxies through their Balmer/4000 Å break or the 1.6 μm bump features in their SEDs, as evidence of the presence of an evolved stellar population. We will designate the former and the latter as "Balmer" Break Galaxies (BBGs) and as IR "Bump" Galaxies (IRBGs), respectively. It is known that both star-forming and passive BBGs in the redshift desert around $z = 2$ can be selected with a simple and sophisticated two-color selection based on B, z, and K band photometry (Daddi et al. 2004). This three-filter optical–NIR technique was designed to detect the Balmer/4000 Å break, nearly free from the dust extinction which caused some difficulties for previous "red color" techniques relying on a color diagnostic of $(R - K)_{\rm Vega} > 5$–6, corresponding to $(R - K)_{AB} > 3.35$–4.35 (Elston et al. 1988; Thompson et al. 1999; Daddi et al. 2000; Firth et al. 2002; Roche et al. 2002, 2003) or for $(J - K)_{\rm Vega} > 2.3$ corresponding to $(J - K)_{AB} > 1.3$[1] (Pozzetti et al. 2003; Franx et al. 2003). With the NIR observations from Spitzer and from AKARI, it has become possible to select IRBGs at $z > 1$ with NIR colors at $> 3\,\mu$m of the 1.6 μm bump (Simpson & Eisenhardt 1999; Sawicki 2002; Berta et al. 2007). These optical–NIR observations, detecting the Balmer/4000 Å break and the 1.6 μm bump, have been also useful to trace how stellar mass is correlated with the absolute NIR luminosity.

Although optical–NIR multi-band photometry has a potential to select a sample for star-forming massive galaxies, it may not be completely free from the AGN contamination. MIR multi-band photometry tracing Polycyclic Aromatic Hydrocarbon (PAH) emissions at 6.2, 7.7, and 11.3 μm and Silicate (Si) absorption at 10 μm (rest-frame) from dusty star-forming regions, can be used to discriminate between the star-forming activity in LIRGs/ULIRGs and that of AGN dominated galaxies. Thus, systematic multi-wavelength observations that include observations at $> 2\,\mu$m are important for studying the star-forming activity of massive high-z galaxies, and in looking back at the evolution of their *SFR*s. In order to connect the history of stellar mass growth in massive galaxies traced in optical–NIR wavelength with ground-based telescopes and that of star formation traced in MIR wavelength observed outside of the atmosphere, we undertook multi-wavelength surveys of deep and wide areas with $\simeq 0.38$ and $\simeq 5.8\,{\rm deg}^2$, respectively, in a field close to the North Ecliptic Pole (NEP), which were extensively observed at the IR wavelength with the first Japanese IR astronomical satellite, AKARI.

In this paper, we attempt to reconstruct the cosmic history of dusty massive galaxies up to $z \simeq 2$, selected from optical–IR images in the NEP survey field. We report on: (1) photometric redshift $z_{\rm phot}$, stellar mass M_*, and $SFR_{\rm UV;cor}$ (see subsection 7.1), which were estimated with their optical–NIR SED fittings, (2) the distinction between dusty starburst and AGN dominated galaxies using the MIR SED features, (3) TIR luminosities of starburst dominated galaxies with subtraction of the obscured AGN contribution, from which we could derive $SFR_{\rm IR+UV}$ (subsection 7.1) complementary to $SFR_{\rm UV:cor}$, and (4) IR luminosities of the dusty tori of AGN dominated galaxies, which show evolutionary trends in the connection between AGN and star-forming activities.

In section 2, we summarize the data we used; in section 3, we present the photometry for z'-band detected galaxies in our multi-wavelength dataset; in section 4, we summarize the photometric redshift results for the z'-detected galaxies; in section 5, we also report AKARI/IRC detected IRBGs classified using the redshifted 1.6-μm IR bump in the NIR bands, which are divided into three redshifted subgroups; in section 6, we present AKARI/IRC MIR detected galaxies that correspond to LIRGs/ULIRGs, and classify them into dusty starbursts and AGNs from their MIR SEDs with/without PAH features in the MIR bands; in section 7, we derive the TIR luminosities for the MIR detected galaxies; in section 8, we estimate their star-formation rates and extinctions; in section 9, we reconstruct their intrinsic stellar populations with extinction correction; in section 10 we also consider the AGN activities in the MIR detected galaxies; in section 11, we discuss some expectations for on-going and future observations; finally in section 12, we summarize the conclusions of our study.

In this paper we adopt $H_0 = 70\,{\rm km\,s^{-1}\,Mpc^{-1}}$, $\Omega_{\rm m} = 0.3$, $\Omega_\Lambda = 0.7$ throughout. All magnitudes are represented in the *AB* system (e.g., Oke 1974).

2. The Data Set

We used mainly data sets obtained in the AKARI Deep imaging survey with all of the available bands of the InfraRed Camera (IRC) on AKARI (Onaka et al. 2007) near the NEP. We define the *N2*, *N3*, *N4*, *S7*, *S9W*, *S11*, *L15*, *L18W*, and *L24* bands as having central wavelengths at 2, 3, 4, 7, 9, 11, 15, 18, and 24 μm, respectively. These are reported in this paper as the IR photometric *AB* magnitude of an object observed in the various IRC bands. Details of the data reduction of the NEP Deep and Wide surveys have been presented by Wada et al. (2008) and Lee et al. (2007) (see also Hwang et al. 2007; Ko et al. 2012), respectively. We used the same IRC scientific data for the AKARI NEP Deep field as described in detail by Wada et al. (2008), which include mosaicing them together and making pointing and distortion corrections, as well as corrections to mitigate any detector artifacts.

The AKARI NEP Deep survey area has been covered by observations in the near-UV u^* band with the CFHT/MegaCam(M-Cam) (Boulade et al. 2003); the optical B, V, R, i', and z' bands with the Subaru/Suprime-Cam(S-Cam) (Miyazaki et al. 2002); and in the NIR J and $K_{\rm s}$ bands with the KPNO(2.1 m)/Flamingos(FLMG) (Elston et al. 2006). Details of the Subaru/S-Cam, CFHT/M-Cam, and KPNO/FLMG data reduction can be found in Imai et al. (2007), Takagi et al. (2012), and T. Ishigaki et al. (in preparation). In this study, we selected $\simeq 56000$ galaxies with $z' < 26.4$ and $S/N > 3$. For these sources, we estimated their multi-wavelength photometric characteristics, while adding ground-based near-UV, optical, and NIR imaging data, to the AKARI/IRC data, as described in the following section. For simplification, we used u, i, z, and K as u^*, i', z', and $K_{\rm s}$, respectively, for representing colors derived from the respective filters.

[1] $J_{AB} = J_{\rm Vega} + 0.89$, $K_{{\rm s}_{AB}} = K_{{\rm s}_{\rm Vega}} + 1.84$.

3. Photometry

3.1. Optical and NIR Photometry for Ground-Based Data

Object detection and photometry were made using SExtractor 2.3.2 (Bertin & Arnouts 1996). The z' S-Cam image was used to detect optical objects, defined as a source with a 5 pixel connection above the $2\,\sigma$ noise level. We derived the Full Width Half Maximum (FWHM) of the Point Spread Function (PSF) from photometric images of stellar objects as point sources (see their selection scheme in subsection 3.4), which are summarized in table 1. In the process to make a catalogue, the reason why the z'-band was chosen as the detection band is the following: (1) the FWHM of the PSF $1''$ in the z' image with the S-Cam is good enough to prevent confusion, (2) z' photometry is one of the essential bands in star–galaxy selection with the *BzK* color, as shown in subsection 3.4, (3) most of the galaxies of interest as detected by AKARI; *N3* Red galaxies (*N3*Rs) and MIR bright *N3*Rs (Mb*N3*Rs), and optical–NIR selected galaxies as BBGs, are clearly identified in the z' image. See details about the *N3*Rs, Mb*N3*Rs, and BBGs in subsections 5.1 and 6.1, and in appendix 1, respectively. The catalogue of detected objects to $z' < 26.4$ with a $2''$ diameter aperture was generated over the whole $23' \times 32'$ area of the S-Cam z' image.

After selecting $\sim$56000 z' sources in the area observed with the FLMG, from the $\sim$66000 sources detected in the S-Cam z' images, we performed aperture photometry in the near-UV u^*, optical B, V, R, i', z', and NIR J, K_s images, fixed at the positions of the z'-detected sources. Photometry on the B, V, R, i', and z' images was performed with a small $2''$ diameter aperture with the SExtractor. The photometry on the u^* and the J and K_s images was performed with larger $3''$ and $4''$ diameter apertures with the photo of the IRAF task, since these image qualities in off-center regions are not good, due to the aberrations compared with those of the S-Cam. The larger aperture photometry reduces the uncertainties in the photometry and the alignment errors in the World Coordinate System (WCS) from these aberrations. The errors of the ground-based optical and NIR photometry come mainly from the sky background and its fluctuation. We estimated them from a Monte-Carlo simulation with the same method as that of T. Ishigaki et al. (in preparation), in which we measured the counts in randomly distributed apertures and fit the negative part of the count histogram with a Gaussian profile. Thus, the $3\,\sigma$ limiting magnitudes, $m_{\rm lim.}$, were derived from the background estimation, as summarized in table 2.

The final integrated magnitudes for all filters were obtained after applying an aperture correction, $\Delta m_{\rm a.c.}$, based on empirical PSFs, which were constructed from the photometry for stars in each image band. All of the optical and NIR magnitudes were further corrected for a Galactic extinction of $E(B-V) = 0.041$, based on observations of the survey area taken from Schlegel, Finkbeiner, and Davis (1998) and using the empirical selective extinction function of Cardelli, Clayton, and Mathis (1989).

3.2. Infrared Photometry for AKARI/IRC Images

As shown above, we produced a multiband merged catalogue from the ground-based telescope images for the z'-detected objects in the field. As shown in table 2, the depth of *N2* images obtained with the AKARI/IRC is comparable to that of K_s images with the KPNO/FLMG, although the images

Table 1. Summary of photometric parameters.

Band	FWHM (pixel)	FWHM ($''$)	Ap.D.[†] ($''$)
u^*	4.9	0.90	3.0
B, V, R, i', z'	5.2	1.00	2.0
J (SE)	2.7[‡]	1.60	3.0
J (NE)	3.1[‡]	1.90	3.0
J (SW)	3.0[‡]	1.80	3.0
J (NW)	3.5[‡]	2.10	4.0
K_s (SE)	2.7[‡]	1.60	3.0
K_s (NE)	3.0[‡]	1.80	3.0
K_s (SW)	3.7[‡]	2.20	4.0
K_s (NW)	3.2[‡]	1.90	4.0
N2, *N3*, *N4*	3.1	4.50	8.0
S7, *S9W*, *S11*	2.4	5.60	10.0
L15, *L18W*, *L24*	2.8	6.70	10.0

[†] Aperture diameter.
[‡] The S-Cam FoV of $34' \times 27'$ is covered with 4 FLMG FoV, in which each covers the $25' \times 30'$ area.

Table 2. Summary of limiting magnitudes and photometric corrections.

Band	$m_{\rm lim.}$[†] (*AB*)	$\Delta m_{\rm a.c.}$[‡] (*AB*)	$\Delta m_{\rm g.e.}$[§] (*AB*)	$\Delta m_{\rm s.o.}$[‖] (*AB*)
u^*	26.31	−0.06	−0.20	+0.20
B	28.25	−0.24	−0.18	+0.00
V	27.57	−0.24	−0.13	−0.02
R	27.41	−0.24	−0.11	−0.11
i'	27.14	−0.24	−0.09	−0.07
z'	26.40	−0.24	−0,06	−0.13
J (SE)	22.28	−0.22	−0.04	+0.02
J (NE)	22.22	−0.27	−0.04	+0.02
J (SW)	22.23	−0.28	−0.04	+0.02
J (NW)	21.83	−0.20	−0.04	+0.02
K_s (SE)	21.66	−0.22	−0.02	−0.09
K_s (NE)	21.58	−0.22	−0.02	−0.09
K_s (SW)	21.34	−0.22	−0.02	−0.09
K_s (NW)	21.20	−0.19	−0.02	−0.09
N2	21.89	−0.24	−0.01	−0.08
N3	22.24	−0.24	−0.01	+0.12
N4	22.49	−0.24	−0.01	+0.13
S7	20.29	−0.20		
S9W	20.00	−0.22		
S11	19.82	−0.24		
L15	19.60	−0.27		
L18W	19.60	−0.26		
L24	18.60	−0.27		

[†] $m_{\rm lim.}$ is the $3\,\sigma$ limiting magnitude.
[‡] $\Delta m_{\rm a.c.}$ is the aperture correction in magnitude.
[§] $\Delta m_{\rm g.e.}$ is the magnitude correction for Galactic extinction in the field.
[‖] $\Delta m_{\rm s.o.}$ is the magnitude correction for systematic offset with the SED calibration for the stellar objects.

of all other bands at longer wavelengths are shallower than those of z'. In fact, from 5819 sources extracted with the SExtractor in the *N3* band with a 5-pixel connection above the $2\,\sigma$ noise level, 92% of them can be identified as 5332 counterparts of z'-detected sources without confusion. Thus, we performed photometry for all of the AKARI/IRC bands on the z'-detected sources.

The IRC photometry on the z'-detected sources was performed with $8''$ and $10''$ diameter apertures for the NIR (*N2*, *N3*, and *N4*) and MIR (*S7*, *S9W*, *S11*, *L15*, *L18W*, and *L24*) bands, respectively, with the IRAF task photo.

The final integrated magnitudes in the IRC photometry were obtained after applying an aperture correction based on growth curves with empirical PSFs, constructed from photometry of stars in each band image, which is basically similar to the scheme descirbed in Takagi et al. (2012). The aperture corrections for the IRC are summarized in table 2, along with those of the ground-based near-UV, optical, and NIR magnitudes.

In order to reduce the source confusion due to the fact that the IRC PSFs are notably worse than those in the ground-based observed images, we performed IRC photometry with several different apertures in each IRC band, and compared these magnitudes, excluding objects with a large magnitude difference from the IRC counterparts in the z'-detected catalogue. In the photometry for the *N2*, *N3*, and *N4* bands, we optimized the constraint for the IRC/NIR counterparts as $N3(6'') - N3(8'') < 0.51$ between $6''$ and $8''$ diameter photometry in the *N3* band, while adding another constraint of $K_{\rm s} - N2 < 1.0$ at $2\,\mu$m.

For MIR sources detected with $S/N > 3$ at least in one MIR band, there were many more sources with confusion compared with the NIR sources. We could select $\sim$800 MIR bright *N3* Red galaxies (Mb*N3*Rs) and $\sim$900 MIR marginally-detected *N3* Red galaxies (Mm*N3*Rs), as shown in section 6. However, we took confirmed samples of $\sim$600 Mb*N3*Rs and $\sim$600 Mm*N3*Rs after excluding NIR counterparts of the MIR sources having pairs within $6''$, in order to correctly select the candidates of LIRGs at $z > 0.4$, as discussed in section 6. Roughly two thirds of these Mb*N3*Rs and Mm*N3*Rs were also identified as sources listed in another MIR source catalogue, reported by Takagi et al. (2012), which were almost the same after taking the difference in their detection limits into consideration, since the former was selected with $S/N > 3$ at least in one MIR band, while the latter was with $S/N > 5$. Concerning these NIR and MIR detected galaxies, we could confirm with our eyes that it could work to mostly exclude confusion from neighborhood sources within a circular region corresponding to the IRC PSF radius around each z' source.

3.3. Photometric Check and Systematic Offsets

In order to further check the photometric zero points, we performed SED fittings with $u^*BVRi'z'JK_{\rm s}$ and AKARI *N2*, *N3*, and *N4* photometric data for the stellar objects. It is well known that galactic stars can be clearly selected using a two-color criterion (Daddi et al. 2004; Kong et al. 2006; Lane et al. 2007; Quadri et al. 2007; Blanc et al. 2008):

$$BzK_* \equiv (z - K)_{AB} - 0.3(B - z)_{AB} < -0.3\,, \qquad (1)$$

where we have taken -0.3 as a parameter on the right side, which defines a line separating stars and galaxies that is slightly larger than Daddi's original value of -0.5, to reduce the contamination of stars in our galaxy sample. We used the *BzK* color criterion to select the photometric calibrators as stellar objects with additional criteria for the magnitudes $z' > 19$ and stellarity parameter CLASS_STAR > 0.95 in SExtractor (see also subsection 3.4). We also excluded IRC/NIR confused image sources by visual examination.

We adopted SED templates from the stellar library of Bruzual–Persson–Gunn–Stryker (BPGS) atlas,[2] based on Gunn and Stryker (1983), which is similar to the stellar spectra of Pickles (1998),[3] and Lejeune, Cuisinier, and Buser (1997). In order to include the *N4* magnitudes in our fitting of SEDs to the stellar objects with the BPGS atlas, we extended the library SEDs beyond wavelengths of $\lambda > 2.5\,\mu$m with a Rayleigh–Jeans law. The best fit was sought by means of χ^2 minimization, among all templates in the stellar library after varying their normalization. We estimated the offsets in each of the bands, which are seen as systematic discrepancies between the original observed magnitudes and the best-fitted library magnitudes. These systematic offsets are also summarized in table 2. Since the derived offsets are less than 0.2, basically we can confirm the accuracy of the photometric zero points in all bands. In a comparison between the spectroscopic and photometric redshifts, the result for the systematic offset is slightly better than that without this. Thus, we use the offset.

3.4. Star–Galaxy Separation

As discussed in subsection 3.3, the colors estimated with the BPGS star atlas overlap with the observed stellar sequence appearing in the *BzK* color region (see figure 44 in appendix 1). Thus, we can also use the *BzK* criterion of equation (1) as a robust method for star–galaxy separation. For sources detected with $S/N > 3$, up to $K_{\rm s} = 20$, we excluded objects satisfying the following conditions: (1) equation (1) and (2) stellarity parameter CLASS_STAR > 0.95 in SExtractor. In order to separate stars and galaxies for all of the z'-detected objects up to an optical limiting magnitude $z' = 26$ that are fainter than the above $K_{\rm s}$ detected sources, we performed SED fittings for them with not only the BC03 model (Bruzual & Charlot 2003) for galaxies, but also the BPGS star atlas for stellar objects, including those corrected with Allen's Milky Way extinction curves. We extracted objects as stellar objects, which were fitted better by the latter than the former, from a catalogue of z'-detected galaxies (see also subsection 4.1). These stellar objects appear in the sequences of the BPGS star atlas in BBG color–color diagrams (see not only figure 44, but also figures 45 and 46 in appendix 1).

4. Photometric Redshifts

4.1. Photometric and Spectroscopic Redshifts

For all of the z'-detected galaxies remaining after the star–galaxy separation procedure, as described in subsection 3.4, we simultaneously obtained the photometric redshift, $z_{\rm phot}$, and the absolute magnitude, $M_{H;{\rm opt}}$, corresponding to the stellar mass, M_* (see also appendix 7), by applying a photometric

[2] ⟨http://www.stsci.edu/hst/observatory/cdbs/bpgs.html⟩.
[3] ⟨http://www.ifa.hawaii.edu/users/pickles/AJP/hilib.html⟩.

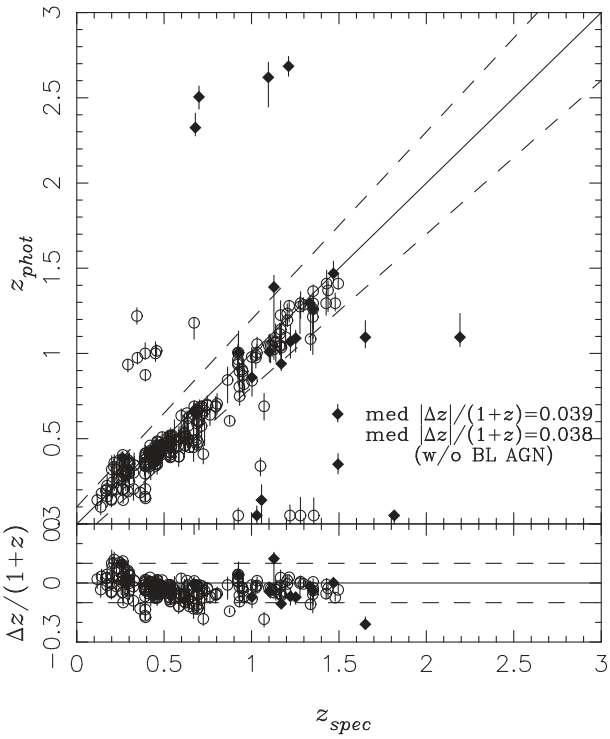

Fig. 1. Comparison between spectroscopic and photometric redshifts for z'-detected galaxies with spectroscopic observations. Filled diamonds and open circles represent objects with and without broad line emissions in their spectra, respectively. Dashed lines represent a deviation with $\Delta z/(1+z_{\rm spec}) = 0.1$.

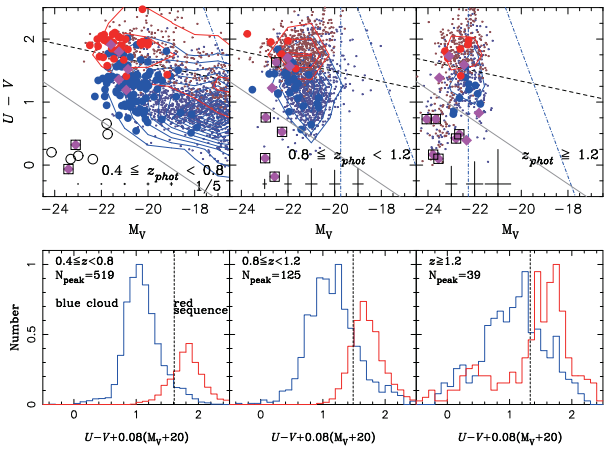

Fig. 2. Rest-frame color $U - V$ for the spectroscopic sample and z'-detected galaxies. Top: Rest-frame Color–Magnitude Diagrams (CMDs) of absolute V-band magnitude vs. $U - V$ color. Objects in redshift ranges of $0.4 \leq z < 0.8$, $0.8 \leq z < 1.2$, and $1.2 \leq z$ are represented from the left to the right. Large symbols represent the spectroscopic sample. Red and blue symbols represent lower and higher *SFR* populations with $sSFR < 0.1\,{\rm Gyr}^{-1}$ and $sSFR > 0.1\,{\rm Gyr}^{-1}$ derived from the SED fitting, respectively. Magenta diamonds represent BL AGNs, in which diamonds in squares represent outlier BL AGNs with $\Delta z/(1+z_{\rm spec}) > 0.2$ in the redshift comparison. Small dots represent the remainder in the z'-detected galaxies. Red and blue contours represent the distribution of lower and higher *SFR* population in the z'-detected galaxies with $sSFR < 0.1\,{\rm Gyr}^{-1}$ and $sSFR > 0.1\,{\rm Gyr}^{-1}$, respectively. Dashed lines represent Bell's color boundary between star-forming and passive populations. Plain black crosses around $U - V \simeq -0.2$ represent typical errors of estimated colors and mass. The vertical and steep slope blue dotted-dashed lines represent the limiting absolute V and U-bands magnitudes at the mean redshift, respectively. The solid mild slope lines represent the boundary with the criterion of equation (2) for EBOs. Open circles represent a population categorized as type 1 QSOs at $z = 0.2$–0.7 in the catalogue of the SDSS/SWIRE sample by Hatziminaoglou et al. (2005). Bottom: Color distributions of the z'-detected galaxies. The color is scaled as $(U - V) + 0.08(M_V + 20)$. Red and blue lines represent lower and higher *SFR* populations with $sSFR < 0.1\,{\rm Gyr}^{-1}$ and $sSFR > 0.1\,{\rm Gyr}^{-1}$ derived from the SED fitting, respectively.

redshift code, *hyperz* (Bolzonella et al. 2000). This is based on a comparison of the observed ground-based $u^*BVRi'z'JK_{\rm s}$ photometry with a grid of stellar population synthesis models produced from Bruzual and Charlot (2003). From this BC03 model we prepared SED templates of a total of nine star-forming history models with exponential decaying star formation as $SFR(t) \propto \exp(-t/\tau)$, with time scales for the star formation activity of $\tau = 0.1$, 0.3, 1, 2, 3, 5, 15, and 30 Gyr; we also varied the age, t, from 0 to 20 Gyr, and included the Constant Star Formation (CSF) model. All of the models are for solar metallicity. With the variations of $E(B - V) = 0$, 0.1, 0.2, 0.3, 0.4, 0.5, and 0.6, we additionally applied Allen's Milky Way, Seaton's Milky Way, LMC, SMC, and Calzetti's extinction curves, to obtain the extinction, A_V. In selecting the best fitting one from five extinction curves for each object, firstly we determined a median photometric redshift, $z_{\rm m}$, in five of them related to these extinction models, and secondly used one model with reduced χ^2 minimization as the photometric redshift, which should be within $0.2(1 + z_{\rm m})$ around the median, $z_{\rm m}$. We adopted a Salpeter initial mass function (IMF) from 0.1 to 100 $M_\odot$ throughout this work.

In the AKARI NEP Deep field, we also obtained spectra with the KeckII/DEIMOS, the Subaru/FOCAS, and the MMT/Hectospec for 420, 57, and 62 objects, which were selected from objects with $R < 24$, < 24, and < 22 mag, respectively. The KeckII/DEIMOS and the Subaru/FOCAS observations partially covered the NEP Deep field, while the MMT/Hectospec observations covered the NEP Deep field by two, 1 deg^2 multi-object configurations. More details on the MMT/Hectospec observations can be found in Ko et al. (2012). They were mostly detected as IR sources with AKARI (Takagi et al. 2010). We obtained 292 spectra for the z'-detected galaxies, in which we could determine secure redshifts for 230 objects that were detected with more than two lines, or clearly with the [O II] line. They included 27 galaxies harboring AGN with Broad Line (BL) emissions, which are spectroscopically classified as BL AGNs. Figure 1 shows a comparison between the spectroscopic and photometric redshifts of the 230 objects and their redshift discrepancy, $\Delta z = z_{\rm phot} - z_{\rm spec}$. The median accuracies of $\langle \Delta z \rangle/(1 + z_{\rm spec})$ are 0.041 and 0.038 for the spectroscopic samples without and with excluding the BL AGNs, respectively. In the spectroscopic sample, there are 22 and 52 outliers with $\Delta z/(1 + z_{\rm spec}) > 0.2$ and > 0.1, in which 11 and 12 out of these outliers are BL AGNs, respectively. Thus, the photometric redshifts are consistent with their spectroscopic ones not only for the samples, except BL AGNs, but also for even half of the BL AGNs. The outlier BL AGNs, except one, are confirmed as Extremely Blue

Objects (EBOs) in the rest-frame Color–Magnitude Diagrams (CMDs), which were selected with a criterion:

$$(U - V) < -0.25(M_V + 22.0) + 0.7\,, \quad (2)$$

as shown in figure 2. If EBOs are type 1 AGNs, this trend is reasonable, since SED models of the AGNs were not included in SED fittings for the photometric redshift estimations.

The AKARI MIR colors can alternatively extract candidates associated with dusty AGN activities, in which we spectroscopically observed 14 agn-Mb*N3*Rs and 2 s/a-Mb*N3*Rs (see the details about them in subsection 6.1). We could confirm that 8 out of 14 agn-Mb*N3*Rs and 2 out of 2 s/a-Mb*N3*Rs show a discrepancy with $\Delta z/(1 + z_{\rm spec}) > 0.1$, respectively. All of these outliers were also identified as BL AGNs, in which 7 out of 8 agn-Mb*N3*Rs and 2 out of 2 s/a-MB*N3*Rs were classified as the EBOs, respectively. As long as their redshifts were correctly obtained with spectroscopy, the overlap of the EBOs with the agn-Mb*N3*Rs suggests that the dust emission detected as the agn-Mb*N3*Rs should coexist with optically blue emission classified as the EBOs in all of them. This supports not only the above expectations that AGNs are harbored in the EBOs and the agn-Mb*N3*Rs, but also a picture of a dusty torus surrounding an AGN, which can explain the variation of their SEDs, as frequently proposed in the AGN unified theory.

We also checked the redshift discrepancy, Δz, in various populations subclassified not only with the spectroscopy, but also with NIR and MIR photometry as *N3*Rs and Mb*N3*Rs, which are summarized in appendix 3. Even though most of the spectroscopic samples were mainly selected from dusty populations with heavy extinction as Mb*N3*Rs detected in the AKARI MIR photometry, their median accuracies of $\langle\Delta z\rangle/(1 + z_{\rm spec})$ are less than 0.05 for any subclassified populations of *N3*Rs and Mb*N3*Rs, except for agn-Mb*N3*Rs. Their photometric redshifts can be estimated well from the SED fitting with their major stellar emission of the host galaxies, in which the extinctions might not be a serious matter. Thus, the estimated photometric redshifts even for most of the galaxies can be used to reconstruct approximately their actual redshifts within $\Delta z/(1 + z_{\rm spec}) < 0.05$.

4.2. Reconstructions of Rest-Frame Magnitudes and Colors

From the derived photometric redshifts, $z_{\rm phot}$, with the optical–NIR SED fittings, we could also estimate rest-frame magnitudes and colors of the z'-detected galaxies. For an object at a redshift z, a magnitude $m_{\lambda_0}(z)$ at a rest-frame wavelength, λ_0, is approximately interpolated from the observed magnitudes, as

$$m_{\lambda_0}(z) = \frac{[\lambda_{\rm r} - \lambda(z)]m_{\rm b} + [\lambda(z) - \lambda_{\rm b}]m_{\rm r}}{\lambda_{\rm r} - \lambda_{\rm b}}\,, \quad (3)$$

$$\lambda(z) = \lambda_0(1 + z)\,, \quad (4)$$

where $m_{\rm r}$ and $\lambda_{\rm r}$ ($m_{\rm b}$ and $\lambda_{\rm b}$) are the observed magnitudes and central wavelengths of the band neighboring the red-side (blue-side) of the observing wavelength, $\lambda(z)$. By using the rest-frame magnitudes derived with $z_{\rm phot}$, CMDs for the z'-detected galaxies could be obtained. The CMD is fundamentally almost the same as the color–mass diagram, which is a powerful tool for studying galaxy evolution, since it shows the bimodal galaxy distribution as early types concentrate in a tight red sequence, while late types distribute in a blue dispersed cloud. This has been studied not only in the local universe with the SDSS (Blanton et al. 2003), but also in the distant universe with surveys for $z < 1$ (Bell et al. 2004; Faber et al. 2007; Borch et al. 2006) and for $z > 1$ (Pannella et al. 2009; Brammer et al. 2009).

Figure 2 shows CMDs of the absolute V-band magnitude M_V and $U - V$ color. We display rest-frame V-detected galaxies on the CMD, and exclude objects with less photometric accuracy of $S/N < 2$ in the rest-frame V band. The rest-frame $U - V$ color straddles the Balmer/4000 Å break, and is also essential to introduce classifications for their stellar populations in IRBGs, Mb*N3*Rs, Mm*N3*Rs, and BBGs, as discussed in the following sections and appendixes. This interpolation scheme, applied for the z'-detected galaxies with $z = z_{\rm phot}$, can be used to derive their M_V and rest-frame $U - V$ colors. In figure 2, we can see that the distribution of galaxies is bimodal up to $z \simeq 1$, as previously shown (Bell et al. 2004; Faber et al. 2007; Borch et al. 2006). In figure 2, we can see that the red sequence and the blue cloud are separated by the following criterion:

$$(U - V) = 1.15 - 0.31z - 0.08(M_V - 5\log h + 20)\,, \quad (5)$$

which is introduced for the definition of red sequence galaxies by Bell et al. (2004), and represented as dashed lines on the CMDs in figure 2. Thus, our catalogue of z'-detected galaxies with photometric redshifts is basically the same as those of other blank-sky surveys.

5. Classification with IR Bump

From the sample of z'-detected galaxies including the Balmer Break Galaxies (BBGs; see the details in appendix 1), we extracted IR classified subpopulations with AKARI/IRC photometry. NIR IRC photometry can select IR bump Galaxies (IRBGs) that have a bump at around 1.6 μm with AKARI (Takagi et al. 2007) and Spitzer (Berta et al. 2008). Both the IRBGs and the BBGs are characterized mainly by emission from the stellar components. In this section, we present three redshifted populations selected by criteria of the IR bump at 1.6 μm, combining the Balmer break. In fact, the selection with 1.6 μm can reduce contamination from the low-z interlopers in the IRBGs at $z > 0.4$, which is also useful to classify MIR-bright populations. We also try to select AGN candidates as outliers with NIR colors redder than normal IRBGs.

5.1. AKARI NIR Color–Color Diagram and 1.6 μm Bump

A bump centered at 1.6 μm in the rest-frame is a major SED feature of galaxies, except for the youngest ones for ages < 10 Myr, in which stellar components are dominated by type-M stars. The 1.6 μm IR bump is produced by combining the spectral peak in black-body radiation from low-mass cool stars as M stars and a minimum in the opacity of H^- ion present in their stellar atmospheres with molecular absorptions (John 1988). Universally appearing in most galaxies, the IR bump is one of the most useful SED features in their photometric measurements (Simpson & Eisenhardt 1999; Sawicki 2002).

AKARI NIR photometry in the *N2N3N4* bands can trace the IR bump at $z = 0.4$–2. We show the redshift tracks of BC03

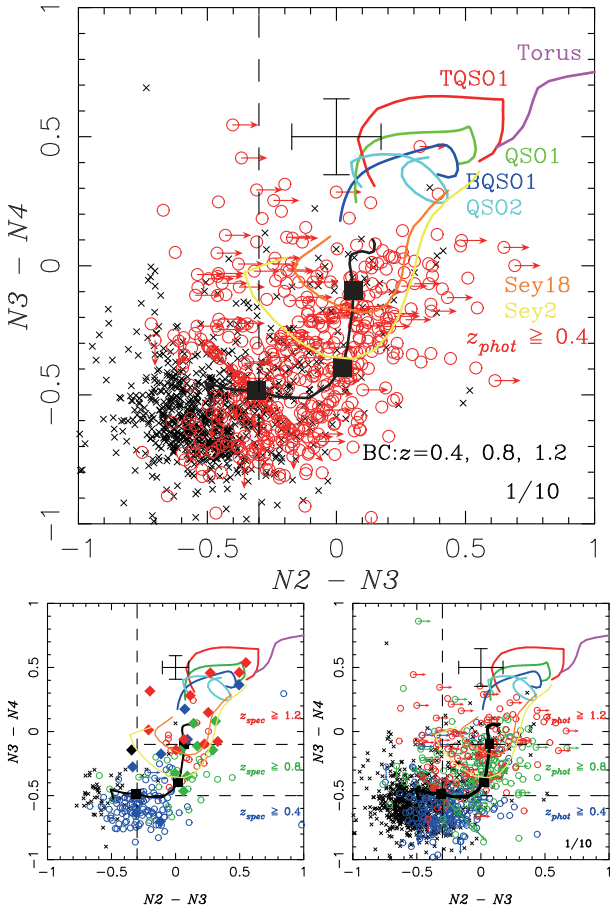

Fig. 3. Two-color diagram of *N2* − *N3* vs. *N3* − *N4* in the field. Symbols of cross bar at (*N2* − *N3*, *N3* − *N4*) = (0.1, 0.5) represent typical errors of the color. A black line is superimposed as a redshifted track of a BC03 model galaxy with $\tau = 1$ Gyr and age = 1 Gyr, on which the squares are related to the redshifts of $z = 0.4$, 0.8, and 1.2 from lower-left to upper-right. Other superimposed green, red, blue, cyan, and magenta lines are tracks of QSO1, TQSO1, BQSO1, QSO2, and dusty torus IR templates, respectively. The redshift from $z = 0$ to $z = 2$ corresponds to the upper-right to the lower-left along each line. Top: For objects detected in the *N2*, *N3*, and *N4* bands. Arrows represent objects that are fainter than the threshold limit in the *N2* or *N4* band. Red open circles and black crosses represent objects at $z_{\rm phot} \geqq 0.4$ and $z_{\rm phot} < 0.4$, respectively. Bottom-left: For spectroscopic samples. Blue, green, and red symbols represent objects at $0.4 \leq z_{\rm spec} < 0.8$, $0.8 \leq z_{\rm spec} < 1.2$, and $z_{\rm spec} \geqq 1.2$, respectively. Diamonds represent BL AGNs. Bottom-right: Same as on the left for the photometric samples.

model galaxies with $\tau = 1$ Gyr and age = 1 Gyr on a two-color diagram of *N2* − *N3* vs. *N3* − *N4* in figure 3, where the filled squares on the tracks represent the redshifts at $z = 0.4$, 0.8, and 1.2 from the bottom-left to the top-right. The tracks are mostly parallel to the *N2* − *N3* axis up to $z \simeq 0.8$, bending upward around $z \simeq 0.8$, and are vertical along the *N3* − *N4* axis at $z \simeq 0.8$–1.2. This trend can be understood as an excess of the redshifted IR bump on the *N2* side in the *N3* band at $z \simeq 0.4$–0.8, the *N4* side in the *N3* band at $z \simeq 0.8$–1.2, and in the *N4* band at $z > 1.2$. The redshift is the dominating factor in determining the AKARI NIR color tracks of galaxies without AGNs, while the galaxy type is less effective.

Table 3. Parameters for IRBG selections.

IRBGs	f_{N23}	$\min_{N34}$	$\max_{N34}$	$z_{\rm min}$	$z_{\rm max}$
*N3*R	−0.3	—	—	0.4	—
N23	−0.3	—	−0.5	0.4	0.8
N34	−0.3	−0.5	−0.1	0.8	1.3
N4R	−0.3	−0.1	—	1.3	—

First, we extract *N3*-detected ones as *N3* Red galaxies (*N3*Rs), possibly at $z > 0.4$ from the z'-detected galaxies with the criterion

$$N2 - N3 > f_{N23} \, . \tag{6}$$

Second, we can also subclassify the *N3*Rs into *N23*, *N34*, and *N4* bumpers, which are defined as IRBGs of their IR bump detected with the *N2* and *N3* bands, the *N3* and *N4* bands, and the *N4* band in three redshift ranges of $z \simeq 0.4$–0.8, $z \simeq 0.8$–1.2, and $z > 1.2$, respectively. The color criteria are represented as

$$N2 - N3 > f_{N23} \cap \ \min_{N34} \leq N3 - N4 < \max_{N34} \, , \tag{7}$$

where the parameters of f_{N23}, $\min_{N34}$, and $\max_{N34}$ are given in table 3.

The bottom-left of figure 3 represents a two-color diagram for the spectroscopic sample in the field, in which most of the galaxies at $z_{\rm spec} \simeq 0.4$–0.8, 0.8–1.2, and > 1.2 appear as *N23*, *N34*, and *N4* bumpers, respectively. The bottom-right of figure 3 also represents another two-color diagram for a photometric sample in the field, in which the NIR colors of galaxies at $z_{\rm phot} \simeq 0.4$–0.8, 0.8–1.2, and > 1.2 distribute around the regions of *N23*, *N34*, and *N4* bumpers, respectively.

When a galaxy harbors an AGN, however, IR emission from the dusty torus around the AGN affects the NIR colors. We also superimposed tracks of redshifted QSO SED templates in the SWIRE library:[4] three types of optically-selected type 1 QSOs (QSO1, TQSO1, and BQSO1) and two models of type 2 QSOs (QSO2 and Torus). All of them show dominant emissions from the dusty torus at IR wavelength $\lambda > 1\,\mu$m. Thus, the NIR color criterion from equation (6) can be still effective for selecting not only galaxies at $z > 0.4$, but also AGN candidates. Furthermore, all of the QSO tracks overlap with the region of the *N4* bumpers. In fact, most of the BL AGNs, selected by spectroscopy, appear around the region of the *N4* bumpers. Thus, the *N3*Rs with $N3 - N4 > -0.1$ may include not only the *N4* bumpers of IRBGs, but also these AGN candidates, which will also be confirmed with the MIR classified AGNs in section 6. We designate the *N3*Rs with $N3 - N4 > -0.1$ as *N4* Red galaxies (*N4*Rs).

5.2. *N3Rs Subclassified with Balmer Break*

As shown in figure 3, both spectroscopic and photometric redshifts of the *N3*Rs are almost consistent with the NIR color criterion $N2 - N3 > -0.3$ of the IR bump at $z > 0.4$. As mentioned in subsection 4.1, the photometric redshifts were derived from only the ground-based data without the AKARI NIR data, which means that the selection with the IR bump is

[4] ⟨http://www.iasf-milano.inaf.it/~polletta/⟩.

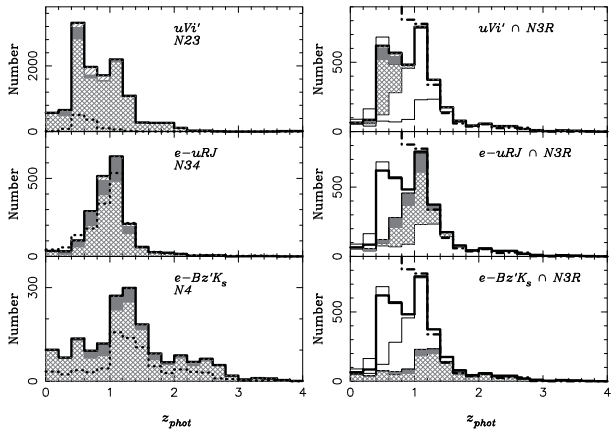

Fig. 4. Photometric redshift distributions for exclusively classified BBGs; e-*BzK*s, exclusively classified e-*uRJ*s from those remaining after exclusion of the e-*BzK*s, and exclusively classified *uVi*s from the remainings after exclusion of both the e-*BzK*s and the exclusively classified e-*uRJ*s, from bottom to top. Shaded, single-hatched, and cross-hatched areas represent p-, qp-, and s-BBGs. Left: For exclusively classified BBGs and IRBGs. The dotted lines represent *N23* bumpers, *N34* bumpers, and *N4*Rs, from top to bottom. Right: For *N3* Red BBGs. The dotted-dashed, thin solid, and thick solid lines represent the rest-frame *V*-detected galaxies, the *N3*Rs, all the *N3* Red BBGs, respectively.

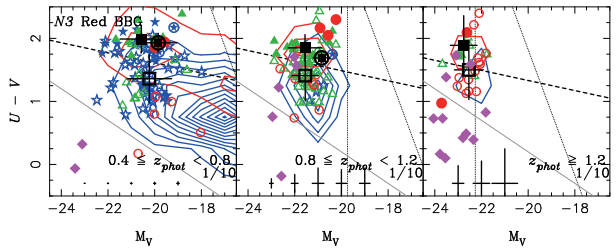

Fig. 5. Same as figure 2 for *N3* Red BBGs. The plots for $0.4 < z < 0.8$, $0.8 < z < 1.2$, and $1.2 < z$ are from left to right. In general, the colored open, solid, and circled symbols represent objects classified as s-, p-, and qp-BBGs, respectively. Basically, red circles, green triangles, and blue stars represent objects selected with the two-color criteria as e-*BzK*s, e-*uRJ*s, and *uVi*s, respectively. Black-large open, solid, and circled symbols represent mean values for the s-, p-, and qp-BBGs, respectively. Crosses on their black symbols represent their standard deviations. Only a part of the samples are plotted to reduce crowding in the diagram, whose fractions are presented as numbers in the right-bottom region of all figures.

independent of the photometric redshifts. Thus, the color criterion with $N2 - N3 > -0.3$ is useful in order to exclude low redshift interlopers at $z < 0.4$ in the IRBGs, as long as they are detected in the *N2* (or *K*) and *N3* bands, as discussed in subsection 5.1. Furthermore, adding the AKARI/NIR photometry to the ground-based optical–NIR photometry can salvage the BBGs in the IRBGs, as shown in appendix 1.3. These are the merits of using AKARI/NIR photometry with the ground-based photometry.

On the other hand, even though the IR bump criteria of *N23* and *N34* bumpers, and *N4*Rs correspond to three redshift intervals, as shown in figure 3, they cannot be robust for the redshift subclassification, since the *N4*Rs possibly include AGNs, as discussed in subsection 6.2. In redshift subclassifications, optical color criteria with the Balmer break are more reliable than those of the $N3 - N4$ colors with the IR bump. As described in appendix 1, we generalized the color criteria of *BzK*s at $1.4 < z < 2.5$ with *BzK* filter set (Daddi et al. 2004) to select BBGs at $0.8 < z < 1.8$ and $0.4 < z < 0.8$ by using *uRJ* and *uVi* filter sets, called as *uRJ*s and *uVi*s, respectively. Furthermore, we selected extended BBGs as e-*BzK*s and e-*uRJ*s with *N3* band photometry, which is the deepest one in the IRC bands (see appendix 1.3). However, these e-*BzK*s, e-*uRJ*s, and *uVi*s overlap each other. Thus, we introduced an exclusive subclassification of BBGs, as first selecting the *BzK* criteria, second applying the *uRJ* criteria for those remaining after exclusion of the *BzK*s, and finally applying the *uVi* criteria for those remaining after exclusion of the *uRJ*s and the *BzK*s. As shown on the left in figure 4, the redshift distributions of the exclusively classified BBGs, except for the *uVi*s, are similar to those of IRBGs, since the *uRJ*s and the *BzK*s correspond to the *N34* bumpers and the *N4*Rs, respectively. Most counterparts of the MIR bright populations at $z > 0.4$, detected by AKARI MIR photometry in the field, are identified as the *N3*Rs. Thus, hereafter, we will take a subclassification of the *N3*Rs into the star-forming (s-), passively evolving (p-), and quasi passively evolving (qp-) BBGs with the exclusive subclassification. We name these BBGs exclusively subclassified from the *N3*Rs as *N3* Red BBGs (*N3*RBBGs); *N3*R*BzK*s, *N3*R*uRJ*s, and *N3*R*uVi*s. The redshift distributions of *N3*RBBGs are also shown on the right in figure 4. Figure 5 shows the CMD of M_V and $U - V$ for these *N3*RBBGs. We can see that the subclassification of the s-, p-, and qp-*N3*RBBGs is consistent with that using Bell's color boundary in figure 5.

Since *N3* band photometry is the deepest one in the IRC bands, as discussed in appendix 1.3, the *N3*RBBGs salvaged with the *N3* photometry are almost the same selected population as the rest-frame *V*-detected galaxies at $z > 0.4$. It can be confirmed, since both of them show a similar redshift distribution, as shown in figure 4. The rest-frame *V*-detected galaxies are a kind of referenced sample as frequently plotted with the referenced contours on the CMDs in figures 2 and 5 (see also figures 48 and 50 in appendix 1). Thus, the *N3*RBBGs are suitable in the study for their stellar populations by using the CMD, even in MIR bright populations, as can be seen in section 6.

6. Classifications with MIR SEDs

MIR multi-band photometry with the IRC has identified MIR-bright populations in the *N3*Rs, as detected with $S/N > 3$ in MIR bands and classfied into starbursts or AGNs with two MIR color diagrams, which are called as Mb*N3*Rs. IRC MIR photometry can detect PAH emissions from dusty star-forming regions for a subgroup in the IRC detected Mb*N3*Rs. The subgroup with the PAH features can be classified with the MIR colors as starbursts, which are overlapped with the PAH luminous galaxies in some companion papers (Takagi et al. 2007, 2010, 2012). Another subgroup of Mb*N3*Rs without any PAH features, or with weak ones, is possibly AGN dominant. Some of them may overlap with Power-Law Galaxies (PLGs) and IR Excess Galaxies (IREGs), which are already classified with Spitzer as AGN-dominant populations. The former has

MIR SEDs well fitted by a power law (Lacy et al. 2004; Stern et al. 2005; Alonso-Herrero et al. 2006; Donley et al. 2007). The latter shows the large IR-to-UV/optical flux ratio (Daddi et al. 2007; Dey et al. 2008; Fiore et al. 2008; Polletta et al. 2008), in which some may be identified as sources with heavily obscured optical emissions. The Mb*N3*Rs and their relatives at $z > 0.4$, detected in the field, typically have TIR luminosities of $> 10^{11} L_{\odot}$, which correspond to those of LIRGs/ULIRGs, as shown in appendix 4. In this section, thus, we mainly consider the subclassification for the Mb*N3*Rs and their relatives by analyzing the MIR and NIR SEDs as preparing to reveal star-forming and AGN activities of LIRGs/ULIRGs at $z > 0.4$ in the following sections.

6.1. *Starburst and AGN in MIR Bright N3Rs*

AKARI/IRC MIR photometry, in the *S7*, *S9W*, *S11*, *L15*, *L18W*, and *L24* bands, is capable of tracing the features of PAH emissions at 3.3, 6.2, 7.7, and 11.3 μm and Si absorption at 10 μm (rest-frame) from dusty starbursts in the Mb*N3*Rs. The MIR two-color diagrams of *S9W* − *S11* vs. *S11* − *L15* (*S9W*/*S11*/*L15*) and *S11* − *L15* vs. *L15* − *L18W* (*S11*/*L15*/*L18W*) are useful to trace the redshifted PAH features, since the strong PAH 7.7 μm emission (the dip between PAH 6.2 and 7.7 μm) enters into the *L15* (*S11*) band for higher-redshifted dusty starbursts in a redshift range of $z = 0.4$–2.6. In order to characterize the MIR SED features for the Mb*N3*Rs, we present their observed colors on two-color diagrams of *S9W*/*S11*/*L15* and *S11*/*L15*/*L18W*, as shown in figure 6. In order to classify them in the MIR two-color diagram. we selected $\sim$600 Mb*N3*Rs from the *N3*Rs with the detection of $S/N > 3$ in the MIR bands.

Dusty starburst Mb*N3*Rs (s-Mb*N3*Rs) are distinguished from AGN-dominated ones (agn-Mb*N3*Rs) with solid lines in figure 6 as the boundary between the two populations, which were derived from the redshifted tracks of their MIR SEDs (see figure 63 in appendix 5). On the other hand, the agn-Mb*N3*Rs were selected with MIR color criteria in each of the redshift interval classes, which are

$$(S9W - S11) < 0.3 \cap (S11 - L15) > 0.0 \quad (8)$$

at $z = 0.4$–1.0,

$$(S9W - S11) < 0.3 \cap (S11 - L15) < -1.5(S11 - L15) + 1.2 \quad (9)$$

at $z = 0.8$–1.4,

$$(S11 - L15) < 0.8 \cap (L15 - L18W) < 0.3 \quad (10)$$

at $1.0 < z < 2.8$. Assuming that the Mb*N3*Rs are at photometric redshift $z_{\rm phot}$ derived in subsection 4.1, the classification criteria at $z = 0.4$–1.0, $z = 0.8$–1.4, and $1.0 < z < 2.8$ were applied for the Mb*N3*Rs with photometric redshifts of $0.4 \leq z_{\rm phot} < 0.8$, $0.8 \leq z_{\rm phot} < 1.2$, and $1.2 \leq z_{\rm phot}$, respectively, as shown in figure 6. The three redshift intervals roughly correspond to *N3* Red *uVi*s (*N23* bumpers), *uRJ*s (*N34* bumpers), and *BzK*s (*N4R*s) in *N3* Red BBGs (IRBGs), respectively. Even with substitution of the photometric selections as the BBGs (IRBGs) for the redshift selections, the MIR two-color diagrams can be also applied to distinction between dusty starbursts and AGNs.

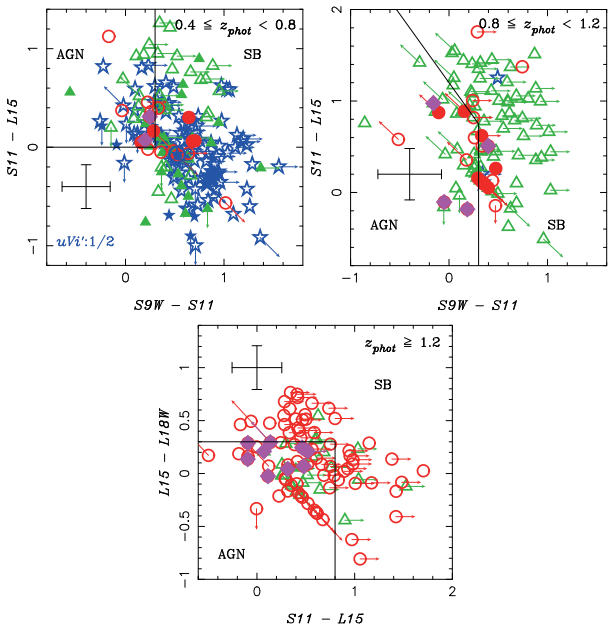

Fig. 6. MIR color–color diagrams for the Mb*N3*Rs, which are also subclassified into s/p/qp-BBG/*N3*Rs and BL AGNs. Blue stars, green triangles, and red circles represent s(p)-*uVi*s, s(p)-(*uRJs*+*uRN3*s+*BRN3*s), and s(p)-(*BzKs*+*uzN3*s+*BzN3*s) (see appendix 1.3). In general, the colored open and filled symbols and filled symbols in circles represent objects classified as s-, p-, and qp-BBGs, respectively. Magenta diamonds represent the spectroscopic BL AGNs. Top-left: *S9W* − *S11* vs. *S11* − *L15* diagram for the observed Mb*N3*Rs at $0.4 \leq z < 0.8$. Top-right: Same as the top-left, for the Mb*N3*Rs at $0.8 \leq z < 1.2$. Bottom: *S11* − *L15* vs. *L15* − *L18W* diagram for the Mb*N3*Rs at $z \geq 1.2$.

We also fitted this AKARI/IRC photometry for the s-Mb*N3*Rs observed at the 7–24 μm wavelength with the SED templates of starbursts (Siebenmorgen & Krügel 2007) (hereafter S&K model, see also appendix 5.4). Even though we could roughly distinguish s-Mb*N3*Rs and agn-Mb*N3*Rs only with the AKARI MIR colors, since their MIR emissions are dominant from dusty starburst and AGN, we could also miss some AGNs hidden in the s-Mb*N3*Rs with dusty starbursts. In order to classify the s-Mb*N3*Rs into two subgroups of starburst dominants and starburst/AGN coexisting, we performed the MIR SED fitting with composite SED models, in which the dusty torus model in the SWIRE library was added to the dusty starburst S&K model with mixing rates of 10, 20, 30, 40, 50, 60, 70, 80, 90, and 100% in the rest-frame 5-μm luminosity. We selected sb-Mb*N3*Rs and s/a-Mb*N3*Rs with the mixing rates of the dusty torus $< 50\%$ and $\geq 50\%$ as starburst-dominants and starburst/AGN coexisting, respectively, derived from the MIR SED fitting. The MIR SED fitting results for the Mb*N3*Rs are consistent with their simple MIR color classification, since Mb*N3*Rs fitted well with the high AGN mixing rate, which overlapped with the agn-Mb*N3*Rs classified by the MIR color. Figure 7 shows the SEDs normalized at 1.6 μm for sb-, s/a-, and agn-Mb*N3*Rs, where we had estimated the rest-frame monochromatic magnitudes (luminosities) with their

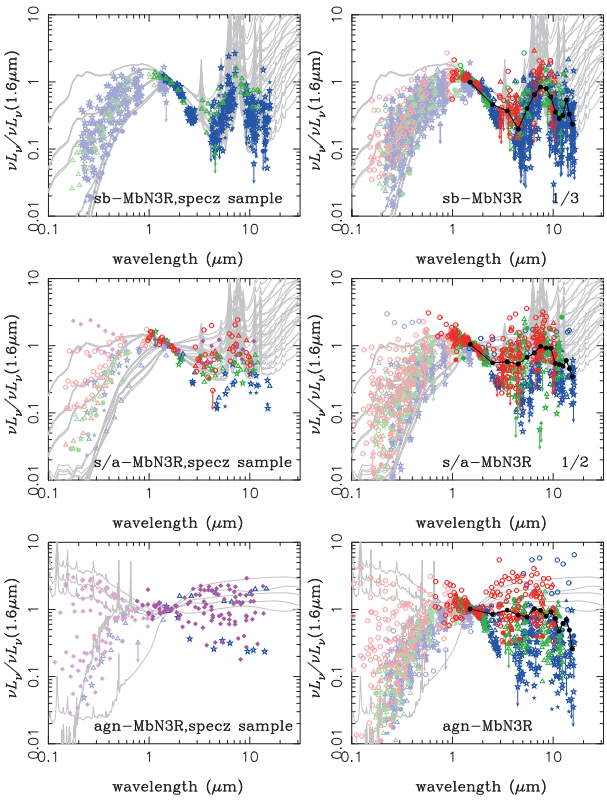

Fig. 7. Rest-frame SED normalized at 1.6 μm for the Mb*N3*Rs. The symbols are the same as figure 6 except for their colors. Blue, green, and red symbols represent the redshifts of $0.4 \leq z < 0.8$, $0.8 \leq z < 1.2$, and $z \geq 1.2$, respectively. Dark and faint symbols represent AKARI IRC photometric data and ground-based photometric data, respectively. The averaged observed MIR SEDs are represented by solid lines in the figures on the right. Top-left: For the sb-Mb*N3*Rs in the spectroscopic sample. Superimposed lines represent dusty starburst SED templates of the S&K model used in the MIR SED fitting. Top-right: Same as on the left for the sb-Mb*N3*Rs in the photometric sample. Middle-left: Same as the top-left for the s/a-Mb*N3*Rs in the spectroscopic sample. Superimposed lines represent SEDs composed of the S&K model and the dusty torus model in the SWIRE SED library with the ratio of 0.3 to 0.7 at 5 μm. Middle-right: Same as on the left for the s/a-Mb*N3*Rs in the photometric sample. Bottom-left: Same as the top-left for the agn-Mb*N3*Rs in the spectroscopic sample. Superimposed lines represent the SWIRE SED templates of dusty torus, QSO2, BQSO1, TQSO1, and QSO1 from top to below at long wavelength. Bottom-right: Same as on the left for the agn-Mb*N3*Rs in the photometric sample.

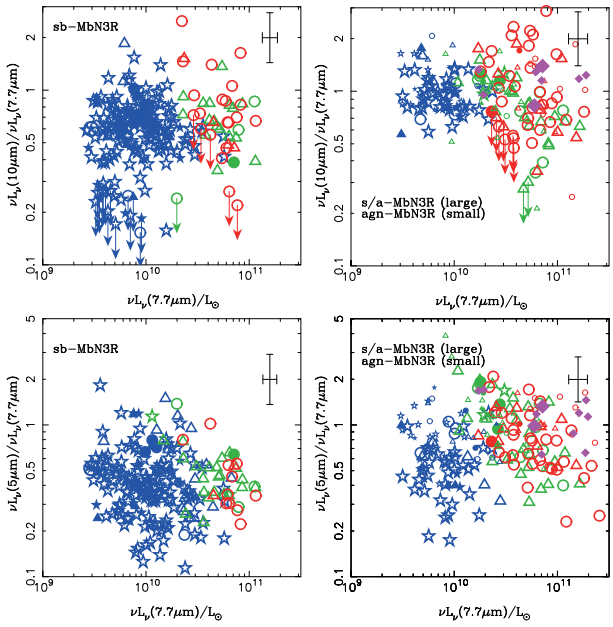

Fig. 8. Correlation between the monochromatic luminosity, $\nu L_{\nu,7.7}$, at the rest-frame 7.7-μm and the ratio of monochromatic luminosities. The symbols are the same as figure 6, except for their colors and sizes. The blue, green, and red symbols represent the redshifts of $0.4 \leq z < 0.8$, $0.8 \leq z < 1.2$, and $z \geq 1.2$, respectively. Small symbols represent the agn-Mb*N3*Rs classified by the MIR colors. Top: Ratio of the monochromatic luminosity, $\nu L_{\nu,10}$, at the rest-frame 10 μm to the $\nu L_{\nu,7.7}$. Bottom: Ratio of the monochromatic luminosity, $\nu L_{\nu,5}$, at the rest-frame 5 μm to the $\nu L_{\nu,7.7}$. Left: For the sb-Mb*N3*Rs. Right: For the s/a- and the agn-Mb*N3*Rs. Large and small symbols represent the s/a- and agn-Mb*N3*Rs, respectively.

spectroscopic and photometric redshifts. For the photometric sb-, s/a-, and agn-Mb*N3*Rs, their averaged MIR SEDs were also derived, as shown by black lines on the right side.

Rest-frame SEDs of the sb-Mb*N3*Rs, as shown in figure 7, show deep dips at around 5 and 10 μm, and a strong excess at around 8 μm with weak ones at around 3 and 11 μm. The features agree well with the SEDs of the dusty starburst S&K model overplotted as thin lines. This indicates not only the consistency for this starburst classification with MIR colors and MIR SED fittings, but also accuracy for their photometric redshifts. On the other hand, the features are not so clear for the agn-Mb*N3*Rs. The 5 μm dip corresponds to the transition between the stellar emission and the dust emission from their star-forming regions. The strong excess at around 8 μm with weak ones at around 3 and 11 μm and the dip at around 10 μm can also be naturally explained with the PAH 7.7, 3.3, and 11.3 μm emissions and Si 10 μm absorption in typical MIR emission from their dusty star-forming regions.

Figure 8 shows similar trends to those that appear in figure 7, since the dips at rest-frame 5 and 10 μm are deeper in the sb-Mb*N3*Rs than in the s/a- and agn-Mb*N3*Rs. These trends can also be naturally explained since MIR SEDs of s/a-Mb*N3*Rs consist of a smooth power-law or convex component added to an original component with deep concave dips at 5 and 10 μm, which agree well with the superimposed SEDs composed of the dusty starburst S&K model templates and the dusty torus model template in the SWIRE SED library with a ratio of 0.3 to 0.7 at 5 μm. The composition of the starburst and the dusty torus is typically characterized by the monochromatic luminosity ratio of s/a-Mb*N3*Rs, shown in figure 8. This is consistent with a picture of an obscured AGN coexisiting with a dusty star-forming region in an s/a-Mb*N3*R, which contributes to the additional smooth component and emission with 5 and 10 μm dips in the MIR SED, respectively.

6.2. *NIR Colors of MbN3Rs*

The NIR color diagram of figure 9 for the Mb*N3*Rs can also support the existence of a dusty torus hidden in the agn- and s/a-Mb*N3*Rs with excess in the *N4* band. The agn- and

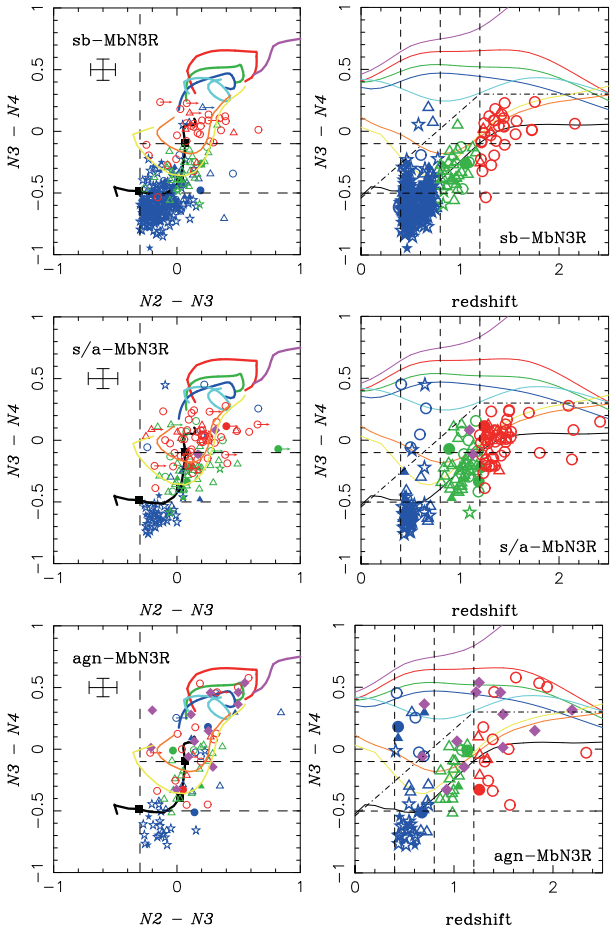

Fig. 9. Left: Same as figure 3 for the Mb*N3*Rs. The symbols are the same as figure 6, except for their colors. The blue, green, and red symbols represent objects at redshifts of $0.4 \leq z < 0.8$, $0.8 \leq z < 1.2$, and $z \geq 1.2$, respectively. Right: Redshift vs. $N3 - N4$ color. Top: For the sb-Mb*N3*Rs. Middle: For the s/a-Mb*N3*Rs. Bottom: For the agn-Mb*N3*Rs.

s/a-Mb*N3*Rs, even at $z < 1$, appear in the region of $N3 - N4 > -0.1$, which is the same trend as for the BL AGNs, and expected from the tracks of the dusty torus and QSO models, as shown in figure 9. For the stellar compornent with the IR bump, the mean $N3 - N4$ color track, represented as solid lines in the right plots of figure 9, can be roughly approxinated as a function, $N3N4(z)$, of z:

$$N3N4(z) = \begin{cases} 0.74z - 0.84 & (0.4 \leq z < 1.2) \\ 0.048 & (z \geq 1.2)\,. \end{cases} \quad (11)$$

Thus, we selected AGN candidates with an NIR color criterion,

$$N3 - N4 > N3N4(z) + \Delta N34\,, \quad (12)$$

where we took a typical $N3 - N4$ color error $\Delta(N3 - N4)$ into account, and introduced $\Delta N34 = 3\Delta(N3 - N4)$. The galaxies, selected with this additional NIR color criterion from the *N3*Rs, will be called *N3N4* Red galaxies (*N3N4*Rs). The boundary of the NIR color criterion is shown as dotted-dashed lines in the right plots of figure 9, where $\Delta(N3 - N4) = 0.1$ as a typical $N3 - N4$ color error for the Mb*N3*Rs, which selects

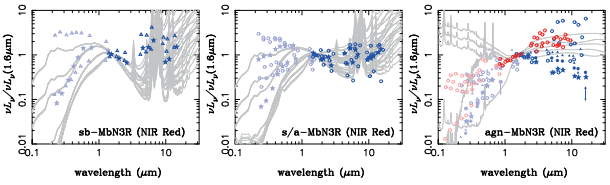

Fig. 10. Same as figure 7 for the Mb*N3N4*Rs. Left: For the sb-Mb*N3N4*Rs. Middle: For the s/a-Mb*N3N4*Rs. Right: For the agn-Mb*N3N4*Rs.

MIR bright *N3N4*Rs (Mb*N3N4*Rs). As shown in figure 10, the SEDs of agn- and s/a-Mb*N3N4*Rs are similar to spectroscopically confirmed BL AGNs in agn-Mb*N3*Rs. The redder color $N3 - N4$ in the agn- and s/a-Mb*N3N4*Rs is consistent with the existence of a dusty torus, which dominates the stellar components of the host. On the other hand, the SEDs of sb-Mb*N3N4*Rs are still similar to those of dusty starbursts like most of the sb-Mb*N3*Rs. The sb-Mb*N3N4*Rs, even with the redder color $N3 - N4$, may still be dusty starburst dominant. Thus, the MIR SED classification for the sb-Mb*N3*Rs is robust to distinguish dusty starbursts from AGNs, while the NIR color classification can be effective only to select bright obscured AGNs.

6.3. *MIR Marginally-Detected N3Rs*

We should remark that MIR multi-band photometry with the IRC can select unique samples for studying star formation and AGN activity, as not only the Mb*N3*Rs, but also sources detected only in some of the *S7*, *S9W*, *S11*, *L15*, *L18W*, and *L24* MIR bands. As shown above, *S11*, *L15*, *L18W*, and *L24* of the IRC are effective in detecting the 7.7 μm PAH emission from dusty starbursts at $z \geq 0.4$. Even though we selected $\sim$600 Mb*N3*Rs with the detection of $S/N > 3$ in more than two MIR bands in subsection 6.1, we also excluded MIR sources in the *N3*Rs, as detected only in one or two MIR bands with the detection of $S/N > 3$, and in other MIR bands with the detection of $S/N < 3$, which are called MIR marginally-detected *N3*Rs (Mm*N3*Rs), whose MIR magnitudes and colors can still be estimated, since the Mm*N3*Rs are mimics of the Mb*N3*Rs. We selected $\sim$600 Mm*N3*Rs, which were subclassified into $\sim$320 possible PAH emitting (pP-)Mm*N3*Rs and $\sim$270 faint PAH emitting (fP-)Mm*N3*Rs. The former can be PAH 7.7 μm emitters, as detected in the *S11*, *L15*, and *L18* bands at $z = 0.4$–0.65, 0.65–1.5, and > 1.5, respectively, while the latter even have MIR emission, but possibly not related to the PAH emissions. Thus, the pP-Mm*N3*Rs and fP-Mm*N3*Rs could be candidates for dusty starbursts and AGN mixtures or less-active star-forming galaxies with and without the PAH emissions in their selection criteria, respectively.

Following the MIR color classifications in subsection 6.1, we checked the difference between the pP- and fP-Mm*N3*Rs on the MIR color–color diagrams, as shown in figures 11 and 12. Even though the errors in the MIR colors of the Mm*N3*Rs are large, most of the pP-Mm*N3*Rs appear in the area of dusty starburst in the MIR color–color diagrams, which are similar to the s-Mb*N3*Rs. On the other hand, the fP-Mm*N3*Rs are more dispersed on the diagrams, which suggests that the

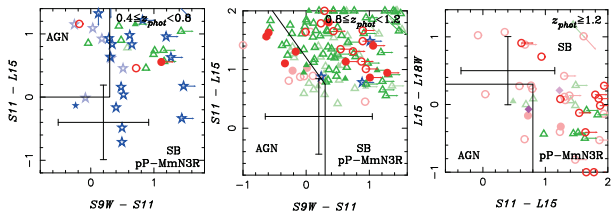

Fig. 11. Same as figure 6 for the pP-Mm*N3*Rs. Dark and faint symbols represent the sb- and non sb- pP-Mm*N3*Rs, respectively.

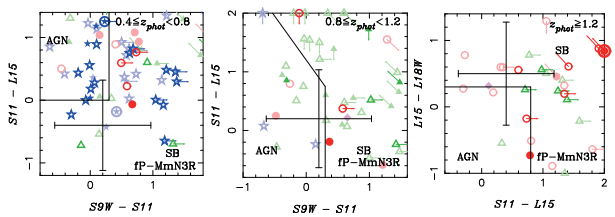

Fig. 12. Same as figure 11 for the fP-Mm*N3*Rs. Dark and faint symbols represent sb- and non sb-fP-Mm*N3*Rs, respectively.

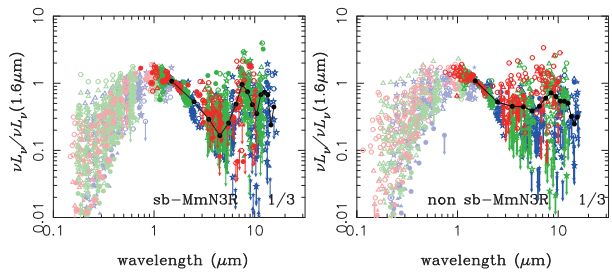

Fig. 13. Same as figure 7 for the Mm*N3*Rs. Left: For the sb-Mm*N3*Rs. Right: For the non sb-Mm*N3*Rs.

fP-Mm*N3*Rs mainly consist of star-forming and AGN mixtures. In order to classify the Mm*N3*Rs into two subgroups of starburst and non starburst, we also performed the MIR SED fitting with the same composite SED models as described in subsection 6.1. We selected sb- and non sb-Mm*N3*Rs with the mixing rates of the dusty torus $< 50\%$ and $\geq 50\%$ in MIR SED fittings as starburst-dominants and possibly non starburst, which are represented as dark and thin symbols, respectively, in figures 11 and 12. Then, we categorized these starburst dominant Mm*N3*Rs (sb-Mm*N3*Rs) as mimics of sb-Mb*N3*Rs.

In fact, $\sim$240 out of $\sim$320 pP-Mm*N3*Rs are sb-pP-Mm*N3*Rs, while only $\sim$110 out of $\sim$270 fP-Mm*N3*Rs are sb-fP-Mm*N3*Rs. Thus, the classifications from the MIR colors for pP-Mm*N3*Rs and fP-Mm*N3*Rs are roughly consistent with those from the MIR SED fittings for sb-Mm*N3*Rs and non sb-Mm*N3*Rs. Figure 13 also shows averaged MIR SEDs of sb-Mm*N3*Rs and non sb-Mm*N3*Rs. We can see that the averaged MIR SED of the sb-Mm*N3*Rs have dusty starburst features with deep dips at around 5 and 10 μm, and excesses at around 8 and 11 μm in the SEDs, which are similar to the sb-Mb*N3*Rs, as shown in figure 7. We can also see these features in the luminosity ratios of $\nu L_{\nu,10}/\nu L_{\nu,7.7}$ and $\nu L_{\nu,5}/\nu L_{\nu,7.7}$, as shown in figure 14. On the other hand,

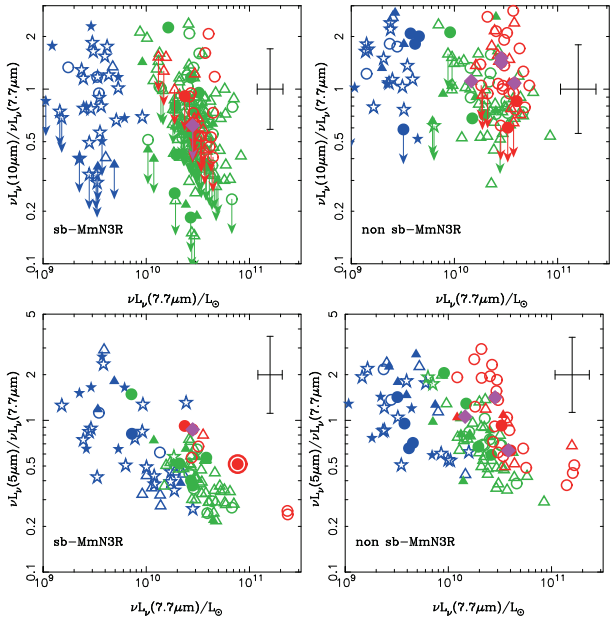

Fig. 14. Same as figure 8 for the sb- and non sb-Mm*N3*Rs.

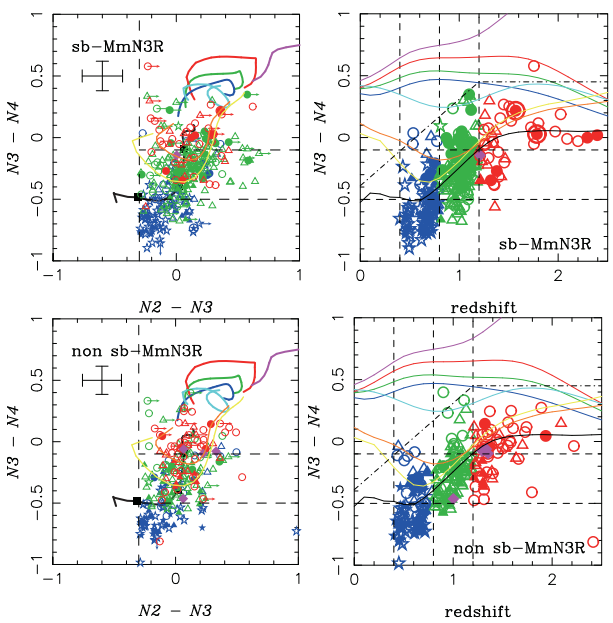

Fig. 15. Same as figure 9 for the Mm*N3*Rs.

the averaged MIR SED and the luminosity ratio of the non sb-Mm*N3*Rs are similar to those of the s/a-Mb*N3*Rs. We also tried to find AGN candidates hidden in the Mm*N3*Rs with the NIR color criterion of equation (12), as applied to the Mb*N3*Rs in subsection 6.1. With $\Delta(N3 - N4) = 0.15$, as a typical $N3 - N4$ color error for the Mm*N3*Rs, the boundary of the criterion with dotted-dashed lines in figure 15 is represented again as same at those in figure 9, which select Mm*N3N4*Rs. As shown in figure 16, the sb- and non sb-Mm*N3N4*Rs are similar to the sb- and agn-Mb*N3N4*Rs, respectively.

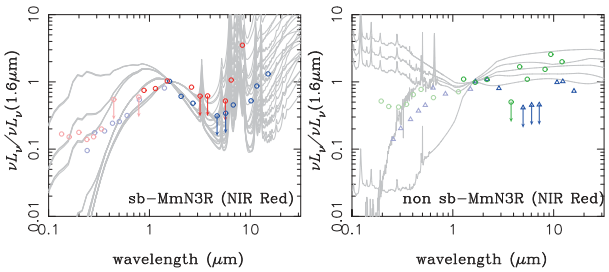

Fig. 16. Same as figure 7 for the Mm*N3N4*Rs.

Thus, the distinction between starbursts and AGNs with features in MIR/NIR SED is basically valid even in the Mm*N3*Rs, which are the same as the Mb*N3*Rs. Thus, we can treat sb-Mm*N3*Rs as mimics of s-Mb*N3*Rs in the following sections.

6.4. *MIR Faint N3Rs and BBGs*

From the opposite point of view to subsections 6.1 and 6.3, weak emission and/or non-detection in these MIR IRC bands are still important constraints for selecting galaxies with low extinction or AGNs with weak dusty torus emission. These MIR faint sources, having less than the limiting magnitudes of those in table 2 in all the MIR bands (*S9*, *S11*, *L15*, *L18W*, and *L24*), can be classified into a subclass population of *N3*Rs, which we call as MIR faint *N3*Rs (Mf*N3*Rs), as alternatives to not only the Mb*N3*Rs, but also the Mm*N3*Rs. The Mf*N3*Rs may in general also consist of star-forming and passive populations in the BBGs with weak dust emission. For example, passive *uVi*s, *uRJ*s, and *BzK*s without the 7.7 μm PAH emission at $0.4 \leq z < 0.8$, $0.8 \leq z < 1.2$, and $1.2 \leq z$ are expected to be faint in the *S11*, *S11*/*L15*, and *L15*/*L18W* bands, respectively. Thus, the Mf*N3*Rs can be subclassified into s- and p-BBGs with the two-color diagram.

The Mf*N3*Rs at $z > 1.2$ form a limited sample in our shallow survey depth in the J, K, and *N3* bands, and they are mostly identical to MIR faint BBGs (MfBBGs). The Mf*N3*Rs at $z < 1.2$ are a part of MIR faint *uVi*s (Mf*uVi*s). In order to study the evolution and mass dependence in star formation, these Mf*N3*Rs and MfBBGs are also important as reference samples compared with the Mb*N3*Rs and Mm*N3*Rs for analyzing their evolutionary features of *SFR*, extinction, and M_* in section 8. We will sometimes refer to MfBBGs as BBGs not classified as Mf*N3*Rs in the following.

6.5. *Comparison with X-Ray and Radio Observations*

Before closing this section, we quickly compare the MIR SED classification with recent results at X-ray and radio wavelengths. AGNs being harbored in the agn-Mb*N3*Rs and the s/a-Mb*N3*Rs are also indicated from a preliminary look at our recent Chandra X-ray Observatory (CXO) data on this field (M. Krumpe et al. in preparation; T. Miyaji et al. in preparation), which show that $\sim 50\%$ of the agn-Mb*N3*Rs and $\sim 15\%$ of the s/a-Mb*N3*Rs have counterparts of X-ray sources. Thus, the trend for the X-ray sources also supports that the MIR SED classification is effective for selecting AGNs. Furthermore, as shown in figure 13, the non sb-Mm*N3*Rs are possibly harboring AGNs with dusty starbursts. If this is true, their X-ray emission can be detected by a stacking analysis of their CXO data. Thus, the CXO data can be effective to study AGN activities not only for the Mb*N3*Rs, but also for the Mm*N3*Rs.

We have also made a radio observation with the WSRT at 1.4 GHz of $\simeq 1.7\,\mathrm{deg}^2$ covering the field, which found $\simeq 500$ sources with > 0.1 mJy in the field (White et al. 2010). The radio source counts are consistent with a two-population model with radio loud sources and radio faint sources with < 1 mJy, in which it was assumed that the former and the latter are powered by AGNs and star-forming galaxies, as in previous studies of other deep fields. The radio loud and the sub-mJy populations possibly overlap with the agn- and s-Mb*N3*Rs, respectively. However, as the s-Mb*N3*Rs were subclassified to the starburst dominates (sb-Mb*N3*Rs) and the starburst/AGN co-existence (s/a-Mb*N3*Rs) in subsection 6.1, the sub-mJy radio populations can also be subclassified into starburst dominant and starburst/AGN co-existence populations. Thus, it will be interesting to compare the MIR populations with the X-ray and radio sources, which will be considered in a future paper.

7. Calorimetric Studies with MIR SEDs

For the s-Mb*N3*Rs and the sb-Mm*N3*Rs classified as dusty starbursts, their MIR SEDs with PAH emissions and Si absorption should contain rich information not only to distinguish from AGNs, but also about the physical properties in their star-forming regions, such as their bolometric luminosities, *SFR*s, and extinction, which were derived by calorimetric schemes in MIR SED analysis.

7.1. *Bolometric Luminosity and SFR*

As long as AGN activity is negligible in a galaxy, young stars are dominant sources for emission. Thus, the contributions of *SFR*s are nearly equal to the bolometric luminosity for star-forming galaxies. We can estimate the total emitting power with an SED analysis for multi-wavelength photometric data, and convert it to the *SFR*. *SFR*s are derived not only from the intrinsic UV continuum luminosity by assuming an extinction law for all z'-detected galaxies, but also from the IR luminosity for the s-Mb*N3*Rs and sb-Mm*N3*Rs.

When massive stars are not obscured by dust, *SFR* on a star-forming region can be directly traced with their UV continuum luminosity in the rest-frame wavelength of 1500 Å. Thus, the UV luminosity can be translated into the *SFR* by the relation

$$SFR_{\mathrm{UV}}\left(M_{\odot}\mathrm{yr}^{-1}\right) = \frac{L_{\nu}(1500\,\text{Å})}{8.85\times10^{27}(\mathrm{erg\ s^{-1}Hz^{-1}})}\,. \qquad (13)$$

When massive stars are born in dust-obscured star-forming regions, their UV radiation is reprocessed into IR emission. In this case, the *SFR* can be traced mainly with their TIR luminosity, L_{IR}. Even without using their TIR luminosity, as frequently applied, the intrinsic UV continuum luminosity, $L_{\mathrm{UV;cor}}$, can be reconstructed with a correction for the classical dust extinction, $A_{\mathrm{UV;opt}}$ from the observed UV luminosity, $L_{\mathrm{UV;obs}}$ (see also the details in subsection 7.3), and derive $SFR_{\mathrm{UV;cor}}$ from $L_{\mathrm{UV;cor}}$ with equation (13) and/or directly optical–NIR SED fittings with synthesis models. The scheme for $SFR_{\mathrm{UV;cor}}$ can be applied even for all z'-detected galaxies, including MIR faint galaxies.

For s-Mb*N3*Rs and sb-Mm*N3*Rs, on the other hand, by integrating a fitted model SED from 8 to 1000 μm in the rest-frame while correcting for the photometric redshift, $z_{\rm phot}$, we can obtain $L_{\rm IR}$ of the emission from the dusty star-forming regions. According to Kennicutt (1998), thus, *SFR* can be estimated from $L_{\rm IR}$ as

$$SFR_{\rm IR}\left(M_\odot {\rm yr}^{-1}\right) = \frac{L_{\rm IR}}{2.2\times10^{44}\,({\rm erg\ s}^{-1})}\ , \tag{14}$$

where we assumed the Salpeter IMF in the optical–NIR SED fitting, as shown in subsection 4.1. In general, the total *SFR* in a galaxy is derived as a sum,

$$SFR_{\rm IR+UV} = SFR_{\rm IR} + SFR_{\rm UV;obs}\ , \tag{15}$$

since dust can partially obscure galaxies. It is noted that $SFR_{\rm UV;obs}$ is derived from the observed UV luminosity, $L_{\rm UV;obs}$, without any extinction correction.

7.2. *Total IR Luminosities from MIR SED*

By means of the S&K model as a library of SED templates required in MIR SED fittings, we could derive the TIR luminosity from the fitted IR SEDs for the s-Mb*N3*Rs. Thus, we could obtain a relation between the rest-frame monochromatic 7.7 μm luminosity, $\nu L_{\nu,7.7}$, and the TIR luminosity, $L_{\rm IR}$, for all of the s-Mb*N3*Rs including both sb-Mb*N3*Rs and s/a-Mb*N3*Rs, as shown in figure 17. The top and bottom diagrams in figure 17 indicate the results in the $L_{\rm IR}$ estimation without and with subtraction of the obscured AGN contribution, respectively. Before subtraction of the AGN contribution, TIR luminosity range of the s/a-Mb*N3*Rs was larger than those of the sb-Mb*N3*Rs, as shown in the top diagrams of figure 17. After subtraction, the discrepancy in the TIR luminosities between the sb- and s/a-Mb*N3*Rs was reduced. This suggests that subtraction is effective to derive TIR luminosities, even for the s/a-Mb*N3*Rs, which is also essential to estimate their *SFR*s, as discussed in subsection 8.2.

Even though the TIR luminosity correlates well with the rest-frame 7.7-μm monochromatic luminosity, $\nu L_{\nu,7.7}$, as shown in figure 17, this estimation of the TIR luminosity with the MIR SED fitting seems to still be a kind of extrapolation to obtain the Far-InfraRed (FIR) emission at around $\simeq 1000\,\mu$m from the NIR/MIR side only up to $\simeq 24\,\mu$m with the best-fitted model SED. However, we would like to remark that it can be more than an extrapolation scheme, since the AKARI MIR multi-band photometry can certainly trace not only the PAH emission, but also the Si absorption feature, as already shown in figures 7 and 8. The absorption feature depends on the optical depth in galaxies, and corresponds to the TIR luminosity, as discussed in the following.

We can see multi-sequences in figure 17. The splitting into multi-sequences is mainly caused by the difference in the "mean" optical depth, which can be characterized as an SED model parameter of "visual extinction", $A_{V;\rm SK}$, at the edge of the dusty starburst nucleus in the S&K model, which is indicated by the symbol size. In MIR SED fittings with the S&K model library, we took the model SEDs with $A_{V;\rm SK} = 2.2$, 6.7, and 17.9, corresponding to large, medium, and small symbols in the figures, respectively. Even though $A_{V;\rm SK}$ is not equivalent to the observed visual extinction, A_V, assuming

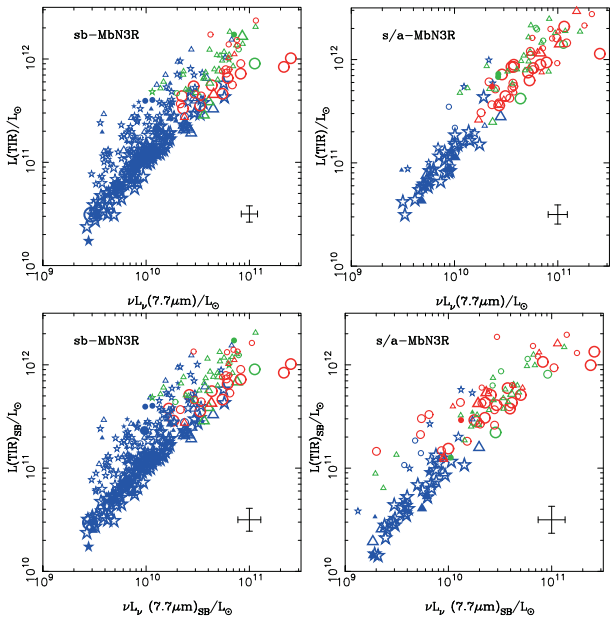

Fig. 17. Rest-frame 7.7-μm monochromatic luminosity $\nu L_{\nu,7.7}$ vs. the TIR luminosity, $L_{\rm IR}$, derived from IR SED fittings for the s-Mb*N3*Rs. The symbols are the same as in figure 6, except for their colors and sizes. Blue, green, and red symbols represent objects at redshifts of $0.4 \le z < 0.8$, $0.8 \le z < 1.2$, and $z \ge 1.2$, respectively. Large, medium, and small symbols indicate results that fit well with the S&K model SEDs of $A_{V;\rm SK} = 2.2$, 6.7, and 17.9, respectively. Top: $L_{\rm IR}$ derived without excluding the contribution from the hidden AGN. Bottom: $L_{\rm IR}$ derived while excluding the contribution from the hidden AGN. Left: For the sb-Mb*N3*Rs. Right: For the s/a-Mb*N3*Rs.

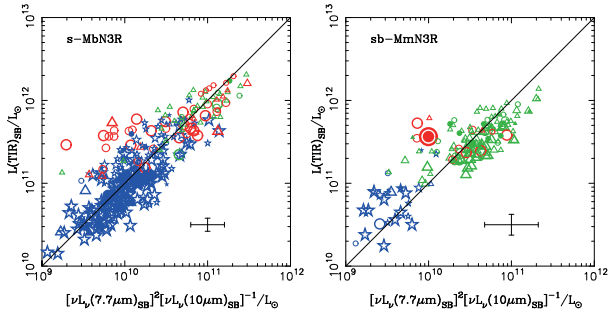

Fig. 18. Relation between the TIR luminosity, $L_{\rm IR}$, estimated from the S&K model and the rest-frame luminosities of $L_{\nu,7.7}$ and $L_{\nu,10}$. The symbols are the same as in figure 6, except for their colors and sizes. Blue, green, and red symbols represent objects at the redshifts of $0.4 \le z < 0.8$, $0.8 \le z < 1.2$, and $z \ge 1.2$, respectively. Large, medium, and small symbols indicate results that fit well with the S&K model SEDs of $A_{V;\rm SK} = 2.2$, 6.7, and 17.9, respectively. The line represents the relation approximated by equation (16).

spherical geometry for star-forming regions in the S&K model, this parameter, $A_{V;\rm SK}$, is quantitatively related to the optical depth of the observed dusty starbursts, since the model MIR SEDs with larger $A_{V;\rm SK}$ show a deeper Si 10 μm absorption feature, since it is induced with the dust self-absorption process in dense dusty regions. In fact, the s-Mb*N3*Rs, with not only PAH emissions, but also Si 10 μm absorption, have various ratios of $\nu L_{\nu,10}/\nu L_{\nu,7.7}$ between 10 and 7.7 μm, as already

shown in figure 8. Then, the observed ratio, $\nu L_{\nu,10}/\nu L_{\nu,7.7}$, contains information about the mean optical depth related to the denseness and the size of a dusty star-forming region, which is parametrized with $A_{V;\mathrm{SK}}$ in the S&K model (see the details in appendix 5.4).

Thus, the MIR SED fitting with the S&K model can analyze a variational degree of the mean optical depth possibly related to the Si absorption depth. The mean optical depth is another influential parameter for estimating the TIR luminosity from the MIR SED fitting. Thus, it is expected that their TIR luminosity is correlated not only with the rest-frame monochromatic 7.7 μm PAH luminosity, $\nu L_{\nu,7.7}$, but also with the Si absorption depth, at least for the selected starburst samples of the s-Mb*N3*Rs and the sb-Mm*N3*Rs as

$$L_{\mathrm{IR;SK}} \simeq 10 \times \left(\frac{\nu L_{\nu,10}}{\nu L_{\nu,7.7}}\right)^{\alpha} \times \nu L_{\nu,7.7} \,, \tag{16}$$

where the units of $L_{\mathrm{IR}}, \nu L_{\nu,7.7}$, and $\nu L_{\nu,10}$ are (erg s^{-1}) and $\alpha \simeq -1$. This approximate formulation can work well, as shown in figure 18.

Even though the S&K model can reproduce MIR SEDs of the s-Mb*N3*Rs and the sb-Mm*N3*Rs well, they are produced with some simplified assumptions, such as a spherical geometry with constant dust distribution for the modeled starburst region. Even though we could confirm the accuracy of the estimation for the TIR luminosity with complementary observations at longer wavelengths than MIR as FIR and Submm, as remarked in section 11, we have not yet obtained them in the field. At this moment, we can not rule out a possibility that the TIR luminosity, $L_{\mathrm{IR;SK}}$, estimated with the fitted S&K model, includes a systematic offset. Thus, we introduce a factor, f_{SK}, in the conversion from the model estimated $L_{\mathrm{IR;SK}}$ to the real L_{IR}:

$$L_{\mathrm{IR}} = f_{\mathrm{SK}} L_{\mathrm{IR;SK}} \,. \tag{17}$$

As long as the proportional factor $f_{\mathrm{SK}} = 0.3$–1, the estimation of L_{IR} is consistent with previous work. For example, by taking $f_{\mathrm{SK}} \simeq 1$, we can roughly reproduce the a relation $L_{\mathrm{IR}} \simeq 17.2\, L_{5\text{–}8.5\ \mu\mathrm{m}}$ by Elbaz et al. (2002). We found an offset between the S&K model and the Chary and Elbaz (2001) model (C&E model), in which the TIR luminosity with the C&E model can be reproduced with $f_{\mathrm{SK}} \simeq 0.3$ (see figure 64 in appendix 5). In the following, we take $f_{\mathrm{SK}} = 1$ as the default value.

7.3. *Classical and Calorimetric Extinctions*

In this subsection, we derive extinctions at the UV wavelength $\simeq 1500$ Å with two schemes, and compare them. One scheme is with optical–NIR SED analysis, deriving classical UV extinction $A_{\mathrm{UV;opt}}$ related to common visual extinction A_V. Another is with the IR SED analysis, deriving calorimetric extinction $A_{\mathrm{UV;IR}}$ as a ratio of total emission to observed UV emission.

For all BBGs/IRBGs including the MfBBGs, even without MIR detections, visual extinction A_V can be derived from the multicolor optical–NIR SED fitting with stellar population synthesis models as the BC03 model. In a dust-screen model, the dust extinction magnitude, A_λ, is proportional to the optical depth at a wavelength λ to characterize the difference between

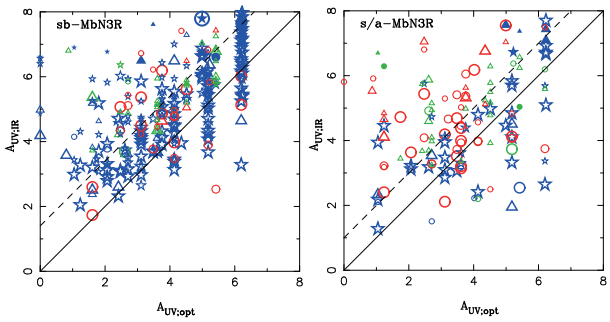

Fig. 19. Correlation between two extinctions at 1500 Å derived from the optical–NIR SED fitting and the luminosity ratio of the total to observed UV as $A_{\mathrm{UV;opt}}$ vs. the $SFR_{\mathrm{IR+UV}}/SFR_{\mathrm{UV;obs}}$. The symbols are the same as in figure 18. The dashed line represents a proportional law with equation (21), obtained by fitting the sample. Left: For the sb-Mb*N3*Rs. Right: For the s/a-Mb*N3*Rs.

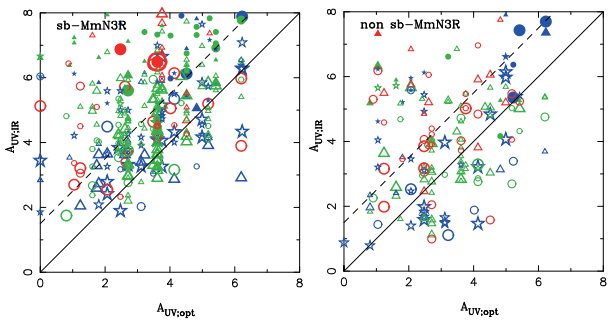

Fig. 20. Same as figure 19 for the Mm*N3*Rs. The dashed line represents a proportional law with equation (21), obtained by fitting the sample. Left: For the sb-Mm*N3*Rs. Right: For the non sb-Mm*N3*Rs.

the intrinsic flux, $F_{\mathrm{int}}(\lambda)$, and the observed flux, $F_{\mathrm{obs}}(\lambda)$, as

$$F_{\mathrm{obs}}(\lambda) = F_{\mathrm{int}}(\lambda) 10^{-0.4 A_\lambda} \,. \tag{18}$$

By selecting a reddening curve of $k(\lambda)$ from extinction models: the Milky Way, the LMC, the SMC, and the Calzetti law, extinction A_λ at a wavelength λ can be represented with the visual extinction, A_V, or the color excess, $E(B-V)$, as

$$A_\lambda = \frac{k(\lambda)}{R_V} \times A_V = k(\lambda) E(B-V) \,, \tag{19}$$

where $R_V = 3.1$, 2.72, and 4.05 is for both the Milky Way and the LMC, for the SMC, and for the Calzetti law, respectively, and the reddening curves are normalized as $k(B) - k(V) = 1$. In the following, we have taken the best-fitted reddening curve in the optical–NIR SED fittings for each galaxy to convert the obtained $A_{V;\mathrm{opt}}$ to $A_{\mathrm{UV;opt}} = A_{1500}$ at $\lambda = 1500$ Å as a typical "optically observed" UV extinction.

Even though the above estimation of $A_{V;\mathrm{opt}}$ has been frequently applied in studying the extinction of distant galaxies, it should be recalled that it is based on a simple dust-screen model, which cannot guarantee a correct description of the radiation fields in nuclear starbursts expected in s-Mb*N3*Rs and sb-Mm*N3*Rs. Thus, we also tried to estimate the calorimetric extinction, $A_{\mathrm{UV;IR}}$, for the s-Mb*N3*Rs and sb-Mm*N3*Rs. If the dust and stellar components are mixed

Table 4. Fitting results with equation (21).*

	a_A	$\Delta A_{\rm UV}$	Residuals (RMS)
sb-Mb*N3*R	0.52 ± 0.05	3.3 ± 0.2	1.51
	fixed 1	1.4 ± 0.1	1.69
s/a-Mb*N3*R	0.41 ± 0.08	3.2 ± 0.3	1.47
	fixed 1	1.0 ± 0.1	1.74
sb-Mm*N3*R	0.22 ± 0.09	4.6 ± 0.3	2.34
	fixed 1	2.0 ± 0.1	2.57
non sb-Mm*N3*R	0.29 ± 0.12	3.7 ± 0.4	2.46
	fixed 1	1.5 ± 0.1	2.68

* Values are means and ± standard deviations.

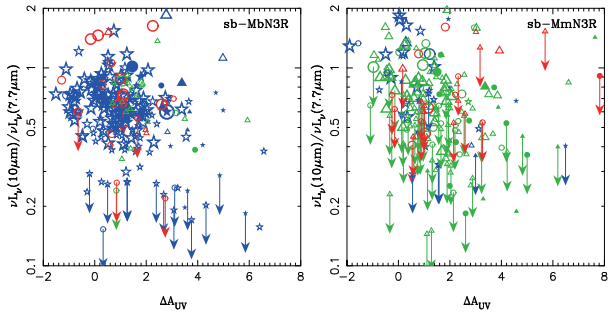

Fig. 21. Extinction difference $\Delta A_{\rm UV}$ vs. the monochromatic luminosity ratio of $\nu L_{\nu,10}/\nu L_{\nu,7.7}$, where $\Delta A_{\rm UV} = A_{\rm UV;IR} - A_{\rm UV;opt}$ is derived from the calorimetric estimated extinction $A_{\rm UV;IR} = 2.5 \log (SFR_{\rm IR+UV}/SFR_{\rm UV;obs})$ and the classical extinction $A_{\rm UV;opt}$. The symbols are the same as in figure 18.

well in a galaxy as nuclear starbursts in local LIRGs/ULIRGs, extinction estimations with the IR SED analysis may be more accurate than the common scheme for the classical extinction, $A_{\rm UV;opt}$, from the visual extinction, A_V. The total bolometric luminosity, $L_{\rm IR+UV}$, from the star-forming regions in s-Mb*N3*Rs and sb-Mm*N3*Rs can be estimated as $L_{\rm IR+UV} = L_{\rm IR} + L_{\rm UV;obs}$, which is the sum of the TIR luminosity, $L_{\rm IR}$, derived from MIR photometric SED analysis in section 7 and the observed UV luminosity, $L_{\rm UV;obs}$, not corrected for dust extinction derived from the optical–NIR photometric SED fitting. Using $L_{\rm IR+UV}$ and $L_{\rm UV;obs}$, we can derive an alternative extinction with a calorimetric scheme as

$$A_{\rm UV;IR} = 2.5 \log \left(\frac{L_{\rm IR+UV}}{L_{\rm UV;obs}} \right) , \quad (20)$$

where we have taken the *SFR* ratio as the luminosity ratio, $(L_{\rm IR+UV}/L_{\rm UV;obs}) \simeq (SFR_{\rm IR+UV}/SFR_{\rm UV;obs})$. Figures 19 and 20 show comparisons between the calorimetric extinction, $A_{\rm UV;IR}$, and the classical extinction, $A_{\rm UV;opt} = A_{1500}$, for the s-Mb*N3*Rs and the sb-Mm*N3*Rs, respectively, where we have taken $f_{\rm SK} = 1$ in the estimation of $L_{\rm IR}$. We can see that the calorimetric extinction, $A_{\rm UV;IR}$, with the IR SED analysis shows a proportional trend for the classical extinction, $A_{\rm UV;opt}$, which suggests both extinctions are different, yet almost the same.

However, there are some offsets between $A_{\rm UV;IR}$ and $A_{\rm UV;opt}$, as shown in figures 19 and 20. We fitted the trend with the form

$$A_{\rm UV;IR} = a_A A_{\rm UV;opt} + \Delta A_{\rm UV} . \quad (21)$$

As the fitting results summarized in table 4 show, mean offsets of sb-Mb*N3*Rs, s/a-Mb*N3*Rs, and sb-Mm*N3*Rs are significant compared with the RMS of the residuals, while those of non sb-Mm*N3*Rs are not. This result suggests that the offsets of sb-Mb*N3*Rs, s/a-Mb*N3*Rs, and sb-Mm*N3*Rs may be systematic ones. By fixing $a_A = 1$ as a proportionality between $A_{\rm UV;IR}$ and $A_{\rm UV;opt}$, assumed for sb-Mb*N3*Rs, s/a-Mb*N3*Rs, and sb-Mm*N3*Rs, the systematic offsets are $\langle \Delta A_{\rm UV} \rangle = 1.4$, 1.0, and 2.0, respectively, which are represented by dashed lines, as shown in figures 19 and 20. There are two ways to understand the systematic offset: (1) $A_{\rm UV;IR}$ with the S&K model tends to overestimate, or (2) $A_{\rm UV;opt}$ with the classical extinction laws tends to underestimate. At least for s-Mb*N3*Rs, the former recommends to take $f_{\rm SK} \simeq 0.3$, while the latter suggests $f_{\rm SK} \simeq 1$. On-going or near-future observations in Submm and FIR wavelengths can determine the parameter $f_{\rm SK}$ as discussed in section 11.

The MIR SED fitting with the S&K model derives not only $A_{\rm UV;IR}$ from $L_{\rm IR;SK}$, but also the visual extinction, $A_{V;\rm SK}$, in the model parameters. In figures 19 and 20, the smaller and larger symbols represent galaxies fitted with larger and smaller $A_{V;\rm SK}$, respectively. We can see another trend, that sb-Mb*N3*Rs with larger $A_{V;\rm SK}$ have larger offsets in extinction, $\Delta A_{\rm UV}$, due to the variation of $A_{\rm UV;IR}$, even in the same $A_{\rm UV;opt}$ sample. This variation of $A_{\rm UV;IR}$ can be caused by that of the interstellar density, which also determines a parameter, $A_{V;\rm SK}$ in the S&K model. As discussed in subsection 7.2, $A_{V;\rm SK}$ characterizes the monochromatic luminosity ratio between the rest-frame 10 and 7.7 μm: $\nu L_{\nu,10}/\nu L_{\nu,7.7}$, as the effect on mean optical depth in $L_{\rm IR}/\nu L_{\nu,7.7}$ represented in equation (16) (see also figures 17 and 18). Then, it is expected that we can see some correlations between $\Delta A_{\rm UV}$ and $\nu L_{\nu,10}/\nu L_{\nu,7.7}$. In figure 21, indeed, we can see that sb-Mb*N3*Rs with larger $A_{V;\rm SK}$ have not only larger $\Delta A_{\rm UV;IR}$, but also deeper 10-μm decrement, which may be caused by Si self-absorption as remarked in subsection 6.1.

These trends can be naturally explained by different characteristics of the extinctions of $A_{\rm UV;opt}$, and $A_{\rm UV;IR}$, as follows. The calorimetric extinction, $A_{\rm UV;IR}$, may trace the dust extinction in dense dust-obscured areas in star-forming regions, since the dust column density becomes large enough to cause Si self-absorption. In contrast, the classical extinction, $A_{\rm UV;opt}$, tends to trace relatively lower optical depth areas, such as optical emissions, which are mainly detected from the lower optical depth areas. Thus, the extinction difference, $\Delta A_{\rm UV}$, may be related to the geometrical variations in their star-forming regions and dust distributions in the s-Mb*N3*Rs and sb-Mm*N3*Rs.

8. Evolution of SFRs and Extinctions

As examined in section 7, we could derive the TIR luminosity and the extinction for s-Mb*N3*Rs and sb-Mm*N3*Rs at $z = 0.4$–2, which can be applied to estimate the *SFR*. In this section, we reconstruct their evolutionary features and mass dependence of extinction and *SFR* in galaxies up to $z = 2$.

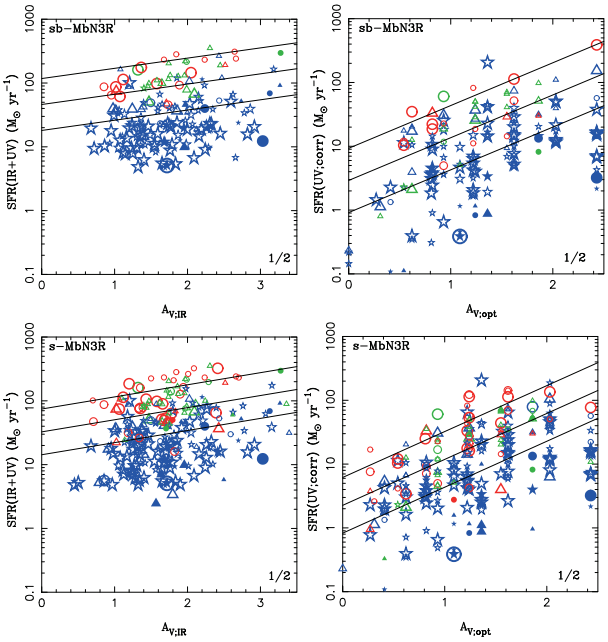

Fig. 22. Relation between the visual extinction, A_V, and *SFR* for the s-Mb*N3*Rs and the sb-Mb*N3*Rs. The symbols are the same as in figure 18. Solid lines represent the fitted results with equation (22) for $M_* = 10^{11}\,M_\odot$ at $z = 1.5$, 1.0, and 0.6 from top to bottom. Top-left: For $A_{V;\mathrm{IR}}$ and $SFR_{\mathrm{IR+UV}}$ of sb-Mb*N3*Rs. Top-right: For $A_{V;\mathrm{opt}}$ and $SFR_{\mathrm{UV;cor}}$ of sb-Mb*N3*Rs. Bottom-left: Same as the top-left for s-Mb*N3*Rs. Bottom-right: Same as the top-right for s-Mb*N3*Rs.

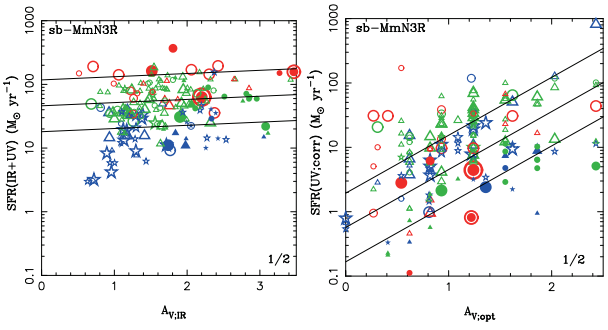

Fig. 23. Same as figure 22 for sb-Mm*N3*Rs. Left: For $A_{V;\mathrm{IR}}$ and $SFR_{\mathrm{IR+UV}}$. Right: For $A_{V;\mathrm{opt}}$ and $SFR_{\mathrm{UV;cor}}$.

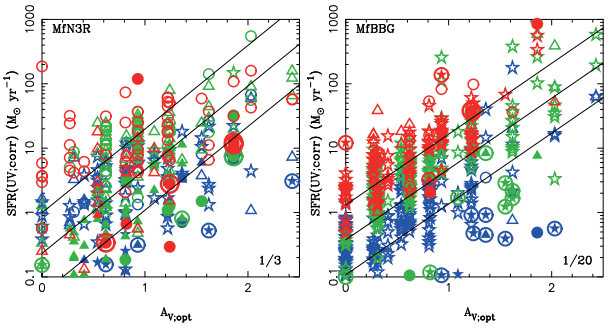

Fig. 24. Relation between the visual extinction, A_V, and $SFR_{\mathrm{UV;cor}}$ for the Mf*N3*Rs and the MfBBGs. Solid lines represent the fitted results with equation (22) for $M_* = 10^{10}\,M_\odot$ at $z = 1.5$, 1.0, and 0.6 from top to bottom. Left: For the Mf*N3*Rs. Right: For the MfBBGs.

Table 5. Fitting results with equation (22).*

	$\log\left(\frac{SFR_0}{M_\odot\,\mathrm{yr}^{-1}}\right)$	α	β	γ
$A_{V;\mathrm{IR}}$				
sb-Mb*N3*R	0.4	0.16	4.2	0.17
	±0.1	±0.02	±0.2	±0.04
s-Mb*N3*R	0.4	0.19	3.7	0.13
	±0.1	±0.02	±0.2	±0.04
sb-Mm*N3*R	0.4	0.05	4.2	0.16
	±0.1	±0.02	±0.2	±0.03
$A_{V;\mathrm{opt}}$				
sb-Mb*N3*R	−1.1	0.67	5.2	−0.19
	±0.2	±0.05	±0.5	±0.08
s-Mb*N3*R	−1.0	0.72	4.5	−0.21
	±0.1	±0.04	±0.4	±0.06
sb-Mm*N3*R	−1.9	0.9	5.5	−0.42
	±0.3	±0.1	±0.8	±0.11
Mf*N3*Rs	−3.3	1.3	6.5	−0.71
	±0.2	±0.1	±0.4	±0.06
MfBBGs	−2.3	1.1	5.6	−0.19
	±0.2	±0.1	±0.1	±0.06

* Values are means ± standard deviations.

8.1. *Correlation among SFR, Extinction, Redshift, and Mass*

Figures 22, 23, and 24 show the correlation between A_V and *SFR* for s-Mb*N3*Rs, sb-Mm*N3*Rs, Mf*N3*Rs, and MfBBGs. For all subsamples, we fitted correlations among A_V, *SFR*, z, and M_* with the form

$$\frac{SFR}{SFR_0} = 10^{\alpha A_V}(1+z)^{\beta}\left(\frac{M_*}{10^{11}M_\odot}\right)^{\gamma}, \qquad (22)$$

where SFR_0 is a normalization parameter for the *SFR* in units of $M_\odot\,\mathrm{yr}^{-1}$. Their best-fitting planes are determined in the space of A_V, $\log(1+z)$, $\log M_*$, and $\log SFR$, as summarized in table 5 and shown in figures 22, 23, and 24. For the s-Mb*N3*Rs, we can estimate both the classical visual extinction, A_V, with the SED fitting and the calorimetric visual extinction, $A_{V;\mathrm{IR}}$, converted from the calorimetric UV extinction, $A_{\mathrm{UV;IR}}$, with equation (19) for the best-fitted reddening curve in the optical–NIR SED fitting.

We should remember that $SFR_{\mathrm{IR+UV}}$ and $A_{V;\mathrm{IR}}$ are estimated from their MIR SED fittings, while $SFR_{\mathrm{UV;cor}}$ and $A_{V;\mathrm{opt}}$ are from their optical SED fittings. This denotes that the trends of $SFR_{\mathrm{IR+UV}}$ and $A_{V;\mathrm{IR}}$ are independent of those of $SFR_{\mathrm{UV;cor}}$ and $A_{V;\mathrm{opt}}$. As shown in figure 22, however, the correlation between $SFR_{\mathrm{IR+UV}}$ and $A_{V;\mathrm{IR}}$ is similar to that between $SFR_{\mathrm{UV;cor}}$ and $A_{V;\mathrm{opt}}$. Furthermore, the trends, among $SFR_{\mathrm{UV;cor}}$, $A_{V;\mathrm{opt}}$, and z_{phot}, except M_*, are similar to each other not only in the Mb*N3*Rs and the Mm*N3*Rs, but also in all subsamples including the Mf*N3*Rs and MfBBGs, as shown in figure 22 (see also table 5). All of them show the same trends: (1) larger *SFR*, larger extinction, A_V, and (2) a lower redshift, larger extinction, A_V. The second trend, increasing A_V with the cosmic time, suggests that increasing dust has been

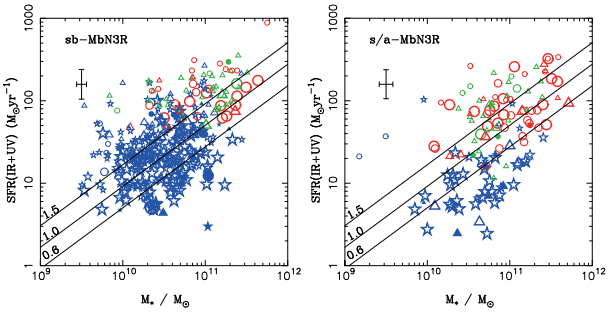

Fig. 25. Stellar mass M_* vs. $SFR_{\rm IR+UV}$ derived with the TIR and observed UV luminosities. The lines are the same as in figure 27 (see the text in detail). The symbols are the same as in figure 18. Left: For the sb-Mb*N3*Rs. Right: Same as on the left for the star-forming components in the s/a-Mb*N3*Rs.

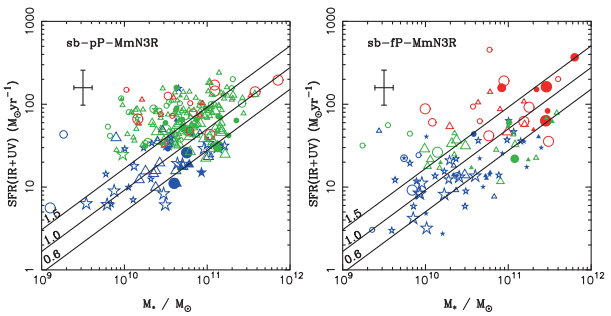

Fig. 26. Same as figure 25 for the sb-Mm*N3*Rs. Left: For the sb-pP-Mm*N3*Rs. Right: For the sb-fP-Mm*N3*Rs.

induced with chemical enrichment in evolving galaxies.

8.2. *Mass Dependence and Evolution of SFR*

Figures 25 and 26 show $SFR_{\rm IR+UV}$ to M_* for the sb- and s/a-Mb*N3*Rs and sb-Mm*N3*Rs. We can see correlations between $SFR_{\rm IR+UV}$ and M_*, which are more obvious for the sb-Mb*N3*Rs than for the s/a-Mb*N3*Rs. The correlation between $SFR_{\rm IR+UV}$ and M_* in the sb-Mb*N3*Rs also has an evolutionary trend. The $SFR_{\rm IR+UV}$–M_* correlation in the s/a-Mb*N3*Rs is more scattered to the lower *SFR* side from that in the sb-Mb*N3*Rs, in which the decrement becomes more obvious at lower redshifts $z < 0.8$, even though the highest mass group around $10^{11}\,M_\odot$ at higher redshifts $z \geq 0.8$ tends to mostly follow that in the sb-Mb*N3*Rs. They indicate that the star-formation activities in the s/a-Mb*N3*Rs were quenched at $z < 0.8$ compared with those in the sb-Mb*N3*Rs. The indicated connection between quenching star formation and AGN activity around $z \simeq 0.8$ is discussed along with the evolution of the stellar populations in section 9.

The evolutionary trend and mass dependence on the *SFR* can be seen more clearly in figure 27, for all of the star-forming galaxies including the s-Mb*N3*Rs, the sb-Mm*N3*Rs, the star-forming Mf*N3*Rs, and the MfBBGs, which are plotted from top to bottom in redshift intervals of $0.4 \leq z < 0.8$, $0.8 \leq z < 1.2$, and $z \geq 1.2$. The star-forming Mf*N3*Rs and MfBBGs are selected as the population in the region of the "blue cloud" in the $(U - V) - \Delta_{\rm UV}$ color, as remarked in

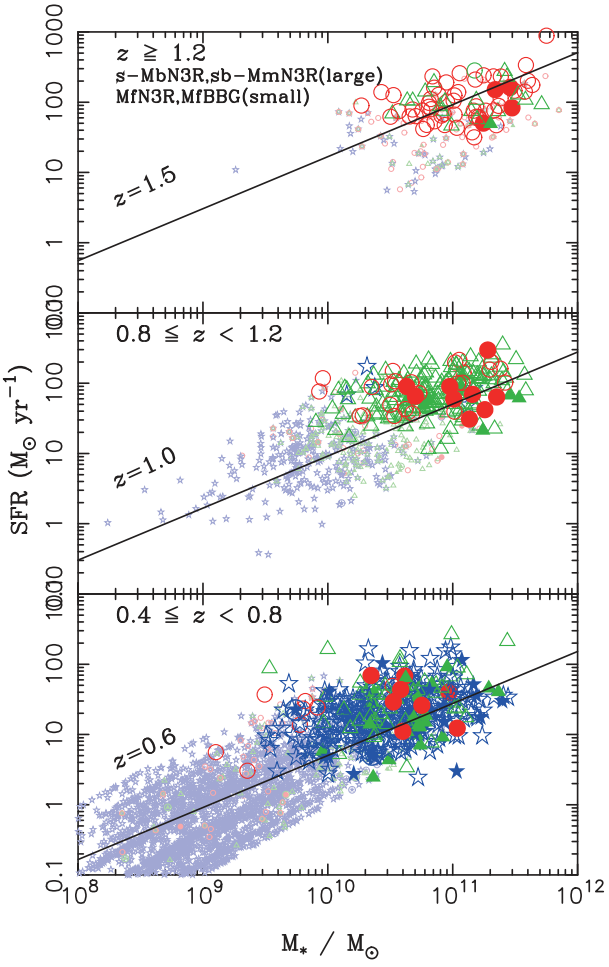

Fig. 27. Stellar mass M_* vs. *SFR* for all the star-forming galaxies; the sb-Mm*N3*Rs, Mf*N3*Rs, and MfBBGs. The lines represent the fitting result (see the text in detail). The symbols are the same as in figure 6, except for the large dark and small thin ones represent the MIR-detected star-forming *N3*Rs (s-Mb*N3*Rs and sb-Mm*N3*Rs) and the MIR faint star-forming galaxies (star-forming Mf*N3*Rs and MfBBGs), respectively. Top: For $z \geqq 1.2$. Middle: For $0.8 \leq z < 1.2$. Bottom: For $0.4 \leq z < 0.8$.

subsection 6.4, which excludes extremely young objects fitted with the BC03 model of age $t < 0.1$ Gyr.

The mean *SFR* for all of the star-forming galaxies including both the s-Mb*N3*Rs, sb-Mm*N3*Rs, Mf*N3*Rs, and MfBBGs is presented as an approximate function of M_* and z,

$$SFR\left(M_\odot \mathrm{yr}^{-1}\right) \simeq SFR_{11}\left(\frac{M_*}{10^{11} M_\odot}\right)^{\alpha} (1+z)^{\beta}\,, \qquad (23)$$

where the best-fitting plane in the space of $\log M_*$, $\log(1+z)$, and $\log SFR$ is determined as $SFR_{11}/(M_\odot\,\mathrm{yr}^{-1}) = 7.8$, $\alpha = 0.74 \pm 0.01$, and $\beta = 2.7 \pm 0.1$. In figures 25, 26, and 27, the solid lines at $z = 0.65$, 1.0, and 1.5 represent the best-fitting result. Roughly taking $\alpha \simeq 1$ and $\beta \simeq 3$ for simplification, the growth time scale of the star-forming galaxies is typically derived as

$$\frac{M_*}{SFR}\ (\mathrm{yr}) \simeq 10^{10}(1+z)^{-3}\,, \qquad (24)$$

which means the inverse of the *sSFR*. These *SFR* evolutionary

properties and mass dependence are consistent with previous work for star-forming galaxies selected with general schemes (Noeske et al. 2007; Santini et al. 2009; Dunne et al. 2009; Pannella et al. 2009).

9. Evolution of Stellar Populations

9.1. Rest-Frame Optical Color Distributions

The CMD is a powerful tool for studying galaxy evolution, since it shows the bimodal galaxy distribution as early types that concentrate in a tight red sequence, while late types distribute in a blue dispersed cloud, which have been studied not only in the local universe with the SDSS (Blanton et al. 2003), but also in the distant universe with surveys for $z < 1$ (Bell et al. 2004; Faber et al. 2007; Borch et al. 2006) and for $z > 1$ (Pannella et al. 2009; Brammer et al. 2009). Spitzer results have also shown that rest-frame colors of MIPS-detected objects, which may overlap with the Mb*N3*Rs and the Mm*N3*Rs, fall between the red sequence and the blue cloud up to $z = 2$ (Cowie & Barger 2008; Salim et al. 2009; Brammer et al. 2009).

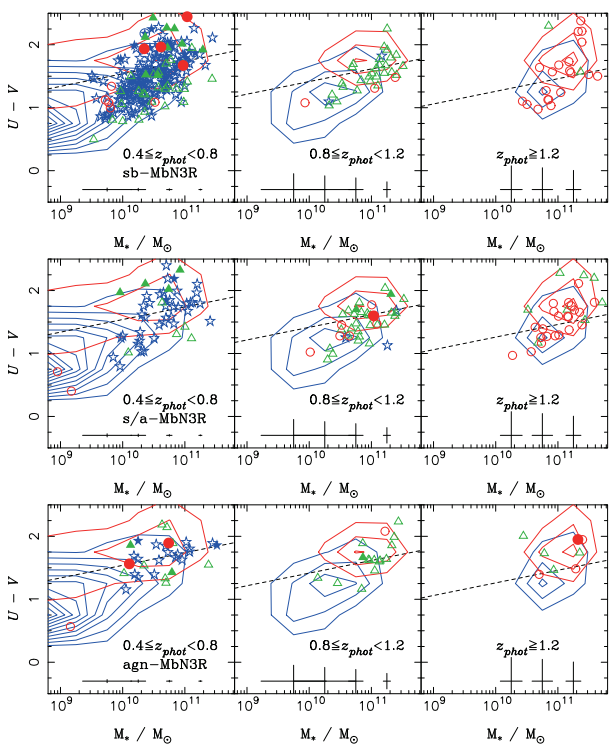

Fig. 28. Stellar mass and rest-frame color diagram of M_* vs. $U - V$ for the Mb*N3*Rs excluded BL AGNs and EBOs. The color is not corrected for dust extinction. Typical errors of the mass and color are represented with crosses at the bottom. Open and filled symbols and filled symbols in circles represent s-, p-, and qp-BBGs, respectively, which are the same as in figure 6. The plots are for $0.4 \leq z < 0.8$, $0.8 \leq z < 1.2$, and $z \geqq 1.2$ from left to right. Red and blue contours represent the rest-frame V detected galaxies with $sSFR < 0.1\,\mathrm{Gyr}^{-1}$ and $sSFR > 0.1\,\mathrm{Gyr}^{-1}$, respectively. The dashed line corresponds to the Bell's critical line dividing the photometric samples into the blue cloud and the red sequence. Top: Colored symbols represent the sb-Mb*N3*Rs. Middle: Same as the top for the s/a-Mb*N3*Rs. Bottom: Same as the top for the agn-Mb*N3*Rs.

Thus, we also studied the rest-frame $U - V$ colors for Mb*N3*Rs and Mm*N3*Rs in the field from their magnitudes interpolated with equation (4). Figure 28 shows the $U - V$ color without any extinction correction for the stellar mass M_* for the sb-, s/a-, and agn-Mb*N3*Rs from top to bottom, where the left, middle, and right figures correspond to redshift intervals of $0.4 \leq z < 0.8$, $0.8 \leq z < 1.2$, and $z \geq 1.2$, respectively; the overplotted contours represent the rest-frame V detected galaxies, which are also shown with the Mf*N3*Rs in figure 29.

The well-known "red and dead" population in a red sequence has a typical color of $U - V \simeq 2$, which can be the reddest ones, even in the local universe with low A_V values. However, redder populations of $U - V > 2$ can be clearly seen in all diagrams, not only for the Mb*N3*Rs, but also for the Mm*N3*Rs, and even for the Mf*N3*Rs, as shown in figures 28, 29, and 30.

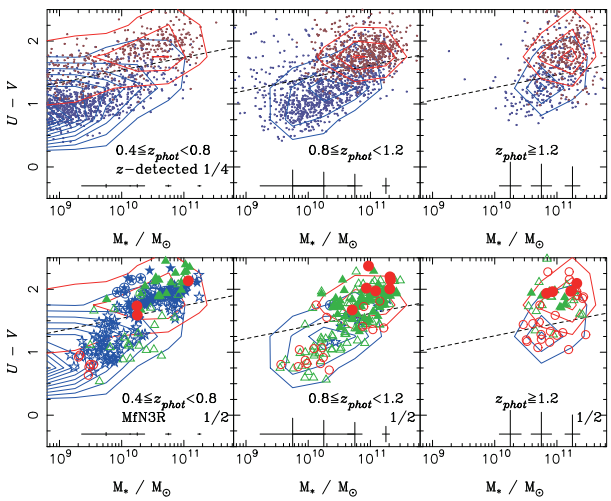

Fig. 29. Same as figure 28 for the the rest-frame V detected galaxies and the Mf*N3*Rs. The red and blue small dots with contours represent the rest-frame V detected galaxies with $sSFR < 0.1\,\mathrm{Gyr}^{-1}$ and $sSFR > 0.1\,\mathrm{Gyr}^{-1}$, respectively. Top: For the rest-frame V detected galaxies. Bottom: For the Mf*N3*Rs.

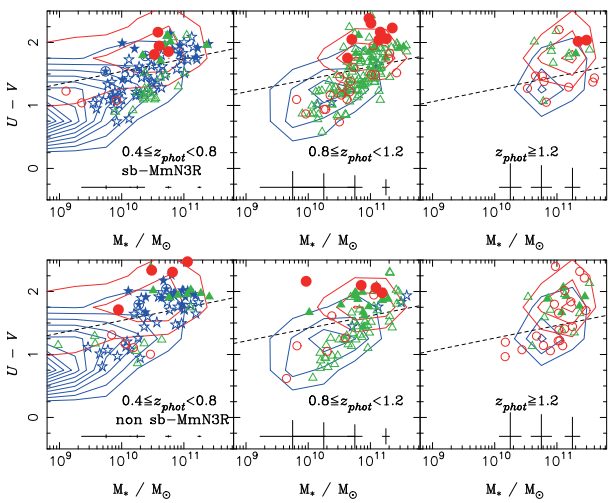

Fig. 30. Same as figure 28 for the Mm*N3*Rs. Top: Colored symbols represent the sb-Mm*N3*Rs. Bottom: Same as the top for the non sb-Mm*N3*Rs.

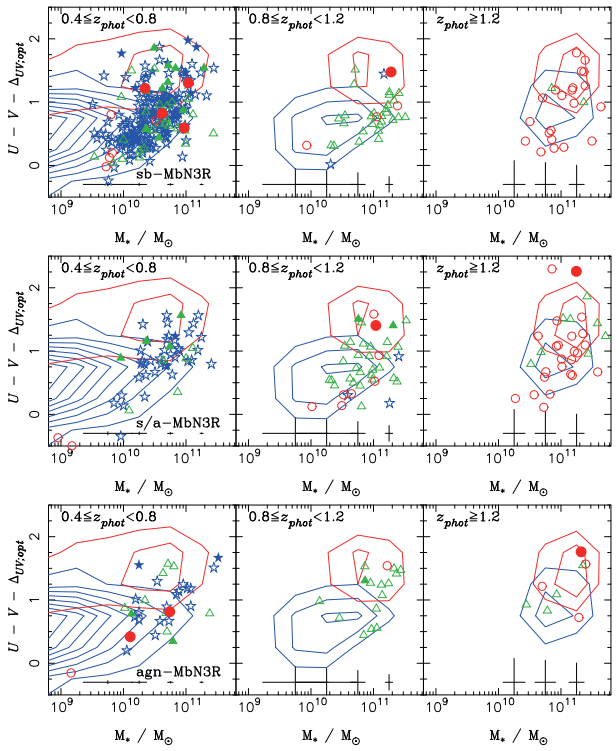

Fig. 31. Same as figure 28 for color $U - V - \Delta_{\rm UV}$ corrected using the extinction $A_{\rm UV;opt}$, which is derived from the optical–NIR SED fitting. The sb-, s/a-, and agn-Mb*N3*Rs are plotted from top to bottom.

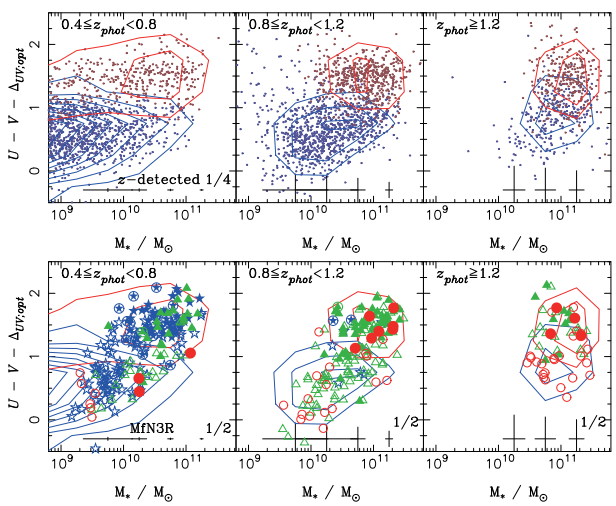

Fig. 32. Same as figure 29 for color $U - V - \Delta_{\rm UV}$ corrected using the extinction $A_{\rm UV;opt}$.

This suggests that not only the Mb*N3*Rs, but also the Mm*N3*Rs and most of the Mf*N3*Rs, suffer from dust extinction, which is already expected from the results in section 8. Thus, we have taken into account color corrections for these diagrams. Figures 31, 32, and 33 represent intrinsic stellar color $(U - V) - \Delta_{\rm UV}$ corrected for extinction using $A_{\rm UV;opt}$, derived from the optical–NIR SED fitting. In the top diagrams of figure 31, we can see that the bimodal color distribution of the Mb*N3*Rs persists even up to $z \simeq 1.2$, which is also consistent with the

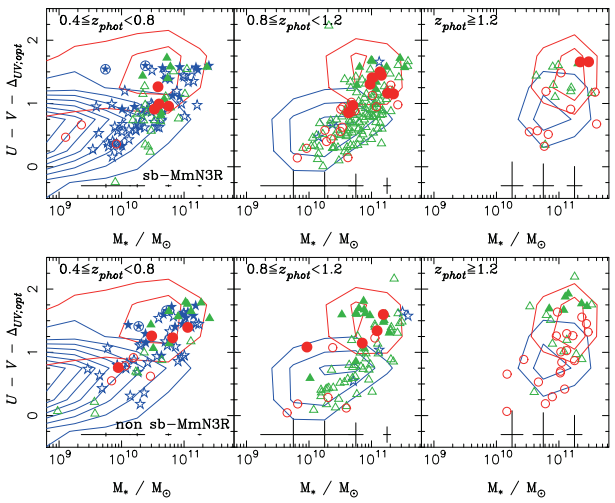

Fig. 33. Same as figure 30 for color $U - V - \Delta_{\rm UV}$ corrected using the extinction $A_{\rm UV;opt}$.

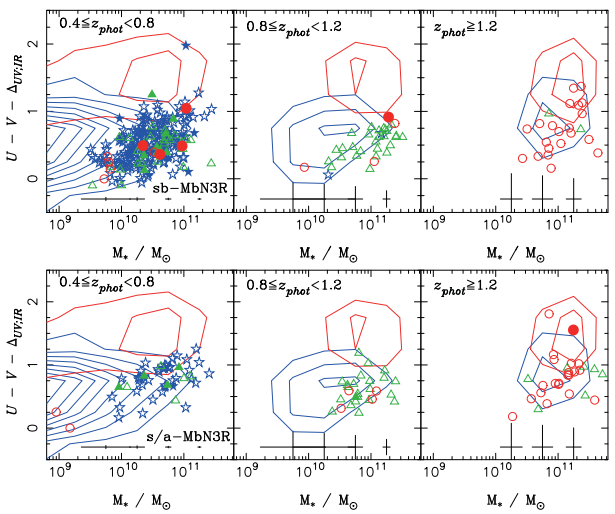

Fig. 34. Same as figure 31 for color $U - V - \Delta_{\rm UV}$ corrected using the extinction $A_{\rm UV;IR}$, which is derived with equation (20). Top: For the sb-Mb*N3*Rs. Bottom: For the s/a-Mb*N3*Rs, its remaining dusty starburst component can be extracted and then used to derive $SFR_{\rm IR+UV}$ by fitting its MIR SED with the S&K model.

BBG classification, since p-BBGs mainly appear in the region of a red sequence. As discussed in appendix 1.3, unfortunately, our $K_{\rm s}$ photometry is not deep enough to obtain a complete sample up to $z \geq 1.2$, which may be one of the reasons why the bimodal feature at $z \geq 1.2$ is not so clear compared with the results of Brammer et al. (2009).

Figure 34 also shows the intrinsic colors of stellar components in the sb- and s/a-Mb*N3*Rs, in which the colors were corrected with $A_{\rm UV;IR}$. A few of them remain in the red sequence region, which comes from the effect of extinctions, as discussed in subsection 7.3: $\langle A_{\rm UV;IR}\rangle \simeq \langle A_{\rm UV;opt}\rangle + \langle \Delta A_{\rm UV}\rangle$ with $\langle \Delta A_{\rm UV}\rangle \sim 0.5$ as long as $f_{\rm SK} = 1$. Furthermore, we cannot clearly see the bimodality in figure 34 compared with figure 31. The same trends can be also confirmed for the Mm*N3*Rs, as shown in figure 35. Even

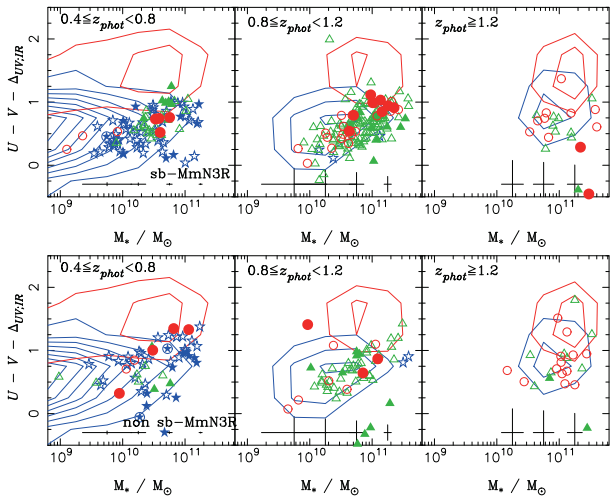

Fig. 35. Same as figure 34 for the Mm*N3*Rs. Top: For the sb-Mm*N3*Rs. Bottom: For the non sb-Mm*N3*Rs.

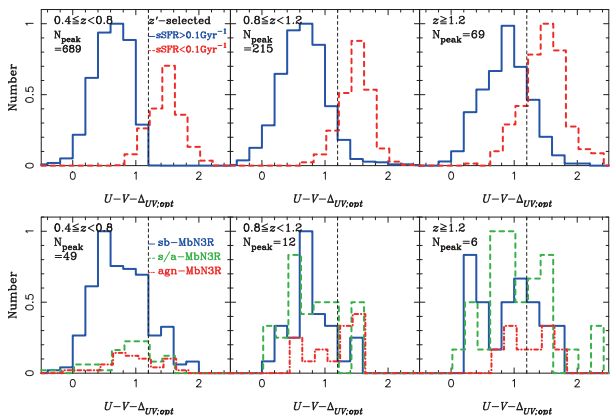

Fig. 36. Histograms of the corrected color distribution with A_V derived from optical SED fittings. The height of the histograms is normalized with the maximum number, which is displayed on the upper-left side. Top: For the rest-frame V detected galaxies, which are classified into two groups with *sSFR* larger and less than 0.1 Gyr^{-1}, which corresponds to a color $U - V - \Delta_{\rm UV} = 1.2$. Bottom: For the sb-, s/a-, and agn-Mb*N3*Rs.

if we have $\langle \Delta A_{\rm UV} \rangle \sim 0$ by taking the proportional factor as $f_{\rm SK} \simeq 0.3$, we just obtain a bluer mean color by adding $\simeq 0.5$ without recovering the bimodality. This suggests that it is appropriate to correct the color of a whole galaxy in the classical way with $A_{\rm UV;opt}$, even for such dusty systems as the Mb*N3*Rs and the Mm*N3*Rs. Thus, we discuss the evolution of stellar populations along with the results corrected with $A_{\rm UV;opt}$ as figure 31 in the following.

We can see the evolutionary trends for sb-, s/a-, and agn-Mb*N3*Rs in figures 31 and 36 and summarize them as follows. In all redshifts, the sb-Mb*N3*Rs mainly stay in the area $U - V - \Delta_{\rm UV} < 1$. This can be interpreted because they are on-going in star formation. On the other hand, the agn-Mb*N3*Rs start to appear even around $U - V - \Delta_{\rm UV} < 1$ at $z \geq 1.2$ with large scatters in a mass range $> 3 \times 10^{10}\,M_\odot$, and relatively concentrate around $U - V - \Delta_{\rm UV} \sim 1$ at $0.8 \leq z < 1.2$, as shown in the bottom diagrams of figure 31. This trend, that starbursts are bluer than AGNs at $0.8 \leq z < 1.2$, can be seen not only for the Mb*N3*Rs, but also for the Mm*N3*Rs in figure 33. Figures 31 and 33 also show that the sb-Mm*N3*Rs are relatively redder than the sb-Mb*N3*Rs for the same stellar mass. This is reasonable, since the former with less luminous IR emissions may have smaller *SFR*s and quench their star-formation activities more effectively than the latter.

As shown in the middle of figure 31, the s/a-Mb*N3*Rs have a similar stellar population to the sb-Mb*N3*Rs at $z \geq 0.8$, even though some of them were $U - V - \Delta_{\rm UV} > 1$. Thus, a dusty star formation cannot suffer from obscured AGN activity at $z \geq 0.8$, at least. On the other hand, at $z < 0.8$, it is similar to the agn-Mb*N3*Rs around $U - V - \Delta_{\rm UV} \sim 1$. Passive populations, such as the p-BBGs and on the red sequence, are relatively major in s/a-Mb*N3*Rs at $0.8 \leq z < 1.2$. This suggests the co-existence of the obscured AGN with passive stellar populations in their hosts, which are older than those in the sb-Mb*N3*Rs. Thus, the stellar populations already become passive in massive galaxies, such as the s/a-Mb*N3*Rs of $\simeq 10^{11}\,M_\odot$, with obscured AGNs, even at $z \simeq 1$; also, the obscured AGNs are activated in less-massive galaxies of $< 10^{11}\,M_\odot$, mainly with star formation at $z < 0.8$. These indications from the CMDs are consistent with the indication about quenching *SFR*s of the s/a-Mb*N3*Rs at $z < 0.8$ from figures 25 and 26. It suggests that the evolution of AGN activity is more rapid than that of star formation around $z = 1$–2, and that the co-evolutionary link between AGN activity and star formation in galaxies can be critical around $z \simeq 1$. This seems to remind us of a scenario that AGN activity may quench star formation in the distant universe to explain *downsizing*.

10. Evolution of AGN Activities

10.1. AGN Activity Traced at Rest-Frame 5 μm

Figure 37 shows the rest-frame absolute monochromatic luminosities $\nu L_{\nu,5}$ at 5 μm to their stellar mass, M_*, derived with equation (4), for the agn-Mb*N3*Rs, the s/a-Mb*N3*Rs, and the sb-Mb*N3*Rs. We can see an evolutionary trend, since the agn-Mb*N3*Rs at higher redshifts are more luminous at 5 μm. The mass and evolutionary trend for $\nu L_{\nu,5}$ is roughly summarized as

$$\nu L_{\nu,5}\,(L_\odot) \simeq L_{11} \left(\frac{M_*}{10^{11} M_\odot} \right)^{\alpha} (1+z)^{\beta}\,. \qquad (25)$$

In figure 37, the data points of the Mb*N3*Rs are plotted in redshift intervals of $0.4 \leq z < 0.8$, $0.8 \leq z < 1.2$, $1.2 \leq z$, respectively. The solid line for agn- and s/a-Mb*N3*Rs at $z = 0.6$, 1.0, and 1.5 represents the best-fitted plane of $\log(L_{11}/L_\odot) = 8.9 \pm 0.1$, $\alpha = 0.15 \pm 0.08$, and $\beta = 6.3 \pm 0.4$ in equation (25). On the other hand, the solid lines for sb-Mb*N3*Rs represent the plane of $\alpha = 0.74$ and $\beta = 2.7$, which are the same exponents of equation (23) for star-forming activities in subsection 7.1. Thus, the 5-μm emissions of the sb-Mb*N3*Rs are dominant from their dusty star-forming regions.

The trends for the 5-μm luminosities do not depend on their selections, since $\nu L_{\nu,5}$ of the Mb*N3*Rs is larger than the limiting luminosities for their detection as $\simeq 10^9$, 6×10^9,

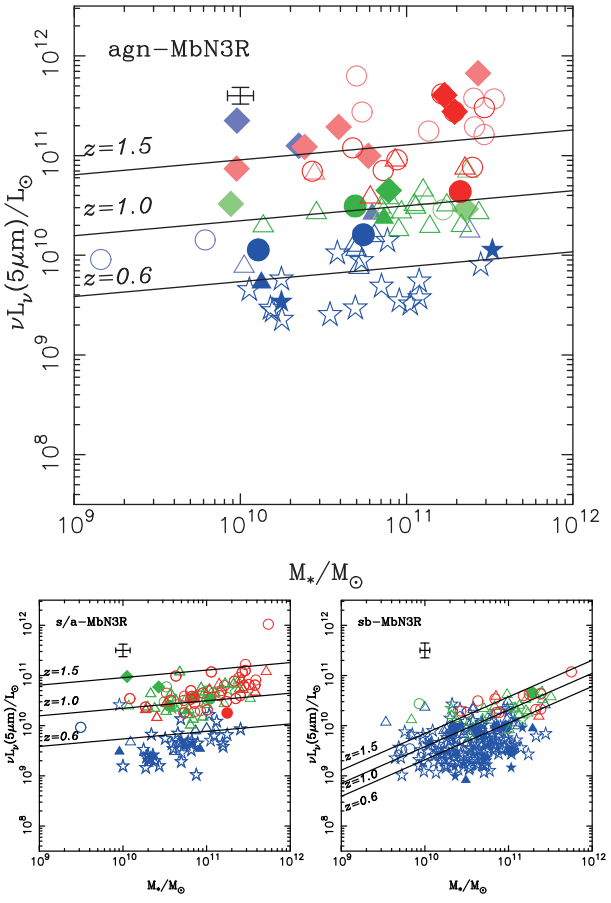

Fig. 37. Correlation between stellar mass M_* vs. $\nu L_{\nu,5}$ at rest-frame 5 μm for the Mb*N3*Rs. Symbols represent the same as in figure 6 except for the colors. The blue, green, and red symbols represent objects at the redshifts of $0.4 \leq z < 0.8$, $0.8 \leq z < 1.2$, and $z \geq 1.2$, respectively. Diamonds represent the spectroscopic BL AGNs. Dark and faint symbols represent objects with reduced $\chi^2 < 0.5$ and $\chi^2 > 0.5$ in the MIR SED fitting, respectively. Top: For the agn-Mb*N3*Rs. Bottom-left: For the s/a-Mb*N3*Rs. Bottom-right: For the sb-Mb*N3*Rs.

and $2 \times 10^{10}\,L_\odot$ at $z = 0.5$, 1.0, and 1.5, respectively. Thus, the emission process at the rest-frame 5 μm for the agn- and s/a-Mb*N3*Rs should be different from the dusty star-forming origin for the sb-Mb*N3*Rs. This supports the supposition that MIR emissions from the agn-Mb*N3*Rs are dominated by obscured AGN. Thus, it is expected that the 5-μm luminosity, $\nu L_{\nu,5}$, may dominate in the bolometric luminosity of the obscured AGN $L_{\rm bol}$ for the s/a- and agn-Mb*N3*Rs.

The evolutionary trend of $\nu L_{\nu,5}$ in the agn-Mb*N3*Rs is more rapid than that of *SFR*s in the sb-Mb*N3*Rs. $\nu L_{\nu,5}$ in the agn-Mb*N3*Rs at $0.8 \leq z < 1.2$ and $0.4 \leq z < 0.8$ also becomes less scattered than those at $z \geq 1.2$, which can be attributable to quenching the AGN activities around $z \simeq 1$.

The analysis with $\nu L_{\nu,5}$ can also apply for the Mm*N3*Rs, as shown in figure 38, even though they are biased, since most of them are detected in a critical threshold at the rest-frame 5 μm. The sb-Mm*N3*Rs and the non sb-Mm*N3*Rs show roughly a similar trend to those of the sb-Mb*N3*Rs and the s/a-Mb*N3*Rs compared with the agn-Mb*N3*Rs, which suggests that AGN activities are not dominant in the Mm*N3*Rs.

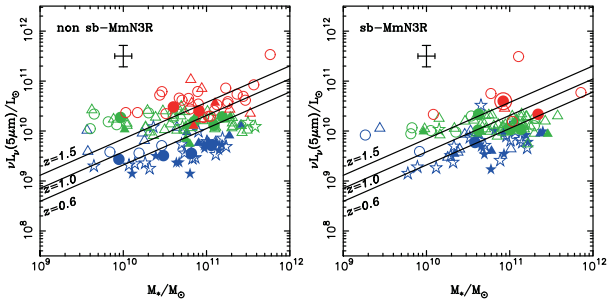

Fig. 38. Same as figure 37 for the Mm*N3*Rs. Left: For the non sb-Mm*N3*Rs. Right: For the sb-Mm*N3*Rs.

10.2. Super Massive Black Holes in AGNs

Consider accretion onto a Super Massive Black Hole (SMBH) with mass $M_{\rm BH}$ for an AGN. The bolometric luminosity, $L_{\rm bol}$, of the emission from the AGN is characterized by an Eddington ratio, λ, of $L_{\rm bol} = \lambda L_{\rm Edd}$ and an Eddington luminosity, $L_{\rm Edd}$, of

$$L_{\rm Edd}\,({\rm erg\ s^{-1}}) = 1.26 \times 10^{38} \left(\frac{M_{\rm BH}}{M_\odot}\right). \tag{26}$$

Introducing a luminosity ratio, $f_5 = \nu L_{\nu,5}/L_{\rm bol}$, we can obtain a constraint for the mass of the SMBH from the 5-μm luminosity $\nu L_{\nu,5}$ as

$$\frac{M_{\rm BH}}{3.06 \times 10^6\,M_\odot} = \lambda^{-1} f_5^{-1} \frac{\nu L_{\nu,5}}{10^{11}\,L_\odot}. \tag{27}$$

We can see $\nu L_{\nu,5} \simeq 10^{12}\,L_\odot$, and $3 \times 10^{10}\,L_\odot$ at the maximum and minimum, respectively, for the agn-Mb*N3*Rs of $M_* \simeq 10^{11}\,M_\odot$ at $z > 1.2$ in figure 37. This means that SMBHs have already grown in a mass range of $\simeq 10^6 \lambda^{-1} f_5^{-1}\,M_\odot$–$3 \times 10^7 \lambda^{-1} f_5^{-1}\,M_\odot > 10^6\,M_\odot$ in a host of $M_* \simeq 10^{11}\,M_\odot$ selected as the agn-Mb*N3*Rs at $z > 1.2$. Furthermore, as long as $\lambda f_5 > 10^{-1}$, the BH mass in a maximum 5-μm luminous agn-Mb*N3*R of $M_* \simeq 10^{11}\,M_\odot$ at $z > 1.2$ does not exceed $3 \times 10^8\,M_\odot$, which is a similar value, attributable to the relation between the mass of the SMBH and the stellar mass in the local spheroid, as derived by Häring and Rix (2004):

$$\log M_{\rm BH} = -4.12 + 1.12\,(\log M_*). \tag{28}$$

If the mass relation between SMBH and the host was already established at $z > 1.2$ as this equation (28) in the local universe, then the AGN luminosity in the agn-Mb*N3*Rs at $z > 1.2$ could be near the Eddington limit, $\lambda \simeq 1$, which is consistent with the following consideration about SMBH growth history.

Introducing an energy conversion efficiency, $\epsilon = L_{\rm bol}/(\dot{M}c^2)$ for mass accretion with $\dot{M}$ onto an SMBH, the 5-μm luminosity $\nu L_{\nu,5}$ also implies a constraint for the mass growth ratio, $\dot{M}_{\rm BH}$, of SMBHs as

$$\frac{\dot{M}_{\rm BH}}{6.8 \times 10^{-3}\,M_\odot\,{\rm yr^{-1}}} = (1-\epsilon)\epsilon^{-1} f_5^{-1} \frac{\nu L_{\nu,5}}{10^{11}\,L_\odot}, \tag{29}$$

where we have used $\dot{M}_{\rm BH} = (1-\epsilon)\dot{M}$ and $\nu L_{\nu,5} = f_5 L_{\rm bol}$. The thin-disk accretion model has predicted that the efficiency, ϵ, should be in the range $\simeq 0.04$–0.31, depending on the spin

of the SMBH. The growth time scale of SMBHs is also represented as

$$\frac{M_{\rm BH}}{\dot{M}_{\rm BH}}\,({\rm yr}) = 4.5\times10^{8}\lambda^{-1}\frac{\epsilon}{(1-\epsilon)}\,. \quad (30)$$

Then, the SMBH growth time could be less than the time of $\simeq 2.5$ Gyr from $z = 2$ to $z = 1$ for $\lambda/\epsilon > 0.2$, which can be satisfied as long as it is near the Eddington limit with $\lambda > 0.06$ for assuming the thin-disk accretion model with $\epsilon = 0.04$–0.31. Thus, it is consistent with the suggestion that SMBHs had already grown in the maximum 5-μm luminous agn-Mb*N3*Rs of $M_* \simeq 10^{11}\,M_\odot$ at $z > 1.2$, and their AGN luminosity could be near the Eddington limit, $\lambda \simeq 1$, as discussed above.

10.3. AGN Activity and Star Formation

Even though the sb-Mb*N3*Rs and the agn-Mb*N3*Rs are different populations, we could obtain simple formulae representing the activity of star formation and obscured AGN in the Mb*N3*Rs up to $z \simeq 2$ with functions of their stellar mass and redshift as equations (23) and (25). The 5-μm luminosity of the agn-Mb*N3*Rs is rapidly quenching as equation (25) compared with that of sb-Mb*N3*Rs as equation (23). This means that the evolutionary time scale of AGN activity is shorter than that of star formation for the Mb*N3*Rs selected with the AKARI MIR photometry.

The rapid evolutionary trend of AGNs in the Mb*N3*Rs was already expected from its color of stellar population, as discussed in section 9. Thus, this evolutionary trend in the time scales, which distinguishes between the agn-Mb*N3*Rs and the sb-Mb*N3*Rs, is consistent with the evolutionary feature of the Mb*N3*Rs around $z \simeq 1$ in their distribution on the color–mass diagram, as shown in figure 31.

11. Discussions

11.1. FIR and Submm Follow-Ups

As discussed in subsection 7.3, the s-Mb*N3*Rs and the sb-Mm*N3*Rs with a lower ratio of monochromatic luminosity at rest-frame 10 μm to that at 7.7 μm: $\nu L_{\nu,10}/\nu L_{\nu,7.7}$ tend to have larger extinctions, assuming denser dust distributions (see figure 21). Larger extinctions, indicated with $\nu L_{\nu,10}/\nu L_{\nu,7.7}$, can make reprocessed photon emissions dominant at longer wavelengths. This trend can be confirmed in the left plot of figure 39, which shows the average IR/Submm SEDs for the s-Mb*N3*Rs fitted well with large, medium, and small optical depth parameters in the S&K model; $A_{V;{\rm SK}} = 17.9$, 6.7, and 2.2, respectively. The s-Mb*N3*Rs with a larger optical depth tend to show not only a deeper dip at 10 μm, but also a larger flux in FIR and Submm wavelengths. This feature can be confirmed directly with observations with FIR devices, such as the Photodetector Array Camera (PACS) and Photometric Imaging Receiver (SPIRE) on board Herschel and Submm telescopes as MAMBO/IRAM and ALMA. Figure 39 shows the expected monochromatic luminosity at rest-frame (600 μm): νL_ν(600 μm) vs. $\nu L_{\nu,10}/\nu L_{\nu,7.7}$ as the trend between extinctions and FIR/Submm wavelength excess.

Observations with ground-based Submm telescopes as SCUBA and MAMBO have reported that so-called high-z SubmilliMeter Galaxies (SMGs) tend to have SEDs reproduced with lower dust temperatures when compared with local ULIRGs (e.g., Chapman et al. 2004), which suggests that detection of SMGs with ground-based Submm telescopes could be biased, and there are missing populations of star-forming galaxies with hotter dust as Optically Faint Radio Galaxies (OFRGs). Recently PACS and SPIRE/Herschel observations have revealed that ULIRGs at $z \simeq 2$, detected with the MIPS/Spitzer, consist of both cold and warm populations corresponding to the SMGs and the OFRGs (Magdis et al. 2010; Elbaz et al. 2011), respectively. Even though it is not clear yet how our samples of Mb*N3*Rs and Mm*N3*Rs are related to the Herschel detected ULIRG samples, since our samples were detected in the MIR bands, and correspond to LIRGs at $z \simeq 1$, the variety of $\nu L_{\nu,10}/\nu L_{\nu,7.7}$ suggests that LIRGs at $z \simeq 1$ may consist of various populations with cold and warm dust, similar to the ULIRGs at $z \simeq 2$, such as the SMGs. The forthcoming and future observations with Herschel and Submm telescopes will confirm these features, as predicted in figure 39.

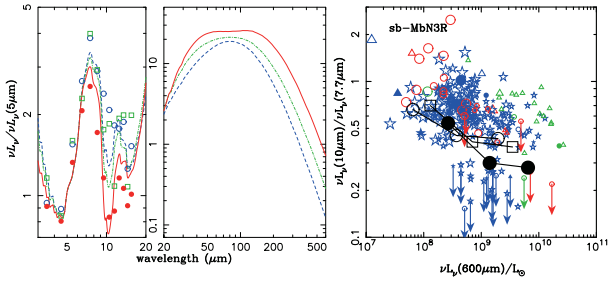

Fig. 39. Left: Averaged rest-frame IR–Submm SEDs for the sb-Mb*N3*Rs. Red filled circles, green open squares, and blue open circles represent the monochromatic luminosity, νL_ν, averaged for the sb-Mb*N3*Rs, which fit well with large, medium, and small optical depth S&K models of $A_{V;{\rm SK}} = 17.9$, 6.7, and 2.2, respectively. Red solid, green dotted, and blue dashed lines represent model SEDs with $A_{V;{\rm SK}} = 17.9$, 6.7, and 2.2, respectively. The model SEDs have been convoluted within a 3 μm wavelength corresponding to a mean width of the AKARI/IRC bands. Right: Expected monochromatic luminosity at rest-frame 600 μm: νL_ν(600 μm) vs. monochromatic luminosity ratio at rest-frame 10 μm to 7.7 μm: $\nu L_{\nu,10}/\nu L_{\nu,7.7}$ for a case with TIR luminosity $L_{\rm IR} = 5\times10^{11}\,L_\odot$. Black filled circles, open squares, and open circles represent monochromatic luminosities $\nu L_{\nu,10}/\nu L_{\nu,7.7}$ from the convoluted S&K models with $A_{V;{\rm SK}} = 17.9$, 6.7, and 2.2, respectively. We have taken other S&K model parameters as $L^{\rm tot} = 10^{10.1}$, $10^{11.1}$, and $10^{12.1}\ L_\odot$ from right to left and fixed $L_{\rm OB}/L^{\rm tot} = 0.6$.

Adding these photometric data at these longer wavelengths for the Mb*N3*Rs can also serve as a strong constraint in the SED analysis with direct estimations of their TIR luminosities, which can overcome any ambiguity left in deriving the absolute TIR luminosity by introducing the proportional factor, $f_{\rm SK}$, in section 7. Furthermore, adding FIR/Submm photometry makes a distinction between starborst dominant and AGN dominant, which is an alternative way to determine the MIR color criteria for selecting s- and agn-Mb*N3*Rs in this work. An alternative selection for AGNs can be also effective to study the census of AGN populations. As shown in subsection 6.1, the CXO found that some agn- and s/a-Mb*N3*Rs are associated with X-ray sources. On the other hand, there are still some populations in the agn- and s/a-Mb*N3*Rs escaping from X-ray

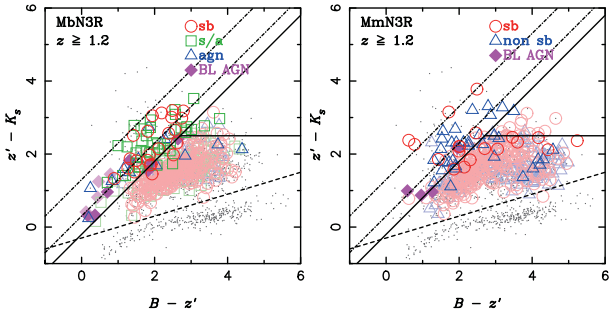

Fig. 40. BzK color diagram for the Mb$N3$Rs and Mm$N3$Rs. Large dark and faint symbols represent galaxies at $z \geq 1.2$ and $z < 1.2$, resepectively. The small dots represent the MIR faint galaxies with $K < 21$. Dashed line represents a boundary line separating stars and galaxies with equation (1) as discussed in subsection 3.3. Left: For the Mb$N3$Rs. Red open circles, green open squares, blue open triangles, and magenta filled diamonds represent sb-, s/a-, agn-Mb$N3$Rs and BL AGNs, respectively. Right: For the Mm$N3$Rs. Red open circles, green open squares and magenta filled diamonds represent sb-, non sb-Mm$N3$Rs, and BL-AGNs, respectively.

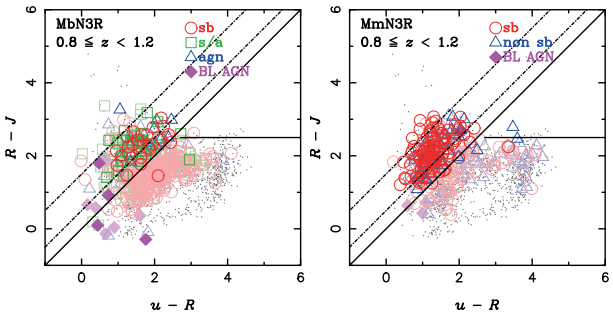

Fig. 41. Same as figure 40 for the uRJ color diagram. Large dark and faint symbols represent galaxies at $0.8 \leq z < 1.2$ and $z < 0.8$, respectively. Small dots represent the MIR faint galaxies with $J < 22$.

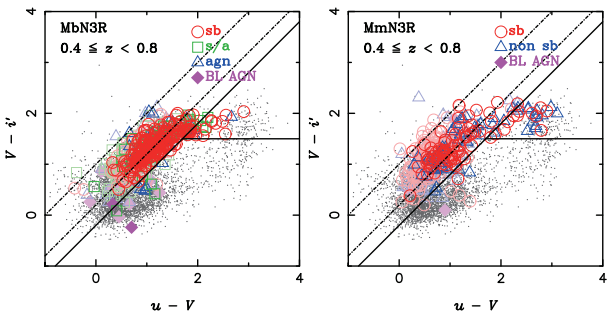

Fig. 42. Same as figure 40 for the uVi color diagram.

detection with the CXO. This suggests that obscured AGNs in the agn- and s/a-Mb$N3$Rs can be classified to two subpopulations associated with and without X-ray sources. The former and the latter are possible candidates of obscured AGNs in the Compton-thin range of $N_{\rm H} \leq 10^{24}\,{\rm cm}^{-2}$ and the Compton-thick (CT) range of $N_{\rm H} > 10^{24}\,{\rm cm}^{-2}$, respectively. Thus, the comparison of MIR–FIR/Submm SEDs between the CT and non-CT AGN candidates is expected to supply constraints for

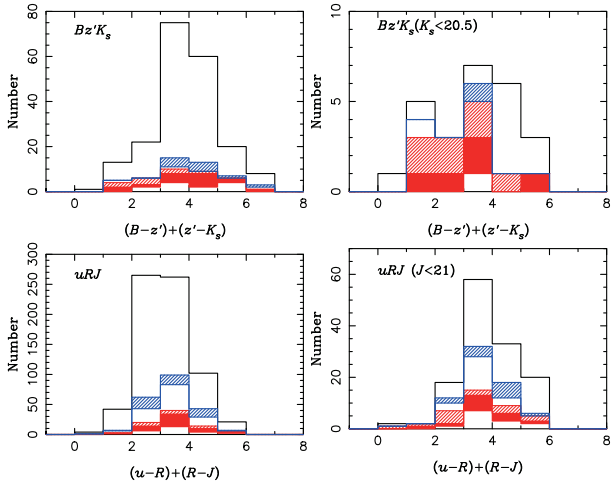

Fig. 43. Color distribution of the Mb$N3$Rs along the strip between the dotted-dashed lines in figures 40 and 41. The top solid line histogram indicates the number of galaxies detected in the NIR band. Red slashed, filled, and outline histograms represent agn-, s/a-, and sb-Mb$N3$Rs, respectively. Blue slashed and outline histograms represent the non sb-Mm$N3$Rs and sb-Mm$N3$Rs, respectively.

physical states around the SMBHs in obscured AGNs.

11.2. Optical Colors of MbN3Rs and MmN3Rs

Most of the Mb$N3$Rs and Mm$N3$Rs are also classified as BBGs. Thus, we have also compared the sb-, s/a-, and agn-Mb$N3$Rs with their colors on two-color diagrams related to the BBG criteria derived in appendix 1. Figures 40, 41, and 42 show that the s-Mb$N3$Rs and the sb-Mm$N3$Rs mainly concentrate around $(B - z, z - K) \simeq (2, 2.5)$, $(u - R, R - J) \simeq (2, 2.5)$, and $(u - V, V - i) \simeq (1.5, 1.5)$, while the agn-Mb$N3$Rs are relatively more dispersed than the s-Mb$N3$Rs. These $\mathcal{B}\mu\mathcal{R}$ colors (see appendix 1.2) of the s-Mb$N3$Rs and the sb-Mm$N3$Rs are consistent with those expected from reddenings with heavy extinctions, as shown by Daddi et al. (2004) and in appendix 1. We detected $\sim$60 s-BzKs and $\sim$100 s-uRJs with $K < 21.5$ and $J < 22$ in the color region within $\Delta(B - K) \simeq \pm 0.5$ and $\Delta(u - J) \simeq \pm 0.5$ around $(B - z, z - K) \simeq (2, 2.5)$ and $(u - R, R - J) \simeq (2, 2.5)$, respectively, where $\sim$15 and $\sim$40 out of these s-BzKs (s-uRJs) are classified as s-Mb$N3$Rs, as shown on the left in figure 43. Thus, roughly, we can detect dusty starbursts at $z \sim 1$–2 with a frequency one fifth of s-BzKs and one third of s-uRJs. For NIR bright BBGs with $K < 20.5$ and $J < 21$, the fractions of Mb$N3$Rs and Mm$N3$Rs in BBGs increase as shown on the right in figure 43. In particular, roughly half of the uRJs with $J < 21$ around $(u - R, R - J) \simeq (2, 2.5)$ are LIRGs around $z \sim 1$, which are selected in the NEP deep field. We should note that this NEP deep field is a blank field. Thus, these kinds of BBGs constrained with NIR brightness and colors in any blank field can be mostly detected as LIRGs around $z \sim 1$–2, which are interesting targets for a future unbiased survey for galaxies with on-going, up-coming, or future FIR/Submm telescopes as Herschel and ALMA. These future studies will be also essential to confirm the trends for the populations marginally detected with the AKARI as the Mm$N3$Rs.

12. Conclusions

We have studied IRBGs/LIRGs in three redshift ranges of $z = 0.4$–0.8, 0.8–1.2, and > 1.2 with MIR multiband photometry, which revealed their star-forming/AGN activities with/without PAH emissions deriving *SFR* from their TIR luminosities.

- The MIR colors and SED analysis can classify MIR bright *N3* Red galaxies (Mb*N3*Rs) into three classes: starburst dominates (sb-Mb*N3*Rs), starburst/AGN co-existence (s/a-Mb*N3*Rs), and AGN dominates (agn-Mb*N3*Rs). The ratio of rest-frame luminosities at 5 and 10 μm to that at 7.7 μm is systematically higher in the s/a-(agn-)Mb*N3*Rs than in the sb-(s/a-)Mb*N3*Rs, which is consistent with the picture of the s/a-Mb*N3*Rs as the starburst/AGN co-existent subpopulation in the dusty star-forming Mb*N3*Rs (s-Mb*N3*Rs).
- MIR marginally-detected *N3*Rs (Mm*N3*Rs) can also be classified into two classes: sb-Mm*N3*Rs as mimics of sb-Mb*N3*Rs, and non sb-Mm*N3*Rs.
- Their rest-frame 7.7-μm luminosity is a good tracer of the TIR luminosity, since the PAH emission dominates the sb- and s/a-Mb*N3*Rs and sb-Mm*N3*Rs, which are classified as dusty star-forming galaxies, even up to $z = 2$.
- The $SFR_{\rm IR+UV}$ derived from the total bolometric luminosity $L_{\rm IR+UV}$ of the sb-Mb*N3*Rs/Mm*N3*Rs shows a correlation that is nearly proportional to the stellar mass M_*, which is consistent with that of the extinction corrected UV star formation ratio, $SFR_{\rm UV;cor}$.
- The $SFR_{\rm IR+UV}$ of the s/a-Mb*N3*Rs tends to be smaller than that of the sb-Mb*N3*Rs at $z < 0.8$.
- The specific $SFR_{\rm IR+UV}$ of the sb-Mb*N3*Rs/Mm*N3*Rs rises with the redshift at all stellar masses.
- The ratio of the rest-frame luminosity at 10 μm to that at 7.7 μm of the sb-Mb*N3*Rs/Mm*N3*Rs may trace the optical depth due to dust extinction.
- The AGN activity could be traced with the rest-frame 5-μm luminosity for the agn- and s/a-Mb*N3*Rs. The evolutionary trend $(1 + z)^6$ of the AGN luminosity for the agn-Mb*N3*Rs is more rapid than $(1 + z)^3$ of *SFR* for the sb-Mb*N3*Rs/Mm*N3*Rs.
- SMBHs in the galaxies have grown to $\simeq 3 \times 10^8\,M_\odot$ in maximum luminous populations with $10^{12}\,L_\odot$ and $10^{11}\,M_\odot$ of the MIR selected AGNs at $z > 1.2$, which suggests that the mass relation between the SMBH and its host is already established at $z \simeq 1$–2, and the same as that at the present day.

This study is based on data mostly collected with the AKARI IR astronomical satellite and at the Subaru Telescope, which are operated by the ISAS/JAXA and the National Astronomical Observatory of Japan, respectively. We would like to thank their staff for their invaluable assistance. We thank B. Weiner and C. Papovich for their help in the spectroscopic observation with the Hectospec/MMT under TSIP program of National Optical Astronomy Observatory. We are grateful to an anonymous referee for his/her comments, which have helped to clarify the paper. HH thanks P. Langman, Iwate University, for proofreading the English writing. This research was mostly supported for HH by the Grant-in-Aid for Scientific Research (21340042) from Japan Society for the Promotion of Science (JSPS), and partly supported for MI by the Korea Science and Engineering Foundation (KOSEF) grant no. 2010-0000712 from the Korea government (MEST).

Appendix 1. Classification with Balmer/4000 Å Breaks

In order to identify galaxies at various redshift intervals, we generalized the two-color technique for detecting the Balmer/4000 Å break, which is a major feature in the SED of galaxies. The Balmer and 4000 Å breaks are often treated as a single feature, owing to their similar wavelengths and overlapping populations of galaxies having these features. However, the breaks originate due to different physical processes, and behave differently as a function of the age and population. Both breaks result from absorption in the stellar atmospheres. The "classical" Balmer break at 3648 Å marks the termination of the hydrogen Balmer series, and is strongest in A-type stars. This means that it is the most prominent feature for intermediate ages of 0.3–1.0 Gyr in a Single Stellar Population (SSP). The Balmer break strength, $D_{\rm B}$, is defined as the ratio of the flux density, F_ν, in the 3500–3650 Å and 3800–3950 Å bands around the break (Balogh et al. 1999). On the other hand, the 4000 Å break arises because of an accumulation of absorption lines of mainly, ionized metals. Its strength is defined using an index, $D_n(4000)$, that is based on the continuum regions, and the ratio of the flux density F_ν in the 3850–3950 Å and 4000–4100 Å bands. As the opacity increases with decreasing stellar temperature, the 4000 Å break strength, $D_n(4000)$, increases for older ages, and is largest in old and metal-rich stellar populations. However, the Balmer break strength $D_{\rm B}$ does not monotonically increase with age, instead reaches a maximum at intermediate ages (Kriek et al. 2006). The metallicity has a more minor influence for ages less than 1 Gyr (Bruzual & Charlot 2003). Thus, both break features at around 4000 Å include information about the stellar populations in a galaxy. Although these breaks are individually unresolved from broad-band photometry, the degenerate Balmer/4000 Å break still provides a robust feature in the SEDs with galaxies of an age $t > 500$ Myr. In the following subsections, we demonstrate that the Balmer/4000 Å break can be used to select galaxies at various redshift intervals of interest to this work.

A.1.1. The BzK, uRJ, and uVi Color–Color Diagram

Daddi et al. (2004) proposed that $z > 1.4$ star-forming BBGs (s-BBGs) should occupy the upper-left region in a two-color $B - z$ and $z - K$ (BzK) diagram, as the bluer and redder colors trace UV excess and the Balmer/4000 Å break feature, representing the star-forming activity and the old stellar component, respectively. We could also show that the BzK technique is efficient for selecting galaxies at $1.4 < z_{\rm phot} < 2.5$, as illustrated in figure 44.

We will argue that this kind of two-color technique can be extended to select s-BBGs at certain redshift intervals with other sets of three photometric observed broad bands, in which

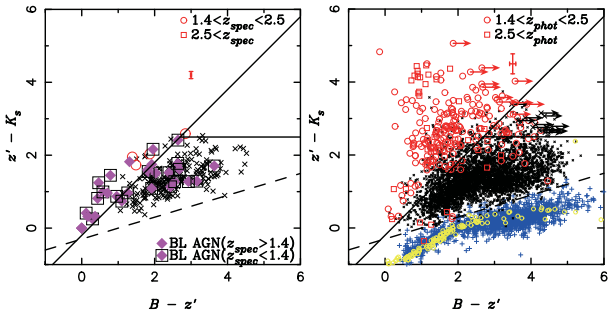

Fig. 44. *BzK* diagrams in the field. Symbols of cross bar at ($B - z'$, $z' - K_s$) = (3, 4.5) represent typical errors of the color. Magenta diamonds represent BL AGNs, in which squared diamonds represent lower-redshifted ones at $z < 1.4$. Dashed line represents a boundary line separating stars and galaxies with equation (1) as disswssed in subsection 3.3. Left: For the spectroscopic samples, red circles represent sources at $z_{\rm spec} = 1.4$–2.5. Right: Same as on the left for the photometric samples, where blue cross and yellow circles represent the stellar objects selected with the scheme described in subsection 3.4, and the reference stars of the BPGS star atlas as introduced in subsection 3.3, respectively. Red circles and squares represent sources at $z_{\rm phot} = 1.4$–2.5 and at $z_{\rm phot} > 2.5$, respectively.

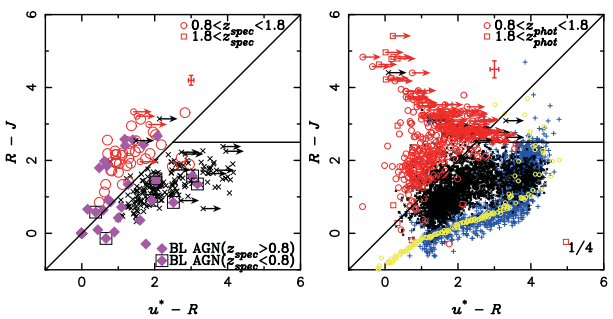

Fig. 45. Same as figure 44 for the *uRJ*s. The symbols of the cross bar at ($u^* - R$, $R - J$) = (3, 4.5) represent typical errors of the color. Red circles and squares represent sources at $z_{\rm phot} = 0.8$–1.8 and at $z_{\rm phot} > 1.8$, respectively. Left: For the spectroscopic samples. Right: For the photometric samples. Only one fourth of all photometric sources detected in the *uRJ* bands are plotted, so as to reduce crowding in the diagram.

their wavelengths are nearly in an equal ratio as a geometric series. By introducing $\mathcal{B}$, μ, and $\mathcal{R}$ as their *AB* magnitudes of general bluer, medium, and redder bands, resepectively, and defining a two-color index $\mathcal{B}\mu\mathcal{R}$ generalized in *BzK*,

$$\mathcal{B}\mu\mathcal{R} \equiv (\mu - \mathcal{R}) - h_{\mathcal{B}\mu\mathcal{R}}(\mathcal{B} - \mu), \quad \text{(A1)}$$

it follows that s-BBGs at certain redshift intervals can be selected by a criterion,

$$\mathcal{B}\mu\mathcal{R} \geq f_{\mathcal{B}\mu\mathcal{R}}, \quad \text{(A2)}$$

and passively evolving BBGs (p-BBGs) can be selected with a criterion,

$$\mathcal{B}\mu\mathcal{R} < f_{\mathcal{B}\mu\mathcal{R}} \cap (\mu - \mathcal{R})_{AB} > g_{\mathcal{B}\mu\mathcal{R}}\ . \quad \text{(A3)}$$

Even though we can obtain only the upper limit in their $\mathcal{B}$ magnitudes, we can select quasi passively evolving BBGs (qp-BBGs) with a criterion,

$$(\mu - \mathcal{R})_{AB} > g_{\mathcal{B}\mu\mathcal{R}}\ . \quad \text{(A4)}$$

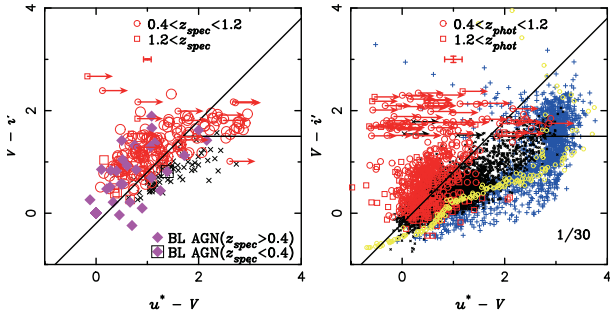

Fig. 46. Same as figure 44 for the *uVi*s. The symbols of the cross bar at ($u^* - V$, $V - i'$) = (1, 3) represent typical errors of the color. Red circles and squares represent sources at $z_{\rm spec} = 0.4$–1.2 and $z_{\rm spec} > 1.2$, respectively. Left: For the spectroscopic samples. Right: For the photometric samples. Only one thirtieth of all photometric sources detected in the *uVi* bands are plotted, so as to reduce crowding in the diagram.

Table 6. Parameters for BBG selection.

Bands	$f_{\mathcal{B}\mu\mathcal{R}}$	$g_{\mathcal{B}\mu\mathcal{R}}$	$h_{\mathcal{B}\mu\mathcal{R}}$	$z_{\rm min}$	$z_{\rm max}$
uVi	−0.2	1.5	1.0	0.4	1.2
uRJ	0.0	2.5	1.0	0.8	1.8
BzK	−0.2	2.5	1.0	1.4	2.5
BRN3	0.7	3.0	3.0	0.8	1.8
uRN3	0.0	3.0	2.0	0.8	1.8
BzN3	−0.2	2.5	1.4	1.4	2.5
uzN3	−0.5	2.5	1.2	1.4	2.5

We confirm the validity of this generalized BBG technique, as shown in figures 45 and 46. These generalized criteria are efficient ways to select photometric s/p/qp-BBGs at $0.8 < z < 1.8$ and $0.4 < z < 1.2$ in the field for the *uRJ* and *uVi* filter sets. These particular color criteria also allow efficient selections of the BBGs not only for $1.4 < z < 2.5$, but also $0.8 < z < 1.8$ and $0.4 < z < 1.2$.

In order to study the validity and physical meaning of the two-color criteria that are generalized from the phenomenologically established *BzK* technique of Daddi et al. (2004), we used the BC03 model to reproduce the blue $\mathcal{B} - \mu$ and red $\mu - \mathcal{R}$ colors of model galaxies, which are described and shown in figures 57 and 58 in appendix 5.2. The result from the stellar population synthesis study is essentially similar to the cases of *BzK*s, as summarized below.

In the redshift ranges for each BBG selection in table 6, the galaxies with ongoing star formation appear in the upper-left region $\mathcal{B}\mu\mathcal{R} \geq f_{\mathcal{B}\mu\mathcal{R}}$ of the generalized $\mathcal{B}\mu\mathcal{R}$ color diagrams. The duration of the star formation (age) has little influence on the blue color $\mathcal{B} - \mu$, while the redder color $\mu - \mathcal{R}$ increases with age. Only very young starbursts with ages less than 10 Myr, and without underlying older stellar populations, are located around the lower-left region, falling just below the line of $\mathcal{B}\mu\mathcal{R} = f_{\mathcal{B}\mu\mathcal{R}}$. On the other hand, the colors of normal galaxies, obtained from the CWW SED templates (Coleman et al. 1980), fall outside the color area of the BBGs in the redshift ranges for each of the BBG selections. This means that

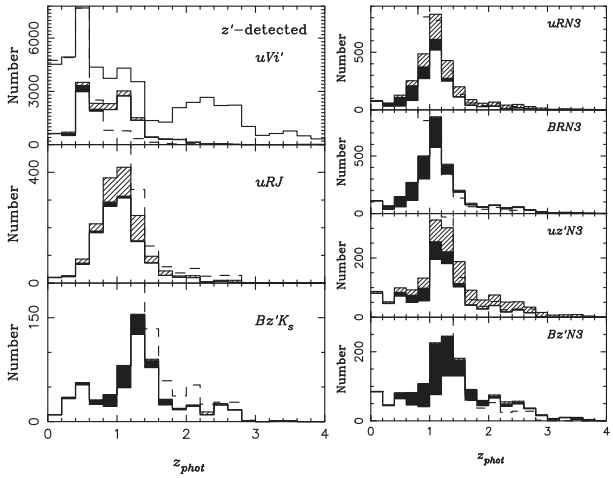

Fig. 47. Photometric redshift distributions for the BBGs in the field. The white, shaded, and dark areas represent the s-, qp-, and p-BBGs, respectively. Left: For the classical BBGs. Right: Same as on the left for the extended BBGs. Left-top: Lower, upper solid line and dashed line histograms represent the *uVi*s, the z'-detected galaxies, and the rest-frame V-detected galaxies, respectively. Left-middle: For the *uRJ*s. Left-bottom: For the *BzK*s. Right-top: For the *uRN3*s. Right-upper-middle: For the *BRN3*s. Right-lower-middle: For the *uzN3*s. Right-bottom: For the *BzN3*s.

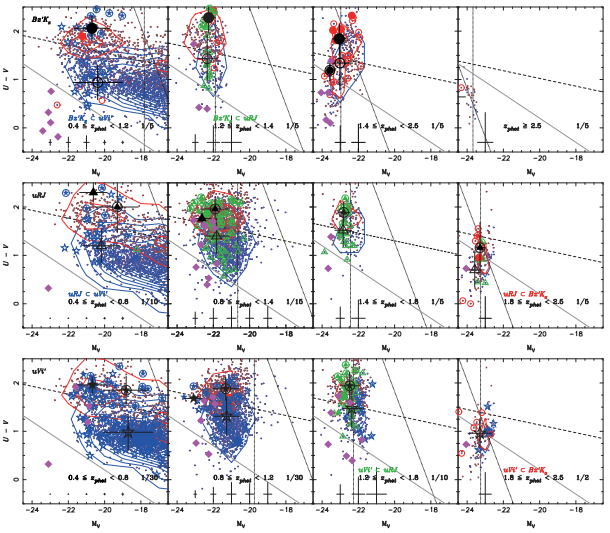

Fig. 48. Same as figure 2 for classical BBGs. Typical errors of the magnitude and color are represented with crosses at the bottom. The vertical dotted and steep slope dotted lines represent the limiting absolute V and U-band magnitudes at the mean redshift, respectively. In general, colored open and filled symbols and filled symbols in circles represent objects classified as s-, p-, and qp-BBGs, respectively. Basically, red circles, green triangles, and blue stars represent objects selected with the two-color criteria as *BzK*s, *uRJ*s, and *uVi*s, respectively. Black-large open and filled symbols and filled circles represent mean values for the s-, p-, and qp-BBGs, respectively. Crosses on the black symbols represent their standard deviations. Only a part of samples are plotted to reduce crowding in the diagram, whose fractions are presented as numbers in the right-bottom region of all figures. Top: *BzK*s at $0.4 \leq z < 1.2$, $1.2 \leq z < 1.4$, $1.4 \leq z < 2.5$, and $z \geq 2.5$ are plotted from left to right. For *BzK*s also classified as *uRJ*s at $1.2 \leq z < 1.4$, their symbols are changed to green triangles from red circles. For *BzK*s also classified as *uVi*s at $0.4 \leq z < 1.2$, the symbols are changed to blue stars from red circles. Middle: *uRJ*s at $0.4 \leq z < 0.8$, $0.8 \leq z < 1.4$, $1.4 \leq z < 1.8$, and $1.8 \leq z < 2.5$ are plotted from left to right. For *uRJ*s also classified as *BzK*s at $1.8 \leq z < 2.5$, their symbols are changed to red circles from green triangles. For *uRJ*s also classified as *uVi*s at $0.4 \leq z < 0.8$, their symbols are changed to blue stars from green triangles. Bottom: *uVi*s at $0.4 \leq z < 0.8$, $0.8 \leq z < 1.2$, $1.2 \leq z < 1.8$, and $1.8 \leq z < 2.5$ are plotted from left to right. For *uVi*s also classified as *uRJ*s at $1.2 \leq z < 1.8$, their symbols are changed to green triangles from blue stars. For *uVi*s also classified as *BzK*s at $1.8 \leq z < 2.5$, their symbols are changed to red circles from blue stars.

the generalized two-color criteria can also be used to exclude the lower-z objects.

The reddening direction lies approximately parallel to the line defined by $\mathcal{B}\mu\mathcal{R} = f_{\mathcal{B}\mu\mathcal{R}}$, since the dust extinction can be approximately represented by a power-law function of wavelength, implying that the reddening is similar in the $\mathcal{B} - \mu$ and $\mu - \mathcal{R}$ colors for star-forming galaxies in various redshift ranges. This means that the generalized criteria $\mathcal{B}\mu\mathcal{R} \geq f_{\mathcal{B}\mu\mathcal{R}}$ for selecting BBGs are also robust from their dust reddening.

Only a few galaxies are found as faint blue objects at $\mathcal{B} - \mu \simeq 0$, suggesting that purely un-reddened, star-forming galaxies are rare, not only for s-*BzK*s at $z \simeq 2$, but also s-*uRJ*s at $z \simeq 1$. On the other hand, we could find some fraction of these nearly extinction-free populations in s-*uVi*s at $z \simeq 0.6$.

Figure 47 shows the distributions of photometric redshifts, $z_{\rm phot}$, for all of the z'-detected galaxies and BBGs. The total numbers of detected *uRJ*s and *uVi*s as the lower-z BBGs are greater than that of detected *BzK*s, while the fractions of low-z interlopers in the *uRJ*s and *uVi*s are on the same order as those in the *BzK*s, as shown in figure 47. Thus, all of the BBG selections can be effective to exclude low-z interlopers at $z < 0.4$, $z < 0.6$, and $z < 1.2$ with the *uVi*, *uRJ*, and *BzK* criteria. These selected-out redshift ranges are consistent with the expected values of $z < 0.4$, $z < 0.8$, and $z < 1.2$ from the stellar population models (see appendix 5). While the *uVi*s are selected out at $z > 1.2$, as expected with the model tracks (see appendix 5), the *uRJ*s and *BzK*s gradually decrease in population at $z > 1.2$ and > 1.6, lower than expected. Low efficiency for BBG selections at the high redshift side may be caused from the shallowness of our ground-based NIR photometry. The limiting magnitudes of $J < 21$ and $K_{\rm s} < 22$ with the KPNO/FLMG are shallow compared with studies for the *BzK*s in other survey fields (Kong et al. 2006; Lane et al. 2007; Quadri et al. 2007; Blanc et al. 2008). Thus, we take into account this limitation of the ground-based NIR photometry in the dataset when we study galaxies at $z \simeq 0.8$–2 as *uRJ*s and *BzK*s. We try to overcome the limitation due to the shallow ground-based NIR photometry for the *uRJ*s and *BzK*s. We further extend the two-color criteria used for detecting the Balmer break in combination with AKARI NIR photometry, as discussed in appendix 1.3.

A.1.2. Rest Frame Color of the BBGs

It is worth comparing the classification with the two-color criteria detecting the Balmer break for the BBGs and their rest frame colors. As shown in the top and middle of figure 48, most of the *BzK*s at $1.2 \leq z_{\rm phot} < 1.4$ are classified as *uRJ*s while only a few of the *uRJ*s at $1.4 < z_{\rm phot} < 2.5$ are classified as *BzK*s. This is related to the shallowness in our ground-based

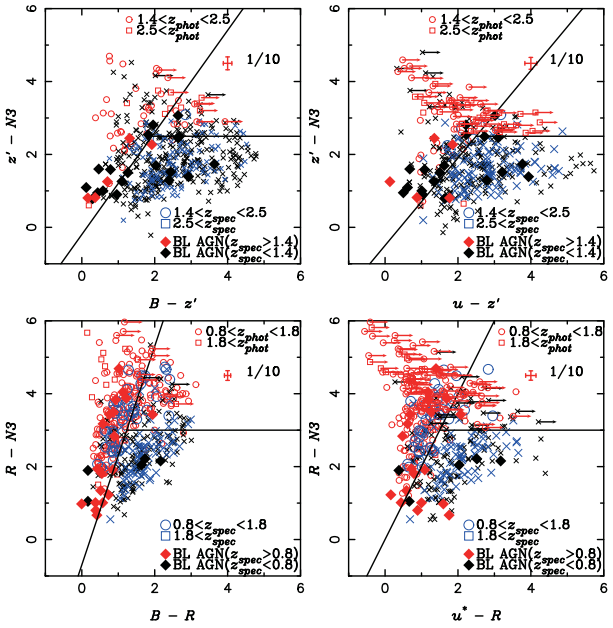

Fig. 49. Two-color diagrams for the extended BBGs selected from the *N3*Rs, in which the *N3* band is taken as the reddest band $\mathcal{R}$ in the BBG criteria. Red crosses at $(\mathcal{B} - \mu,\ \mu - \mathcal{R}) = (4, 4.5)$ represent typical errors of the color. Only a part of the *N3*Rs are plotted to reduce crowding in the diagram, whose fractions are presented as numbers at $(\mathcal{B} - \mu,\ \mu - \mathcal{R}) = (5, 4.5)$ in all figures. Diamonds represent BL AGNs. Large and small symbols represent the spectroscopic and the photometoric samples, respectively. Top-left: Same as figure 44 for the *BzN3*s. Circles and squares represent objects at $z = 1.4$–2.5 and $z > 2.5$, respectively. Top-right: Same as figure 44 for the *uzN3*s. Circles and squares represent objects at $z = 1.4$–2.5 and $z > 2.5$, respectively. Bottom-left: Same as figure 45 for the *BRN3*s. Circles and squares represent objects at $z = 0.8$–1.4 and $z \geq 1.4$, respectively. Bottom-right: Same as figure 45 for the *uRN3*s. Circles and squares represent objects at $z = 0.8$–1.4 and $z \geq 1.4$, respectively.

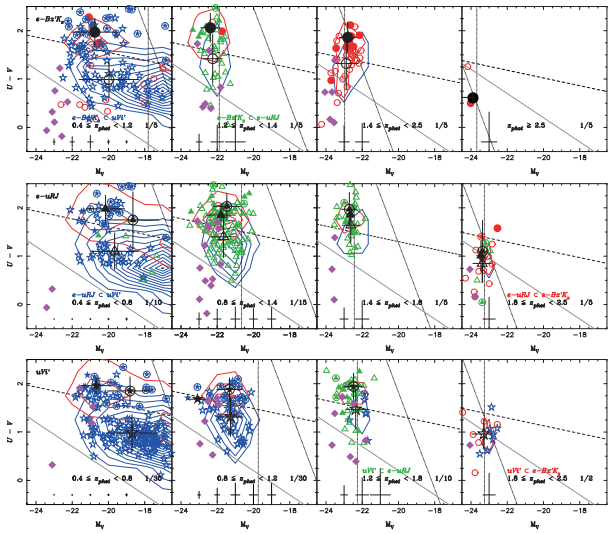

Fig. 50. Same as figure 48 for all the BBGs, including the extended BBGs. Top: For all the *BzK*s, including *uzN3*s and *BzN3*s. For *BzK*s + *uzN3*s + *BzN3*s also classified as *uRJ*s + *uRN3*s + *BRN3*s at $1.2 \leq z < 1.4$, their symbols are changed to green triangles from red circles. For *BzK*s + *uzN3*s + *BzN3*s also classified as *uVi*s at $0.4 \leq z < 0.8$, their symbols are changed to blue stars from red circle. Middle: Same as on the left for all the *uRJ*s, including *uRN3*s and *BRN3*s, as the top. For *uRJ*s + *uRN3*s + *BRN3*s also classified as *BzK*s + *uzN3*s + *BzN3*s at $1.4 \leq z < 2.5$, their symbols are changed to red circles from green triangles. For *uRJ*s + *uRN3*s + *BRN3*s also classified as *uVi*s at $0.4 \leq z < 0.8$, their symbols are changed to blue stars from green triangles. Bottom: Same as the top for the *uVi*s. For *uVi*s also classified as *uRJ*s + *uRN3*s + *BRN3*s at $1.2 \leq z < 1.8$, their symbols are changed to green triangles from blue stars. For *uVi*s also classified as *BzK*s + *uzN3*s + *BzN3*s at $1.8 \leq z < 2.5$, their symbols are changed to red circles from blue stars.

NIR photometry, which is not deep enough to select the population around $z \simeq 2$ as *BzK*s, as mentioned in the previous section. For our sample of up to $z \simeq 2$, the *uRJ* criteria are more useful than the *BzK* criteria. We can see the bimodality, even for the BBGs again as the boundary between the blue cloud and the red sequence is consistent with that by Bell et al. (2004), which are plotted as nearly horizontal dashed lines in figure 48. Even though the bimodality of BBGs at $z > 1.2$ is not so clear compared with that at $z < 1.2$, the mean colors of the s-BBGs and the p- and qp-BBGs, represented as black open and filled symbols and filled symbols in circles in figure 48, are in the blue cloud region and in the red sequence, respectively. Thus, the *uRJ* and *uVi* criteria can reasonably classify the star forming and the passively evolving populations as the s-BBGs and the p- and qp-BBGs at $z < 1.8$ in the field at least. This confirms that the generalized BBG criteria are also useful in order to distinguish a star-forming population from a passively evolving one.

A.1.3. Salvaging BBGs from N3Rs at z > 0.8

As shown in appendix 1.1, the BBG techniques employing not only the original *BzK* color but also the *uRJ* color can select galaxies around the redshift desert. However, we could not completely select these BBGs from the ground-based photometric dataset in the field since the ground-based JK_s photometry with the KPNO/FLMG is not deep enough to pick up the IRBGs detected with AKARI as seen in table 2. Since BBGs and IRBGs are almost the same populations at $z > 0.4$, as discussed above, their statistics can confirm the limitation of the *JK* depth. Roughly one third of *N4R*s and *N34* bumpers could not be identified as *BzK*s or *uRJ*s, as seen in the comparison between the left plot in figure 47 and the top-left plot in figure 4. Even though the limiting magnitude in the *N3* band is comparable to those in *J* and *K* photometry, as can be seen in table 2, the *N3* band is effective to detect emissions around the rest-frame 1.6-μm IR bump for the objects at $z > 1$ more than the *J* and *K* bands. In order to salvage these missing BBGs as non-*BzK*(non-*uRJ*) in *N3*Rs around the redshift desert, we used *N3* photometry instead of the ground-based NIR ones for BBG selections with *BzN3*/*uzN3* (*uRN3*/*BRN3*) colors, as shown in figure 49. The numbers of salvaged *BzN3*s and *uzN3*s (*uRN3*s and *BRN3*s) were greater than those of *BzK*s (*uRJ*s), even in this dataset, as shown in figure 47. Hereafter, we often treat *BzN3*s and *uzN3*s (*uRN3*s and *BRN3*s) as an extended BBG class of *BzK*s (*uRJ*s) at $z \simeq 2$ ($z \simeq 1$) and call these BBGs selected by including the AKARI NIR photometry as extended BBGs while the BBGs selected only with the ground-based photometry as classical BBGs.

Appendix 2. Summary of Classifications

Hereafter, we summarize the photometric classification schemes introduced in the paper, and show their outline as following tree diagrams, in which asterisk ∗, circle ∘, and star ⋆ at the front of a category represent classifications without using redshift information, using redshift information, and with substituting photometric color conditions for redshift selections, respectively.

A.2.1. Optical Classifications

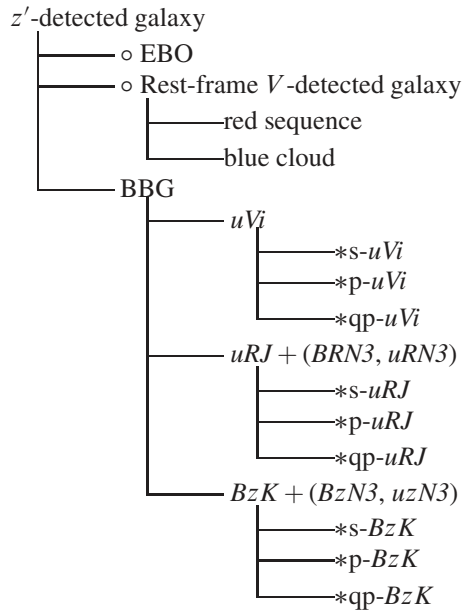

- z'-detected galaxies: As shown in subsection 3.1, we selected ∼56000 of them, performed their photometry, as summarized in table 2, and estimated $z_{\rm phot}$, M_*, A_V, and $SFR_{\rm opt;cor}$, as described in section 4 and appendix 3.
- EBOs: Extremely Blue Objects were selected with the criteria of equation (2), which are possibly AGNs, as discussed in subsection 4.2 and appendix 5.1.
- Rest-frame V-detected galaxies: We studied their stellar populations, which are subclassified as red sequence and blue cloud in the CMD with criteria (5), as discussed in subsection 4.2.
- BBGs: Balmer Break Galaxies (BBGs), including the extended ones (e-BBGs), were introduced for redshift subclassifications of *uVi*s, e-*uRJ*s, and e-*BzK*s including *BzN3*s and *uzN3*s. They are also subclassified into star-forming (s-BBGs), passive (p-BBGs), and quasi-passive (qp-BBGs) populations with the criterias (A2), (A3), and (A4) in appendix 1.

A.2.2. NIR Classifications

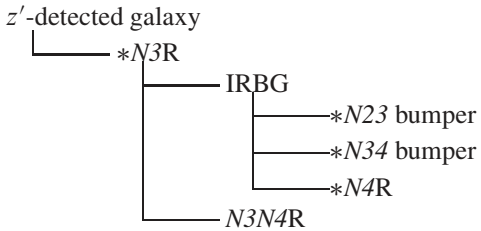

- *N3*Rs: *N3* Red galaxies are selected from the z'-detected galaxies by the criterion (6) in subsection 5.1, which roughly correspond to populations at $z > 0.4$.
- IRBGs: *N3*Rs were subclassified to the *N23*, *N34* bumpers, and *N4* Red galaxies (*N4*Rs) by the criterion (7) as InfraRed Bump Galaxies with 1.6 μm IR bump features from their stellar emissions.
- *N23*, *N34* bumpers, and *N4*Rs: They approximately correspond to the *uVi*s, e-*uRJ*s, and e-*BzK*s, respectively.
- *N3N4*Rs: *N3N4* Red galaxies were classified by equation (12), which are possibly bright AGN candidates, as discussed in subsection 6.2.

A.2.3. MIR Classifications

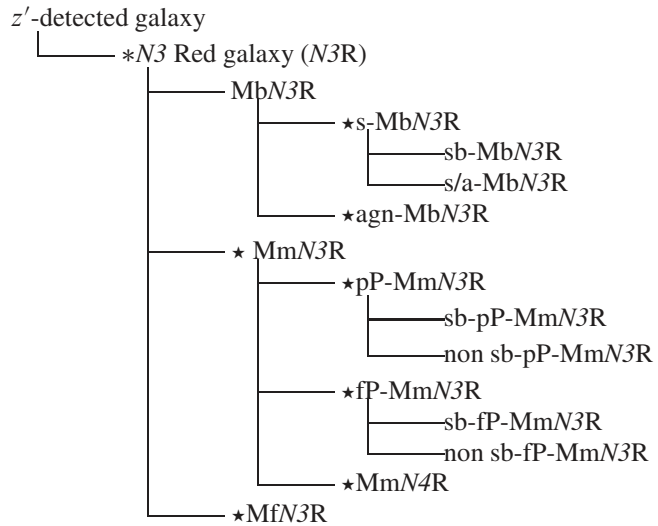

- Mb*N3*Rs: MIR bright *N3*Rs were selected from the *N3*Rs with detection in more than two MIR bands, as described in subsection 6.1.
- s- and agn-Mb*N3*Rs: Mb*N3*Rs were subclassified to starbursts (s-Mb*N3*Rs) and AGNs (agn-Mb*N3*Rs) by the MIR color criteria (8), (9), and (10) at $z = 0.4$–0.8, 0.8–1.2, and > 1.2, respectively, as shown in figure 6.
- sb- and s/a-Mb*N3*Rs: s-Mb*N3*Rs were subclassified to starburst-dominant (sb-Mb*N3*Rs) and starburst/AGN mixture (s/a-Mb*N3*Rs) by their IR SED fittings.
- Mm*N3*Rs: MIR marginally-detected *N3*Rs were detected only in one or two MIR bands with $S/N > 3$, which may be mimics of Mb*N3*Rs with fainter MIR emission. They were subclassified the pP-, fP-, sb-, and non sb-Mm*N3*Rs as discussed in subsection 6.3.
- pP- and fP-Mm*N3*Rs: Mm*N3*Rs were subclassified to the possibly PAH emitting (pP-Mm*N3*Rs) and the faint PAH (fP-Mm*N3*Rs) populations as the PAH 7.7 μm emission from the former is possibly dominant in the *S11*, *L15*, and *L18* bands at $z = 0.4$–0.65, 0.65–1.5, and > 1.5 while that from the latter is not.
- sb- and non sb-Mm*N3*Rs: starburst-dominant populations (sb-Mm*N3*Rs) have MIR SEDs that are reproduced by the S&K model with a low AGN mixture rate of $< 50\%$, while non sb-Mm*N3*Rs do not.

- Mf*N3*Rs: MIR faint *N3*Rs were not detected in any MIR bands with $S/N > 3$, as discussed in subsection 6.4.

A.2.4. Combining Classifications

We sometimes introduced subgroups by combining these optical, NIR, and MIR classifications. For example, *N3*Rs, classified by the criteria of the IR bump in the NIR photometry, can be also subclassified into s-, p-, and qp-BBGs with the criteria of the Balmer break in the optical photometry, which were applied for *N3* Red BBGs as exclusively classified BBGs from *N3*Rs, as can be seen in subsection 5.2. Thus, the combination of classifications at different wavelengths can help us when quickly studying galaxies.

Appendix 3. Photometric Redshifts of Various Populations

We obtained the spectra of 83 *N3*Rs, in which MIR bright sources are subclassified into 35 sb-Mb*N3*Rs, 9 s/a-Mb*N3*Rs, and 14 agn-Mb*N3*Rs. For these spectroscopic *N3*Rs and Mb*N3*Rs samples, figures 51 and 52 show the redshift discrepancy $\Delta z = z_{\rm phot} - z_{\rm spec}$. The median accuracies of $\langle\Delta z\rangle/(1 + z_{\rm spec})$ are 0.040, 0.041, 0.039, 0.042, 0.034, and 0.21 for all the *N3*Rs, relatively bright *N3*Rs ($N3 < 19.9$), relatively faint *N3*Rs ($N3 > 19.9$), sb-Mb*N3*Rs, s/a-Mb*N3*Rs, and agn-Mb*N3*Rs, respectively.

We can see no essential difference in the median accuracy between the relatively bright and faint *N3*Rs, which means that the brightness does not essentially affect the photometric redshift estimations. We can also see that sb-Mb*N3*Rs, preselected for $z > 0.4$ with the IR bump criterion $N2 - N3 > -0.3$, show good agreement between $z_{\rm spec}$ and $z_{\rm phot}$, which means that the photometric redshift estimation is still robust even under heavy extinctions in these Mb*N3*Rs as long as one excludes low redshift dusty starbursts with the IR bump detection.

The agn-Mb*N3*Rs show the largest discrepancy in all subclasses in *N3*Rs. This confirms that AGN is one major cause for inducing deviations in the photometric redshifts, which is reasonable, since we used only stellar population synthesis modeled SEDs as BC03 without including AGN SEDs. Even though 14 spectroscopically observed agn-Mb*N3*Rs, as candidates harboring AGNs, include 8 outliers, all the outliers are spectroscopically identified as BL AGNs, and the remaining 6 non-outliers out of BL AGNs show that their median accuracy is comparable to that of the sb-Mb*N3*Rs as $\langle\Delta z\rangle/(1 + z_{\rm spec}) = 0.042$. This suggests that their photometric redshifts can be accurately estimated from the SED fitting with their major stellar emission of the host galaxies even harboring AGNs.

Thus, the photometric redshifts for *N3*Rs and Mb*N3*Rs can be used to reconstruct their redshifts.

Appendix 4. Redshift Distributions of Galaxies

Figures 53, 54, and 55 show the photometric redshift $z_{\rm phot}$ vs. rest-frame H absolute magnitudes and monochromatic luminosities $\nu L_{\nu,7.7}$. Following the conversion from rest-frame H absolute magnitude to M_* with equation (A11) in appendix 7, we can see that galaxies with $> 10^{10}\,M_\odot$ are detected as the *N3*Rs at $z > 1$ in figure 53. The standard nomenclature LIRG refers to a luminosity class of

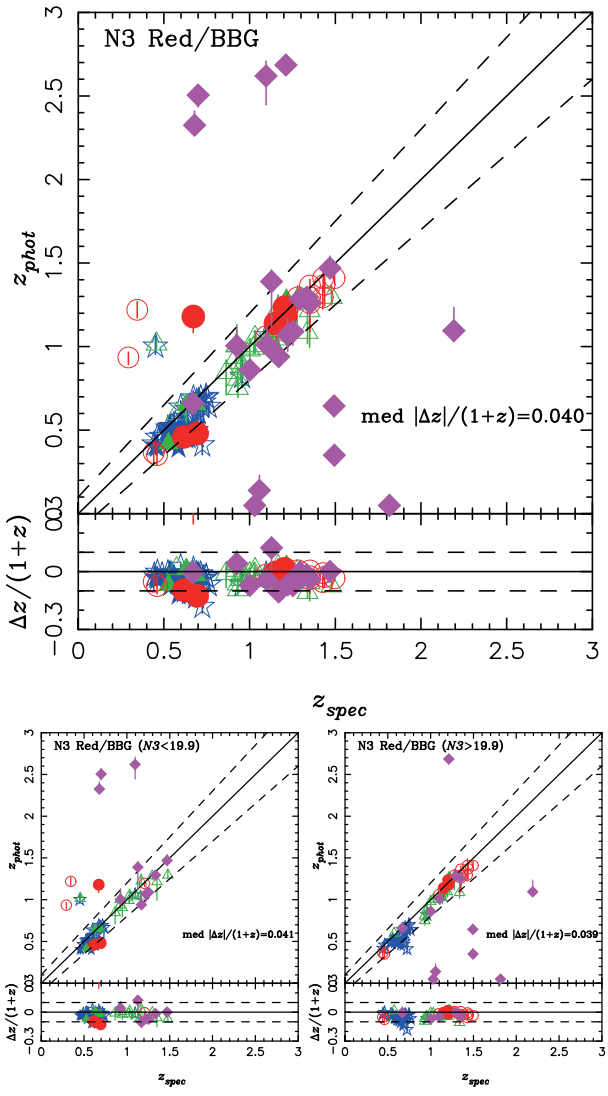

Fig. 51. Same as figure 1 for the *N3* Red BBGs. The colors and symbols are the same as figure 6. The magenta diamonds mean BL AGNs classified with the spectroscopy. Top: For all spectroscopic *N3*Rs. Bottom-left: For relatively bright *N3*Rs with $N3 < 19.9$. Bottom-right: For relatively not-bright *N3*Rs with $N3 \geq 19.9$.

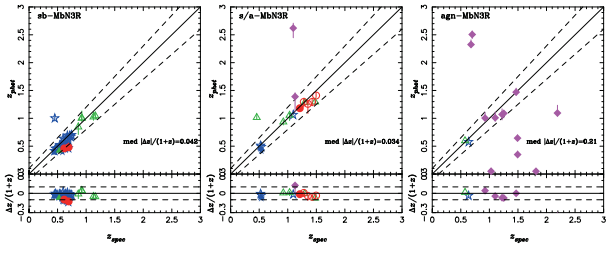

Fig. 52. Same as figure 51 for Mb*N3*Rs; the sb-, s/a-, and agn-Mb*N3*Rs from left to right, which are subclassified on the basis of their MIR SED features, as shown in subsection 6.1.

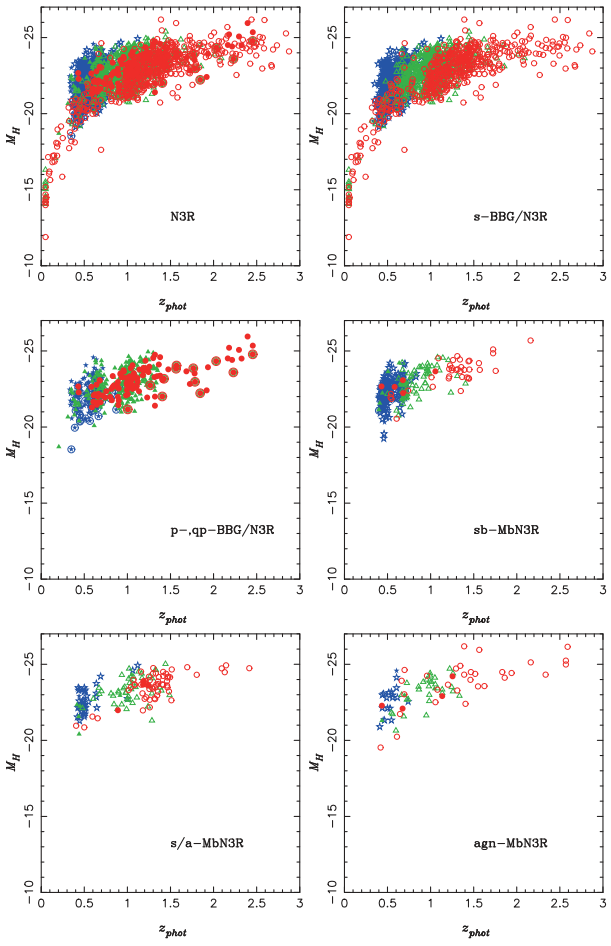

Fig. 53. Photometric redshift $z_{\rm phot}$ vs. rest-frame H absolute magnitudes for *N3*Rs. The colors and symbols are the same as in figure 6. Upper-left: For all the *N3*Rs. Upper-right: Same as the upper-left, for the IRBGs classified as s-BBGs. Middle-left: Same as the upper-left, for the IRBGs classified as p-BBGs. Middle-right: Same as the top-left, for the AKARI MIR detected IRBGs classified as sb-Mb*N3*Rs. Bottom-left: Same as the top-left, for the MIR detected IRBGs classified as s/a-Mb*N3*Rs. Lower-right: Same as the upper-left, for the MIR detected IRBGs classified as agn-Mb*N3*Rs.

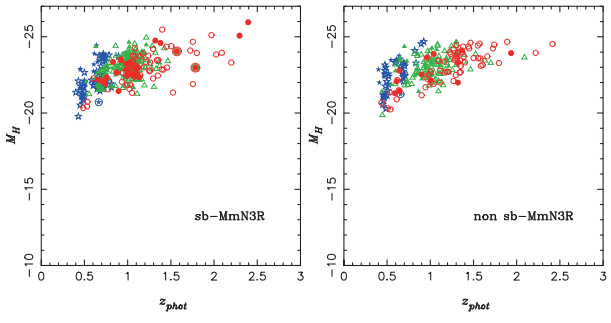

Fig. 54. Photometric redshift $z_{\rm phot}$ vs. rest-frame H absolute magnitudes for the Mm*N3*Rs. The colors and symbols are the same as in figure 6. Left: For the sb-Mm*N3*Rs. Right: For the non ab-Mm*N3*Rs.

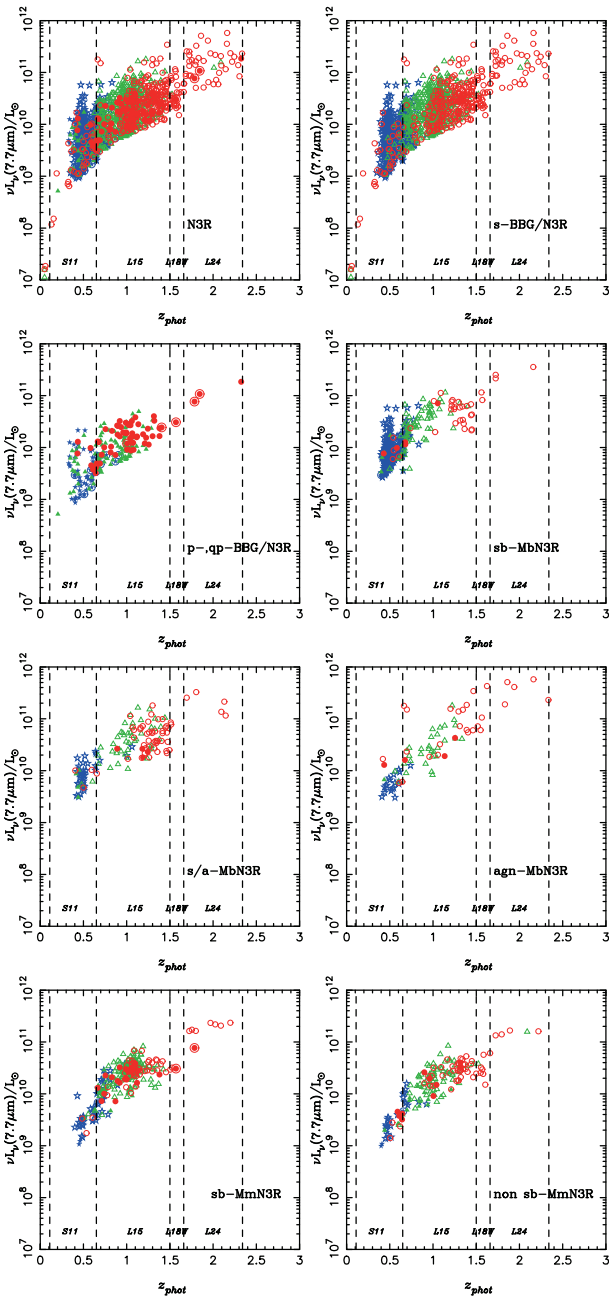

Fig. 55. Photometric redshifts $z_{\rm phot}$ vs. monochromatic luminosities $\nu L_{\nu,7.7}$ at the rest frame 7.7 μm. The colors and symbols are the same as in figure 6.

galaxies with $L \simeq 10^{11-12}\,L_\odot$ and is distinct from starbursts $L \simeq 10^{10-11}\,L_\odot$ and ULIRG $> 10^{12}\,L_\odot$. Following the conversion from $\nu L_{\nu,7.7}$ to TIR luminosity with equation (16) in subsection 7.2, we can see that most of the AKARI MIR-detected galaxies, classified as the s- and s/a-Mb*N3*Rs and sb-Mm*N3*Rs, have typically a TIR luminosity of $10^{11-12}\,L_\odot$, which corresponds to those of local LIRGs.

We can also see that the trend of agn-Mb*N3*Rs is different from those of sb- and s/a-Mb*N3*Rs.

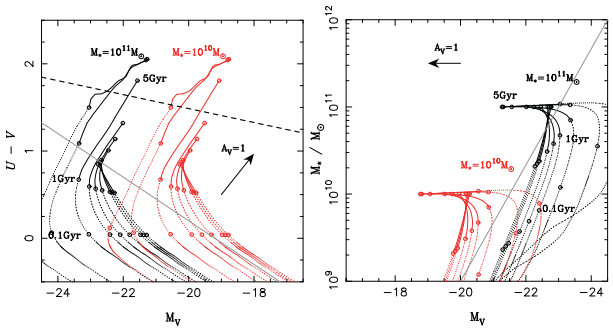

Fig. 56. Left: Evolutionary tracks on the color–magnitude diagram (CMD) of M_V vs. $(U - V)$ from the BC03 model. Red and black lines correspond to systems with $M_* = 10^{10}\,M_\odot$ and $M_* = 10^{11}\,M_\odot$ at 5 Gyr, repsectively, which are evolving with exponential decaying star formation with time scales of $\tau = 0.1$, 0.3, 1,2, 3,5, 15, 30 Gyr and Constant Star Formation (CSF) from the left to the right on the diagram. All of them are in the cases without extinctions. The open circles represent the ages of the systems of 0.1, 1, and 5 Gyr for all models. An arrow at $(M_V, U - V) = (-18, 1)$ represents a color–magnitude correction with a mean extinction of $A_V \simeq 1$. Right: Same as on the left for the mass–magnitude diagram of M_V vs. M_* from the BC03 model.

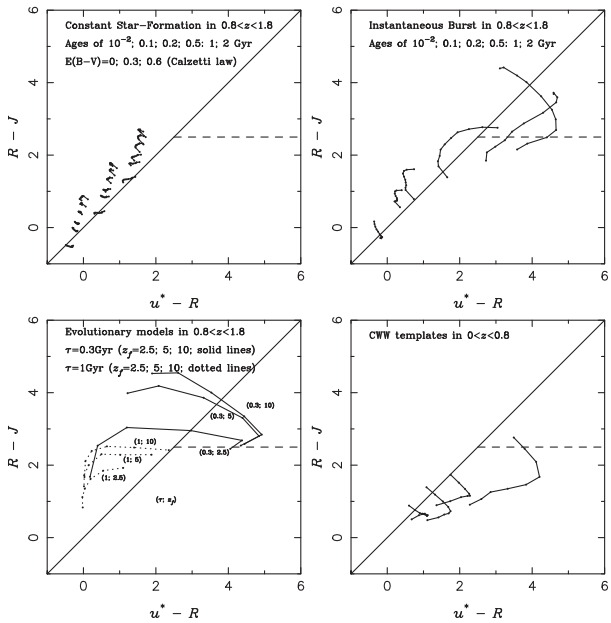

Fig. 57. Evolutionary tracks in the *uRJ* diagram from theoretical models that are the same as figure 8 for the *BzK* diagram in Daddi et al. (2004). The top-left panel shows continuous star-formation model tracks for ages from 1 Myr to 2 Gyr and for $E(B - V) = 0$, 0.3, 0.6. The top-right panel has simple stellar population models for ages from 0.1 to 2 Gyr and no reddening. The bottom-left panel shows evolutionary models with various formation redshifts and *SFR* timescales and no reddening. At decreasing redshifts the tracks generally turn from bottom-left to top-right. The bottom-right panel shows colors for the local templates of various galaxy types from Coleman, Wu, and Weedman (1980). All models are plotted for the range $0.8 < z < 1.8$, except in the bottom-right panel where plots are for $0 < z < 0.8$. The limits and color ranges of all four panels reproduce those of figure 45, for a direct reference.

Appendix 5. Models for SEDs and Colors

A.5.1. Model Tracks for Extremely Blue Objects

As remarked in subsection 4.1, all spectroscopic BL AGNs in the $z_{\rm phot}$ outliers are also EBOs with $(U - V) < -0.25(M_V + 22.0) + 0.7$, which suggests that most of the EBOs are possibly AGN candidates, as long as the redshift estimation is unaffected even by SEDs with a mixture of stellar and AGN emissions. In order to confirm this assumption, we reconstructed the evolutionary tracks with the BC03 model on the CMD and the magnitude vs. stellar mass diagram, as shown in figure 56. Most of the observed star-forming galaxies suffer from extinctions $A_V \simeq 1$ as discussed in subsection 7.3. Thus, most normal star-forming galaxies with $A_V \simeq 1$, except young phase ones with age < 0.1 Gyr, cannot appear in the EBO region of $(U - V) < -0.25(M_V + 22.0) + 0.7$ on the CMD. Even without any extinctions, only objects in an early star-forming epoch < 1 Gyr can have the color of EBOs. It is not realistic to ignore extinctions. Indeed, we found evidence for existing dust even in the EBOs with MIR emission, as reported in subsection 4.1.

A.5.2. Model Tracks for Balmer Break Galaxies

In order to determine the criteria for selecting the BBGs, as shown in appendix 1.1, we studied the model tracks on two-color diagrams of *uRJ*, *uVi*, *BzN3*, *uzN3*, *BRN3*, and *uRN3* as shown in figures 57, 58, 59, 60, 61, and 62, respectively.

The top-left panels of all figures represent the tracks of Constant Star Formation (CSF) for ages of 10^{-2}, 0.1, 0.2, 0.5, 1, and 2 Gyr, various reddening with Calzetti's extinction law, and solar metallicity. We can see that galaxies in such a redshift range with ongoing star formation are indeed expected to lie in the left-upper side region $\mathcal{B}\mu\mathcal{R} \geq f_{\mathcal{B}\mu\mathcal{R}}$ of the two-color diagrams. The duration of the star formation (age) has little influence on the bluer color $\mathcal{B} - \mu$, while the redder color $\mu - \mathcal{R}$ increases with age due to the development of strong Balmer/4000 Å breaks falling in the μ-band around these selecting redshift $z \simeq \langle z \rangle_{\mathcal{B}\mu\mathcal{R}}$. Very young bursts with ages less than 10 Myr without underlying older stellar populations would be located around the left-bottom region just below the line of $\mathcal{B}\mu\mathcal{R} = f_{\mathcal{B}\mu\mathcal{R}}$.

We note that the reddening direction is approximately parallel to the critical line of criteria $\mathcal{B}\mu\mathcal{R} = f_{\mathcal{B}\mu\mathcal{R}}$, since dust extinction is approximately represented as a power-law function of the wavelength and it is implying that the reddening is similar in the $\mathcal{B} - \mu$ and $\mu - \mathcal{R}$ colors for star-forming galaxies in the selected redshift range. It means that the generalized criteria $\mathcal{B}\mu\mathcal{R} \geq f_{\mathcal{B}\mu\mathcal{R}}$ for selecting BBGs are also robust from their dust reddening.

The top-right panels of all figures represent the tracks of simple stellar population (SSP) models after an instantaneous burst, in two-color diagrams, for ages of 10^{-2}, 0.1, 0.2, 0.5, 1, and 2 Gyr, with no reddening, and solar metallicity. Their features are also similar to those in the *BzK*s, since the tracks are similar to those of star-formings at young ages, and begin to move to the region of p-BBGs at older ages of ≥ 1 Gyr. Even though some tracks for intermediate ages of ~ 0.5–1 Gyr are outside of the s/p-BBG regions, the extinction tends to make them redder as those found in the s/p-BBG region. Even

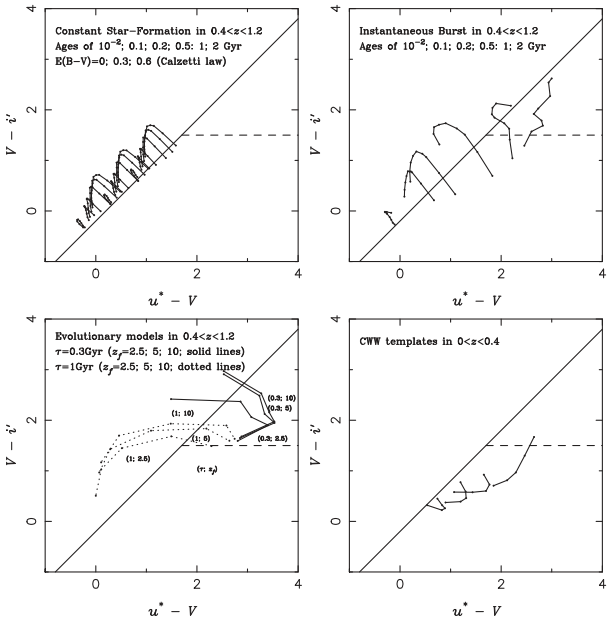

Fig. 58. *uVi* diagram, same as figure 57, except for the redshift range. All models are plotted for the range $0.4 < z < 1.2$, except in the bottom-right panel, where plots are for $0 < z < 0.4$. The limits and color ranges of all four panels reproduce those of figure 46, for a direct reference.

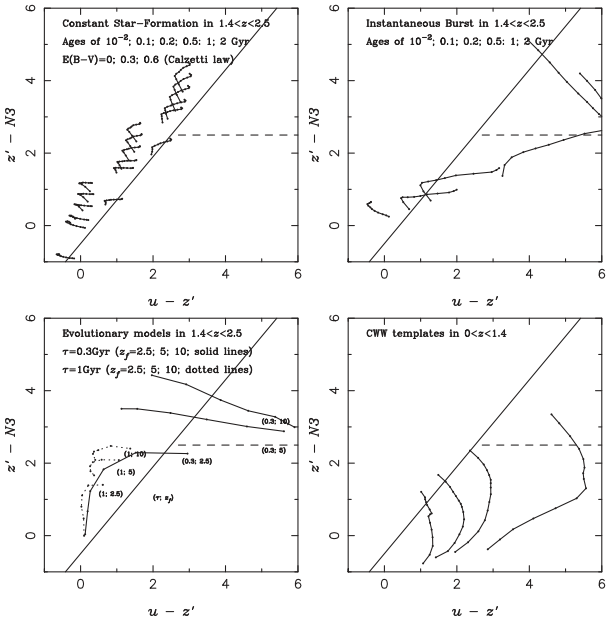

Fig. 60. *uzN3* diagram, same as figure 59, except for the redshift range. All models are plotted for the range $1.4 < z < 2.5$, except in the bottom-right panel, where plots are for $0 < z < 1.4$. The limits and color ranges of all four panels reproduce those of figure 49, for a direct reference.

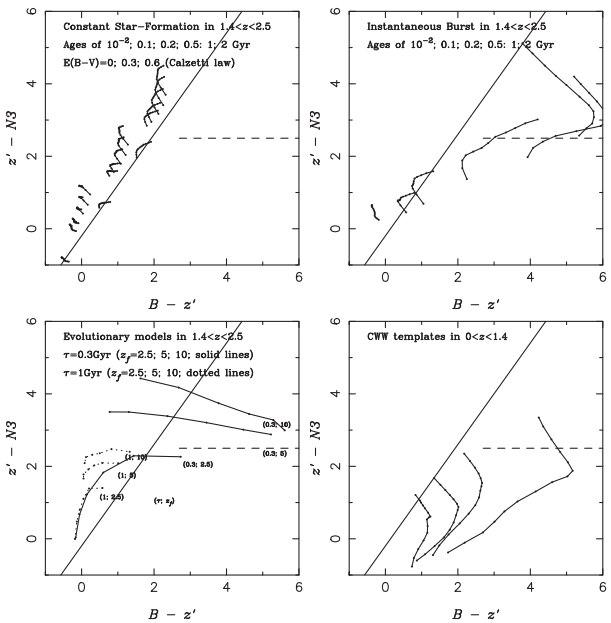

Fig. 59. *BzN3* diagram, same as figure 57, except for the redshift range. All models are plotted for the range $1.4 < z < 2.5$, except in the bottom-right panel where plots are for $0 < z < 1.4$. The limits and color ranges of all four panels reproduce those of figure 49, for a direct reference.

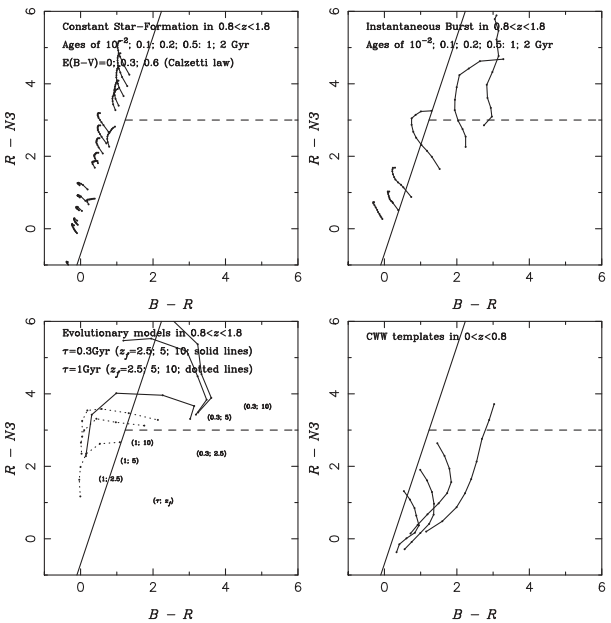

Fig. 61. *BRN3* diagram, same as figure 57, except for the redshift range. All models are plotted for the range $0.8 < z < 1.8$, except in the bottom-right panel where plots are for $0 < z < 0.8$. The limits and color ranges of all four panels reproduce those of figure 49, for a direct reference.

though we should be cautious when applying the SSP model with no reddening to the analysis for real galaxies, the results support that the generalized schemes for selecting s/p-BBGs might still be robust.

The left-bottom panels of all figures show that the $\mathcal{B}\mu\mathcal{R}$ colors for galaxies with various formation redshifts are exponentially declining *SFR*s ($\tau = 0.3$ and 1 Gyr), with no reddening and solar metallicity. The color evolution of galaxies formed at high redshifts is such that most objects move directly from the star-forming galaxy region to the passive galaxy

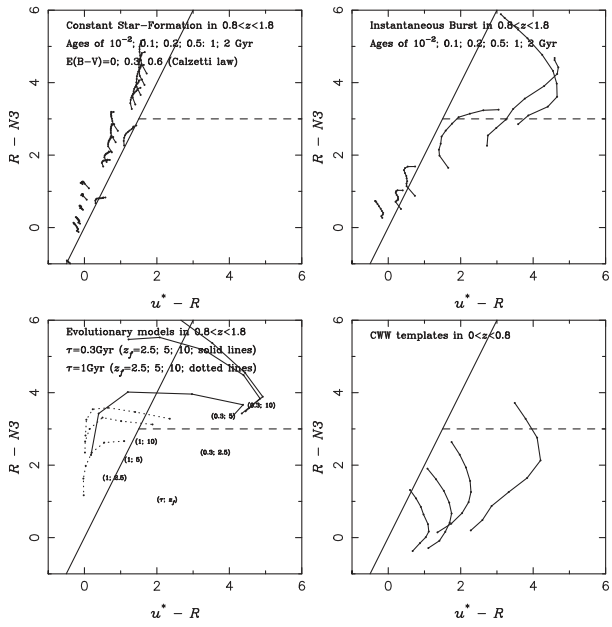

Fig. 62. *uRN3* diagram, same as figure 59, except for the redshift range. All models are plotted for the range $0.8 < z < 1.8$, except in the bottom-right panel where plots are for $0 < z < 0.8$. The limits and color ranges of all four panels reproduce those of figure 49, for a direct reference.

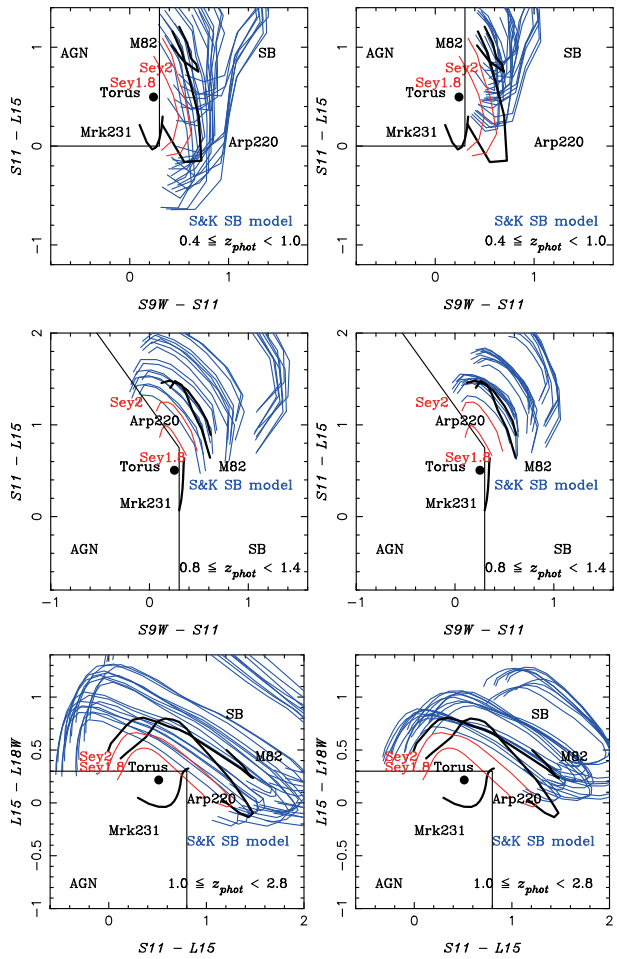

Fig. 63. MIR color–color diagrams for the model SEDs of LIRGs. Thin blue and solid black lines represent tracks for dusty starburst models, and observed (U)LIRGs: M 82, Arp 220, and Mrk 231. Black filled circle represents the dusty torus model of QSO2 in SWIRE SED templates. Objects in the left regions bounded with a thin solid line are excluded from starburst sample. Left: For the S&K model SEDs with a hot spot parameter of $n^{\rm hs} = 10^2\,{\rm cm}^{-3}$. Right: Same as on the left for $n^{\rm hs} = 10^4\,{\rm cm}^{-3}$. Top: *S9W* − *S11* vs. *S11* − *L15* diagram with the model tracks in the interval $0.4 < z < 1.0$. Middle: Same as the top-left, with the tracks in $0.8 < z < 1.4$. Bottom: *S11* − *L15* vs. *L15* − *L18W* diagram with the tracks in $1.0 < z < 2.8$.

region without crossing the bluer regions populated by $z < 1.4$ objects.

The right-bottom panels of all figures show that the colors of normal galaxies are derived from the CWW templates of E-Sbc-Scd-Irregular galaxies (Coleman et al. 1980), which fall outside the color area of the BBGs for $z > 0.8$ ($z > 0.4$), respectively. This means that the generalized two-color criteria can work to exclude the lower-z interlopers.

A.5.3. Model Tracks for Dusty Starbursts and AGNs

In figure 63, the thin blue curves, thick solid black curves, and black filled circles represent the redshifted tracks of dusty starburst SEDs of the S&K model, SEDs of Arp 220, M 82, and Mrk 231, and a model torus SED used to fit the SED of a heavily obscured type 2 QSO SWIRE J104409.95+585224.8 (Polletta et al. 2006), respectively. As shown in figure 63, all of the dusty starbursts of the S&K model, Arp 220, and M 82 appear in the right area while the AGNs, including Mrk 231 as an obscured AGN, appear in the left area. Thus, dusty starburst dominant LIRGs can be distinguished from AGN dominant LIRGs on the MIR color diagrams with a boundary represented as solid lines, which are introduced with equation (8) at $z = 0.4$–1.0, equation (9) at $z = 0.8$–1.4, and equation (10) at $1.0 < z < 2.8$ in section 6.

A.5.4. IR SED Models

By integrating a fitted model SED in rest-frame 8–1000 μm wavelength and correcting for the photometric redshift $z_{\rm phot}$, we can obtain the TIR luminosity, $L_{\rm IR}$, of the emission from the dusty star-forming regions. There are various IR SED models. IR SED libraries can be prepared with three different kinds of schemes: (1) using SED templates of known galaxies (Laurent et al. 2000; Lutz et al. 2003; Spoon et al. 2004), (2) reproducing the SED with optical thin emission from the dusts assumed to be heated in a given radiation field without radiative transfer calculations (Chary & Elbaz 2001; Dale & Helou 2002; Lagache et al. 2003), and (3) calculating radiative transfer to evaluate the emission reprocessed with dusty medium in a spheroidal shape (Silva et al. 1998; Efstathiou et al. 2000; Takagi et al. 2003; Dopita et al. 2006; Piovan et al. 2006a, 2006b; Siebenmorgen & Krügel 2007), or a general three dimensional shape (Kylafis & Bahcall 1987; Popescu et al. 2000), using ray tracing or Monte Carlo techniques (Bianchi et al. 2000). Even in scheme (3), the interaction between dust and radiation is treated consistently in Takagi et al. (2003) and Siebenmorgen and Krügel (2007). Even though empirical conversions from a monochromatic IR luminosity have been sometimes used, their empirical laws have

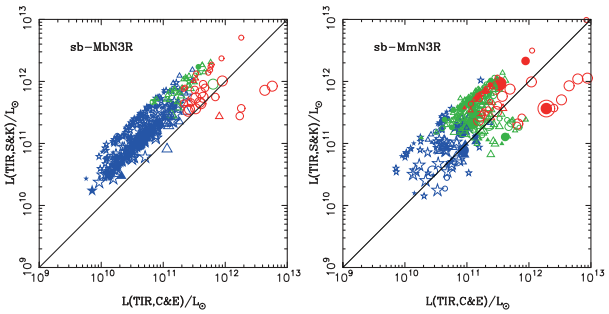

Fig. 64. Comparison between TIR luminosities, $L_{\rm IR}$, estimated from the C&E model and the S&K model for the sb-Mb*N3*Rs and the sb-Mm*N3*Rs. The symbols are the same as in figure 6, except for their colors. Blue, green, and red symbols represent the redshifts of $0.4 \leq z < 0.8$, $0.8 \leq z < 1.2$, and $z \geq 1.2$, respectively. Large, medium, and small symbols indicate the results which fit well with the S&K model SEDs of $A_{V;\rm SK} = 2.2$, 6.7, and 17.9, respectively. Left: For the sb-Mb*N3*Rs. Right: For the sb-Mm*N3*Rs.

been frequently derived from the SED fitting (Bavouzet et al. 2008). When we choose to use them, we should take into account their conceptional differences and applicable situations along with their limitations.

In order to extract information related to the physical properties in a dusty star-forming nucleus, such as the optical depth and dust density from the MIR SEDs with PAH emissions and Si absorption, in this paper, we have taken the S&K model. This can be used to prepare MIR SEDs not only with various PAH emission strengths but also Si absorption depth mainly parametrized with radiation field strength and optical depth, respectively. Individual SED features in the S&K model depend on the following parameters; total luminosity $L^{\rm tot}\,L_\odot$, size of starbursting nucleus R kpc, visual extinction $A_{V;\rm SK}$, ratio of OB star luminosity with hot spots to the total luminosity $L_{\rm OB}/L^{\rm tot}$, and hydrogen number density in the hot spots $n^{\rm hs}$. Even though the S&K model depends on the luminosity $L^{\rm tot}$, we have scaled luminosities and used only their features in the MIR SED fittings. The parameters $L^{\rm tot}$, R, and $A_{V;\rm SK}$ have some degeneracy for variations of the MIR SED features. As shown in the comparison between figures 63, 6, 11, and 12, the models with a hot spot parameter, $n^{\rm hs} = 10^2\,{\rm cm}^{-3}$, can cover typical MIR colors of Mb*N3*Rs and Mm*N3*Rs while the model with $n^{\rm hs} = 10^4\,{\rm cm}^{-3}$ cannot. Thus, we have fixed the hot spot parameter with $n^{\rm hs} = 10^2\,{\rm cm}^{-3}$. And, we have used its 27 models fixed with $R = 3$ kpc and parametrized with $L^{\rm tot} = 10^{10.1}$, $10^{11.1}$, and $10^{12.1}\,L_\odot$, $A_{V;\rm SK} = 2.2$, 6.7, and 17.9, and $L_{\rm OB}/L^{\rm tot} = 0.40$, 0.60, and 0.90, which are treated as only qualitative parameters to reproduce varieties in the MIR SEDs, not as quantitative parameters describing an exact physical state in the starburst nucleus.

In fact, the conversion from $\nu L_{\nu,7.7}$ to $L_{\rm IR}$ depends on the IR SED models used in the fitting. For an example, as shown in figure 64, for most of the sb-Mb*N3*Rs and Mm*N3*Rs, we can see that the estimated $L_{\rm IR;SK}$ from the SED fitting with the S&K model is approximately larger by a factor of three than those with the Chary and Elbaz (2001) model (hereafter C&E model). The IR emission at $> 10\,\mu$m in most of the S&K model SEDs dominate more than those in the C&E model, which causes the TIR luminosity $L_{\rm IR;SK}$ estimated from the S&K model to be larger than the $L_{\rm IR;CE}$ from the C&E model. The S&K model tends to derive a larger TIR luminosity ratio of $L_{\rm IR;SK}/\nu L_{\nu,7.7}$ when SEDs are fitted well with a larger $A_{V;\rm SK}$, even for samples with the same $\nu L_{\nu,7.7}$. On the other hand, the C&E model derives almost the same TIR luminosity ratio $L_{\rm IR;CE}/\nu L_{\nu,7.7}$ for them. Thus, the difference among the three model parameters for $A_{V;\rm SK}$ appears as the split multi-sequences in figure 64. Figure 64 shows multi-sequences with different ratios $L_{\rm IR;SK}/L_{\rm IR;CE}$ and $A_{V;\rm SK}$ more clearly than figure 17.

In order to reproduce the dependence of the optical depth to derive TIR luminosity in the paper, we have used the templates in the public library by Siebenmorgen and Krügel (2007) while the analysis with Takagi, Arimoto, and Hanami (2003), for MIR detected objects in the field, are also reported in other papers (Takagi et al. 2007, 2010, 2012).

Appendix 6. Error Estimations

With photometric redshifts, we derived the physical values for the detected galaxies as absolute magnitudes, M, monochromatic luminosities, νL_ν, stellar mass, M_*, and *SFR*. The physical values include errors from not only their photometric fluctuation Δm in the observed band, but also the uncertainty of their photometric redshift. In their error estimations, we assumed that the former and the latter are independent of each other.

The absolute magnitude, M, is defined with the luminosity, L_ν, observed magnitude, m_ν, and flux, F_ν, at the observed frequency, ν, as:

$$M = -2.5\log_{10}\frac{L_\nu}{4\pi d_L(10\,{\rm pc})} - 48.6\,, \tag{A5}$$

$$L_\nu = 4\pi d_L(z)^2\frac{F_\nu}{(1+z)}\,, \tag{A6}$$

$$F_\nu = 10^{-0.4(m_\nu+48.6)}\,, \tag{A7}$$

where d_L is the luminosity distance. Thus, since $M = -2.5\log_{10}F_\nu - 2.5\log_{10}\dfrac{d_L(z)^2}{(1+z)}$ + constant with $f(z) = d_L(z)^2/(1+z)$, we estimate the error of absolute magnitudes M as

$$\Delta M = \sqrt{\Delta m_\nu^2 + \left[1.09\frac{\Delta f(z)}{f(z)}\right]^2}\,, \tag{A8}$$

where we used $d(\log_{10}x) = (\log_e 10)^{-1}dx/x = 0.434dx/x$ and $\Delta m_\nu = 1.09\,\Delta F_\nu/F_\nu$.

For the monochromatic luminosities νL_ν and the stellar mass M_*, with the similar schemes, their errors can be derived as:

$$\Delta(\log_{10}\nu L_\nu) = 0.4\sqrt{\Delta m_\nu^2 + \left[1.09\frac{\Delta f(z)}{f(z)}\right]^2}\,, \tag{A9}$$

$$\Delta(\log_{10}M_*) = 0.4\sqrt{\Delta m_K^2 + \left[1.09\frac{\Delta f(z)}{f(z)}\right]^2}\,, \tag{A10}$$

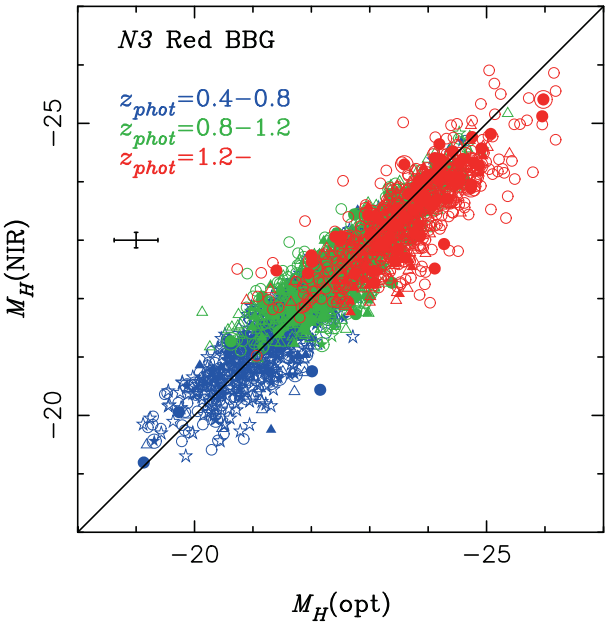

Fig. 65. Comparison of the rest-frame H-band magnitudes for the *N3* Red BBGs between $M_{H;\mathrm{NIR}}$ and $M_{H;\mathrm{opt}}$, which are derived from the AKARI NIR photometry and the ground-based optical–NIR SED fitting, respectively. The symbols are the same as in figure 6, except for their colors. Blue, green, and red symbols represent the redshifts of $0.4 \leq z < 0.8$, $0.8 \leq z < 1.2$, and $z \geq 1.2$, respectively.

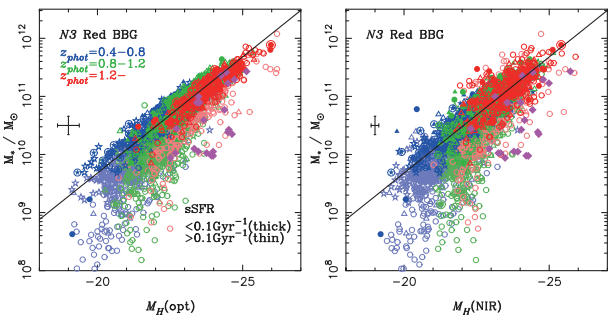

Fig. 66. Absolute rest-frame H-band magnitude M_H vs. stellar mass M_* derived from the optical–NIR SED fitting, for all the *N3* Red BBGs. The symbols are the same as in figure 65. The dark and faint colored symbols represent the subpopulation with $sSFR < 0.1\,\mathrm{Gyr}^{-1}$ and $sSFR > 0.1\,\mathrm{Gyr}^{-1}$. Left: $M_{H;\mathrm{opt}}$ reproduced from the BC03 model fitting vs. M_*. Right: $M_{H;\mathrm{NIR}}$ interpolated from the AKARI NIR photometry vs. M_*.

where we used the error Δm_K in the K band for the stellar mass error estimation.

In error estimations for SFR_{UV} and SFR_{IR}, we used errors, Δm_ν, in the u band and the IRC band related to the rest-frame 7.7 μm, respectively.

Appendix 7. Stellar Mass from Optical/NIR SEDs

The stellar mass, M_*, is estimated in a standard way with the optical–NIR SED fitting for all the z'-detected galaxies and an alternative way from the AKARI/NIR photometry for the IRBGs as a subclass in the z'-detected galaxies.

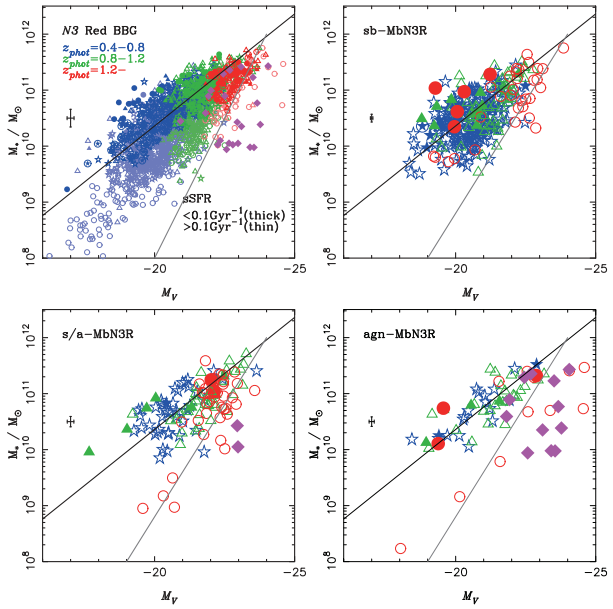

Fig. 67. Absolute rest-frame V-band magnitude M_V vs. stellar mass M_* derived from the optical–NIR SED fitting. Symbols are the same as in figure 6 except their colors. Blue, green, and red mean the redshifts of $0.4 \leq z < 0.8$, $0.8 \leq z < 1.2$, and $z \geqq 1.2$, respectively. Magenta diamonds represent the spectroscopic BL AGNs. The steep line at the right side represents the boundary of the EBOs. Top-left: All of the *N3* Red BBGs with $sSFR < 0.1\,\mathrm{Gyr}^{-1}$ and $> 0.1\,\mathrm{Gyr}^{-1}$ are represented with dark and thin symbols, respectively. Top-right: For the sb-Mb*N3*Rs. Bottom-middle: For the s/a-Mb*N3*Rs. Bottom-right: For the agn-Mb*N3*Rs.

The rest-frame H band wavelength corresponds to the rest-frame 1.6-μm IR bump where the emission is dominated by the stellar components in galaxies. It means that the absolute magnitude in rest-frame H-band M_H represents the underlying stellar mass content M_*. This provided us with two ways to estimate M_H with our dataset; (1) the direct estimation from the AKARI/IRC photometry in the rest-frame H-band at 1.6 μm, and (2) the SED fitting with the ground-based photometric data.

First, *N2*, *N3*, and *N4* photometry can directly detect the 1.6-μm bump from the AKARI/IRC detected IRBGs even at $z > 0.4$. Using the interpolation scheme with equation (4) for *N2*, *N3*, and *N4* photometry with $\lambda_0 = 1.6\,\mu$m and $z = z_{\mathrm{phot}}$, we can estimate the absolute magnitude, $M_{H;\mathrm{NIR}}(z_{\mathrm{phot}})$, corresponding to the rest-frame H-band directly from the *N2*, *N3*, and *N4* magnitudes of the AKARI/IRC detected IRBGs.

Second, the model fitting of Bruzual and Charlot (2003), with the whole ground-based $u^*BVRi'z'JK_{\mathrm{s}}$ SED, derives the absolute magnitude, $M_{H;\mathrm{opt}}$, with our small modified version of the *hyperz* as instantaneously deriving the photometric redshift z_{phot} in subsection 4.1. It can apply for all the z'-detected galaxies. Thus, the derived $M_{H;\mathrm{opt}}(z_{\mathrm{phot}})$ from the optical–NIR SED fitting with the ground-based photometric data is an alternative to determine the stellar mass M_*.

The absolute magnitude, $M_{H;\mathrm{opt}}(z_{\mathrm{phot}})$, from the optical–NIR SED fitting is well correlated with that $M_{H;\mathrm{NIR}}(z_{\mathrm{phot}})$ from the *N2*, *N3*, and *N4* photometry as shown in figure 65. Note this rest-frame $M_{H;\mathrm{NIR}}(z_{\mathrm{phot}})$ from the AKARI/NIR data

can be approximately independent to the $M_{H;\mathrm{opt}}(z_{\mathrm{phot}})$ from the ground-based optical/NIR data, except for the photometric redshift, z_{phot}, derived from the optical dataset. Figure 65 presents not only the consistency between the ground-based NIR and the AKARI/NIR observations, but also accuracy for the photometric redshift from the SED fitting only with the ground-based data.

A weak age dependence between M_* and M_H can be seen in figure 66, in which the deep dark and faint symbols represent old and young populations in the red sequence and blue cloud, respectively, in the $(U - V) - \Delta_{\mathrm{UV}}$ as discussed in subsection 9.1.

Even though the relation between an absolute magnitude, M, in a band and the stellar mass, M_*, depends on the IMF and the star-formation histories, they can be approximately described as

$$\log\left(\frac{M_*}{10^{11}M_\odot}\right) = -0.4(M - M^{11}) , \quad \text{(A11)}$$

where M^{11} is the rest-frame absolute magnitude corresponding to the stellar mass of $10^{11}\,M_\odot$. As shown in figure 66, for M_H in the H band, we can take $M^{11} = M_H^{11} = -23.6$. Even though we mainly used the stellar mass, M_*, derived directly from the optical–NIR SED fittings in the following, the conversion from M_H to M_* is useful as a quick estimation of the stellar mass, M_*.

We also checked the relation between the absolute rest-frame V-band magnitude, M_V, and the stellar mass, M_* (M_V–M_* diagram), derived from the optical–NIR SED fitting, as shown in figure 67. The EBOs and the BL AGNs appear in the right region of the M_V–M_* diagram, where normal star-forming galaxies can appear only at the early phase, < 1 Gyr. Their results in M_V–M_* are consistent with their one concerning the CMD in subsection 4.2, as the EBOs are candidates of AGNs (see also appendix 5). After excluding these EBOs, we obtained a relation between M_V and M_*, approximated as equation (A11) with taking $M_V^{11} = -22$, as shown in figure 67. This conversion from M_V to M_* is useful in making mass–color diagrams in section 9.

References

Alonso-Herrero, A., et al. 2006, ApJ, 640, 167
Arnouts, S., et al. 2007, A&A, 476, 137
Balogh, M. L., Morris, S. L., Yee, H. K. C., Carlberg, R. G., & Ellingson, E. 1999, ApJ, 527, 54
Bavouzet, N., Dole, H., Floc'h, E. L., Caputi, K. I., Lagache, G., & Kochanek, C. S. 2008, A&A, 479, 83
Bell, E. F., et al. 2004, ApJ, 608, 752
Berta, S., et al. 2007, A&A, 476, 151
Berta, S., et al. 2008, A&A, 488, 533
Bertin, E., & Arnouts, S. 1996, A&AS, 117, 393
Bianchi, S., Davies, J. I., & Alton, P. B. 2000, A&A, 359, 65
Blanc, G. A., et al. 2008, ApJ, 681, 1099
Blanton, M. R., et al. 2003, AJ, 125, 2348
Bolzonella, M., Miralles, J., & Pelló, R. 2000, A&A, 363, 476
Borch, A., et al. 2006, A&A, 453, 869
Boulade, O., et al. 2003, Proc. SPIE, 4841, 71
Bouwens, R. J., Illingworth, G. D., Blakeslee, J. P., Broadhurst, T. J., & Franx, M. 2004, ApJ, 611, L1
Brammer, G. B., et al. 2009, ApJ, 706, L173
Brammer, G. B., et al. 2011, ApJ, 739, 24
Brand, K., et al. 2008, ApJ, 673, 119
Brinchmann, J., & Ellis, R. S. 2000, ApJ, 536, L77
Brown, M. J. I., et al. 2008, ApJ, 682, 937
Brown, M. J. I., Dey, A., Jannuzi, B. T., Brand, K., Benson, A. J., Brodwin, M., Croton, D. J., & Eisenhardt, P. R. 2007, ApJ, 654, 858
Bruzual, G., & Charlot, S. 2003, MNRAS, 344, 1000
Bunker, A. J., Stanway, E. R., Ellis, R. S., & McMahon, R. G. 2004, MNRAS, 355, 374
Caputi, K. I., et al 2006, ApJ, 637, 727
Cardelli, J. A., Clayton, G. C., & Mathis, J. S. 1989, ApJ, 345, 245
Chapman, S. C., Smail, I., Blain, A. W., & Ivison, R. J. 2004, ApJ, 614, 671
Chary, R., & Elbaz, D. 2001, ApJ, 556, 562
Choi, P. I., et al. 2006, ApJ, 637, 227
Coleman, G. D., Wu, C.-C., & Weedman, D. W. 1980, ApJS, 43, 393
Cowie, L. L., & Barger, A. J. 2008, ApJ, 686, 72
Cowie, L. L., Hu, E. M., Songaila, A., & Egami, E. 1997, ApJ, 481, L9
Daddi, E., et al. 2007, ApJ, 670, 173
Daddi, E., Cimatti, A., & Renzini, A. 2000, A&A, 362, L45
Daddi, E., Cimatti, A., Renzini, A., Fontana, A., Mignoli, M., Pozzetti, L., Tozzi, P., & Zamorani, G. 2004, ApJ, 617, 746
Dale, D. A., & Helou, G. 2002, ApJ, 576, 159
Damen, M., Schreiber, N. M. F., Franx, M., Labbé, I., Toft, S., van Dokkum, P. G., & Wuyts, S. 2009, ApJ, 705, 617
Dasyra, K. M., et al. 2009, ApJ, 701, 1123
Dennefeld, M., Lagache, G., Mei, S., Ciliegi, P., Dole, H., Mann, R. G., Taylor, E. L., & Vaccari, M. 2005, A&A, 440, 5
Dey, A., et al. 2008, ApJ, 677, 943
Dickinson, M., et al. 2004, ApJ, 600, L99
Dickinson, M., Papovich, C., Ferguson, H. C., & Budavári, T. 2003, ApJ, 587, 25
Donley, J. L., Rieke, G. H., Pérez-González, P. G., Rigby, J. R., & Alonso-Herrero, A. 2007, ApJ, 660, 167
Dopita, M. A., et al. 2006, ApJ, 647, 244
Drory, N., Bender, R., & Hopp, U. 2004, ApJ, 616, L103
Dunne, L., et al. 2009, MNRAS, 394, 3
Efstathiou, A., Rowan-Robinson, M., & Siebenmorgen, R. 2000, MNRAS, 313, 734
Egami, E., et al. 2004, ApJS, 154, 130
Elbaz, D., et al. 2007, A&A, 468, 33
Elbaz, D., et al. 2011, A&A, 533, A119
Elbaz, D., Cesarsky, C. J., Chanial, P., Aussel, H., Franceschini, A., Fadda, D., & Chary, R.-R. 2002, A&A, 384, 848
Elston, R. J., et al. 2006, ApJ, 639, 816
Elston, R., Rieke, G. H., & Rieke, M. J. 1988, ApJ, 331, L77
Faber, S. M., et al. 2007, ApJ, 665, 265
Feulner, G., Gabasch, A., Salvato, M., Drory, N., Hopp, U., & Bender, R. 2005a, ApJ, 633, L9
Feulner, G., Goranova, Y., Drory, N., Hopp, U., & Bender, R. 2005b, MNRAS, 358, L1
Fiore, F., et al. 2008, ApJ, 672, 94
Firth, A. E., et al. 2002, MNRAS, 332, 617
Floc'h, E. L., et al. 2005, ApJ, 632, 169

Fontana, A., et al. 2003, ApJ, 594, L9
Fontana, A., et al. 2004, A&A, 424, 23
Fontana, A., et al. 2006, A&A, 459, 745
Franx, M., et al. 2003, ApJ, 587, L79
Glazebrook, K., et al. 2004, Nature, 430, 181
Gunn, J. E., & Stryker, L. L. 1983, ApJS, 52, 121
Häring, N., & Rix, H.-W. 2004, ApJ, 604, L89
Hatziminaoglou, E., et al. 2005, AJ, 129, 1198
Hernán-Caballero, A., et al. 2009, MNRAS, 395, 1695
Hwang, N., et al. 2007, ApJS, 172, 583
Iglesias-Páramo, J., et al. 2007, ApJ, 670, 279
Imai, K., Matsuhara, H., Oyabu, S., Wada, T., Takagi, T., Fujishiro, N., Hanami, H., & Pearson, C. P. 2007, AJ, 133, 2418
Iwata, I., Ohta, K., Tamura, N., Ando, M., Wada, S., Watanabe, C., Akiyama, M., & Aoki, K. 2003, PASJ, 55, 415
John, T. L. 1988, A&A, 193, 189
Kajisawa, M., Ichikawa, T., Yoshikawa, T., Yamada, T., Onodera, M., Akiyama, M., & Tanaka, I. 2011, PASJ, 63, S403
Kennicutt, R. C. 1998, ARA&A, 36, 189
Ko, J., et al. 2012, ApJ, 745, 181
Kong, X., et al. 2006, ApJ, 638, 72
Kriek, M., et al. 2006, ApJ, 645, 44
Kylafis, N. D., & Bahcall, J. N. 1987, ApJ, 317, 637
Labbé, I., et al. 2005, ApJ, 624, L81
Lacy, M., et al. 2004, ApJS, 154, 166
Lagache, G., Dole, H., & Puget, J.-L. 2003, MNRAS, 338, 555
Lane, K. P., et al. 2007, MNRAS, 379, L25
Laurent, O., Mirabel, I. F., Charmandaris, V., Gallais, P., Madden, S. C., Sauvage, M., Vigroux, L., & Cesarsky, C. 2000, A&A, 359, 887
Lee, H. M., et al. 2007, PASJ, 59, S529
Lehnert, M. D., & Bremer, M. 2003, ApJ, 593, 630
Lejeune, Th., Cuisinier, F., & Buser, R. 1997, A&AS, 125, 229
Lutz, D., Sturm, E., Genzel, R., Spoon, H. W. W., Moorwood, A. F. M., Netzer, H., & Sternberg, A. 2003, A&A, 409, 867
Magdis, G. E., et al. 2010, MNRAS, 409, 22
Magnelli, B., Chary, R. R., Pope, A., Elbaz, D., Morrison, G., & Dickinson, M. 2008, ApJ, 681, 258
Mann, R. G., et al. 2002, MNRAS, 332, 549
Marcillac, D., Elbaz, D., Charlot, S., Liang, Y. C., Hammer, F., Flores, H., Cesarsky, C., & Pasquali, A. 2006a, A&A, 458, 369
Marcillac, D., Elbaz, D., Chary, R. R., Dickinson, M., Galliano, F., & Morrison, G. 2006b, A&A, 451, 57
Miyazaki, S., et al. 2002, PASJ, 54, 833
Murphy, E. J., Chary, R.-R, Alexander, D. M., Dickinson, M., Magnelli, B., Morrison, G., Pope, A., & Teplitz, H. I. 2009, ApJ, 698, 1380
Noeske, K. G., et al. 2007, Apj, 660, L47
Oke, J. B. 1974, ApJS, 27, 21
Onaka, T., et al. 2007, PASJ, 59, 401
Ouchi, M., et al. 2003, ApJ, 582, 60
Ouchi, M., et al. 2004, ApJ, 611, 685
Pannella, M., et al. 2009, ApJ, 698, L116
Papovich, C. 2006, New Astron. Rev., 50, 134
Papovich, C., et al. 2006, ApJ, 640, 92
Papovich, C., et al. 2007, ApJ, 668, 45
Papovich, C., Dickinson, M., & Ferguson, H. C. 2001, ApJ, 559, 620
Peng, Y.-j., et al. 2010, ApJ, 721, 193
Pérez-González, P. G., et al. 2005, ApJ, 630, 82
Pickles, A. J. 1998, PASP, 110, 863
Piovan, L., Tantalo, R., & Chiosi, C. 2006a, MNRAS, 366, 923
Piovan, L., Tantalo, R., & Chiosi, C. 2006b, MNRAS, 370, 1454
Polletta, M., et al. 2006, ApJ, 642, 673
Polletta, M., Weedman, D., Honig, S., Lonsdale, C. J., Smith, H. E., & Houck, J. 2008, ApJ, 675, 960
Popescu, C. C., Misiriotis, A., Kylafis, N. D., Tuffs, R. J., & Fischera, J. 2000, A&A, 362, 138
Pozzetti, L., et al. 2003, A&A, 402, 837
Pozzetti, L., et al. 2007, A&A, 474, 443
Pozzi, F., et al. 2004, ApJ, 609, 122
Quadri, R., et al. 2007, AJ, 134, 1103
Reddy, N. A., Steidel, C. C., Fadda, D., Yan, L., Pettini, M., Shapley, A. E., Erb, D. K., & Adelberger, K. L. 2006, ApJ, 644, 792
Rocca-Volmerange, B., de Lapparent, V., Seymour, N., & Fioc, M. 2007, A&A, 475, 801
Roche, N. D., Almaini, O., Dunlop, J., Ivison, R. J., & Willott, C. J. 2002, MNRAS, 337, 1282
Roche, N. D., Dunlop, J., & Almaini, O. 2003, MNRAS, 346, 803
Salim, S., et al. 2009, ApJ, 700, 161
Santini, P., et al. 2009, A&A, 504, 751
Sawicki, M. 2002, AJ, 124, 3050
Sawicki, M., & Thompson, D. 2006a, ApJ, 642, 653
Sawicki, M., & Thompson, D. 2006b, ApJ, 648, 299
Schlegel, D. J., Finkbeiner, D. P., & Davis, M. 1998, ApJ, 500, 525
Shapley, A. E., Steidel, C. C., Erb, D. K., Reddy, N. A., Adelberger, K. L., Pettini, M., Barmby, P., & Huang, J. 2005, ApJ, 626, 698
Shim, H., Im, M., Choi, P., Yan, L., & Storrie-Lombardi, L. 2007, ApJ, 669, 749
Shimasaku, K., Ouchi, M., Furusawa, H., Yoshida, M., Kashikawa, N., & Okamura, S. 2005, PASJ, 57, 447
Siebenmorgen, R., & Krügel, E. 2007, A&A, 461, 445
Silva, L., Granato, G. L., Bressan, A., & Danese, L. 1998, ApJ, 509, 103
Simpson, C., & Eisenhardt, P. 1999, PASP, 111, 691
Spoon, H. W. W., Moorwood, A. F. M., Lutz, D., Tielens, A. G. G. M., Siebenmorgen, R., & Keane, J. V. 2004, A&A, 414, 873
Stanway, E. R., Bunker, A. J., & McMahon, R. G. 2003, MNRAS, 342, 439
Steidel, C. C., Adelberger, K. L., Giavalisco, M., Dickinson, M., & Pettini, M. 1999, ApJ, 519, 1
Steidel, C. C., Giavalisco, M., Dickinson, M., & Adelberger, K. L. 1996a, AJ, 112, 352
Steidel, C. C., Giavalisco, M., Pettini, M., Dickinson, M., & Adelberger, K. L. 1996b, ApJ, 462, L17
Stern, D., et al. 2005, ApJ, 631, 163
Strazzullo, V., Pannella, M., Owen, F. N., Bender, R., Morrison, G. E., Wang, W.-H., & Shupe, D. L. 2010, ApJ, 714, 1305
Takagi, T., et al. 2007, PASJ, 59, S557
Takagi, T., et al. 2010, A&A, 514, 5
Takagi, T., et al. 2012, A&A, 537, A24
Takagi, T., Arimoto, N., & Hanami, H. 2003, MNRAS, 340, 813
Taylor, E. L., et al. 2005, MNRAS, 361, 1352
Teplitz, H. I., et al. 2007, ApJ, 659, 941
Thompson, D., et al. 1999, ApJ, 523, 100
van Dokkum, P. G., et al. 2004, ApJ, 611, 703
Vergani, D., et al. 2008, A&A, 487, 89
Wada, T., et al. 2008, PASJ, 60, S517
Webb, T. M. A., et al. 2006, ApJ, 636, L17
White, G. J., et al. 2010, A&A, 517, 54
Yan, H., et al. 2004, ApJ, 616, 63
Yan, H., Dickinson, M., Giavalisco, M., Stern, D., Eisenhardt, P. R. M., & Ferguson, H. C. 2006, ApJ, 651, 24
Zheng, X. Z., Dole, H., Bell, E. F., Le Floc'h, E., Rieke, G. H., Rix, H.-W., & Schiminovich, D. 2007, ApJ, 670, 301
Zucca, E., et al. 2006, A&A, 455, 879